Final Report

NASA CR-66812

INVESTIGATION OF COMBUSTION INSTABILITY IN HYBRID ROCKETS

Prepared for:

NATIONAL AERONAUTICS AND SPACE ADMINISTRATION
LANGLEY RESEARCH CENTER
HAMPTON, VIRGINIA

CONTRACT NAS 1-7310

STANFORD RESEARCH INSTITUTE
Menlo Park, California 94025 · U.S.A.

STANFORD RESEARCH INSTITUTE
Menlo Park, California 94025 • U.S.A.

Final Report

INVESTIGATION OF COMBUSTION INSTABILITY IN HYBRID ROCKETS

By: C. E. WOOLDRIDGE, G. A. MARXMAN, and R. J. KIER

Prepared for:

NATIONAL AERONAUTICS AND SPACE ADMINISTRATION
LANGLEY RESEARCH CENTER
HAMPTON, VIRGINIA 23365

ATTN: MR. WILLIAM P. PECK
MAIL STOP 498

CONTRACT NAS 1-7310

SRI Project 6638

Approved:

G. A. MARXMAN, *Director*
Physical Sciences (Physics and Chemistry of Fluids)

MARJORIE W. EVANS
Executive Director
Physical Sciences Division

Copy No. 39

ABSTRACT

This report describes the initial phases of an investigation of hybrid propellant combustion instability. Experimental studies carried out during the first year of this program were principally concerned with the delineation of steady-state hybrid propellant regression rate/pressure coupling in the pressure-sensitive regime, because acoustic instability is expected to depend on the same coupling mechanism. The data established that the onset of the observed dependence of regression rate on pressure at low pressure is attributable to the behavior of the chemical kinetic processes in the gas-phase flame zone. This result provided the basis for theoretical studies performed during the program.

A theoretical model, based on classical turbulent flame theory, was proposed and a mathematical analysis was developed that provided good agreement with the observed steady-state regression rate/pressure dependence at the fixed oxidizer mass flux.

During a few of the experiments, a spontaneous instability corresponding to the longitudinal mode of the chamber was observed to develop. Future studies will be concerned with the delineation of conditions under which the regression rate response to pressure fluctuations can support such instability.

PREFACE

The studies described in this report were performed principally by G. A. Marxman (theory), C. E. Wooldridge (theory and experiments), and R. J. Kier (experiments). The overall program has been under the direction of G. A. Marxman.

Administration and technical direction of the program have been under W. P. Peck, High Temperature Materials Branch, Langley Research Center.

The authors wish to acknowledge the major contributions of A. J. Amaro, R. G. McKee, Jr., and W. H. Johnson to the experimental program. The computer calculations described in this report are the work of Miss Margery Brothers.

CONTENTS

CONTENTS

ILLUSTRATIONS

ILLUSTRATIONS

ILLUSTRATIONS

NOMENCLATURE

A_p Port area for flow

A_t Nozzle throat area

B Thermochemical mass transfer number

B' $2(\rho v)_w/\rho_e u_e c_f$

c_f Friction coefficient = $2\tau_w/\rho_e u_e^2$

C Constant

C_H Stanton number = $Q_w/\rho_e u_e \Delta h$

c_m Heat capacity of nonvaporizing fuel component

c_p Specific heat at constant pressure

c_v Specific heat at constant volume

D Diameter

E_f Gas-phase activation energy

G Total mass flux per unit area

G_o^o Oxidizer mass flux per unit area at x = 0 and t = o

h Enthalpy

h_v Heat of gasification of solid phase

I Radiative intensity per unit volume

k Thermal conductivity of the gas phase

K Mass fraction of nonvaporizing material in the solid phase

K_1 Mass fraction of volatile surface material which forms solid combustion products; chamber parameter

K_2 Chamber parameter

ℓ_1 Characteristic flame propagation length

ℓ_2 Characteristic turbulent mixing length

L Length of grain

Le Lewis number

L_v Heat of vaporization of solid phase

$\dot{m}$ Mass flow rate

M Molecular weight

n Particle number density per unit volume of gas; order of the gas-phase reaction

p Pressure

P Perimeter of grain

Pr Prandtl number

Q_c Chemical heat of reaction

$\dot{Q}_c$ Convective heat transfer in the absence of radiation

$\dot{Q}_r$ Radiative heat transfer

$\dot{Q}_w$ Heat transfer to the wall

$\dot{r}$ Regression rate

r_p Radius of a radiating particle

R Outer radius of radiating annulus; gas constant

R_o Inner radius of radiating annulus

Re_x Reynolds number based on x

t Time

t_1 Characteristic time associated with combustion

T Temperature; characteristic time associated with turbulent mixing

u X-component of velocity

u_f Kinetic flame speed

u' Characteristic turbulent fluctuation

U_f Flame temperature

V Volume

x Longitudinal coordinate in stream direction

x_A Longitudinal coordinate of boundary layer merge point

X Particle displacement by turbulence

y Coordinate normal to solid surface

z Radiative path length

α Empirical radiation coefficient

β Angle defined in Fig. 2

γ Specific heat ratio, c_p/c_v; absorptivity coefficient

δ^* Boundary layer displacement thickness

Δh Sensible enthalpy difference between combustion zone and wall

ϵ Emissivity

ζ Mass of oxidizer consumed in producing particulate products per unit mass of nonvaporizing fuel particles

ζ_1 Mass of oxidizer consumed in producing particulate combustion products per unit mass of volatile surface material which forms particulate products

λ Mass of particles produced per unit mass of particle-producing material in surface

ν Kinematic viscosity

ν_p Stoichiometric coefficient

ν_r Stoichiometric coefficient

ρ Density

ρ_p Particle density

σ Stefan-Boltzmann constant

τ Shear stress; transmissivity

φ Angle defined in Fig. 2

Φ Total radiation per unit time

Subscripts

b Condition at combustion zone

e Conditions at boundary layer edge

f Fuel

g Gas phase

o Conditions with zero surface mass injection; oxidizer

r Radiative

v Conditions of vaporizing component in solid phase

w Conditions at surface

∞ Limiting value at high pressure

I. INTRODUCTION

Increased interest in the development of the hybrid rocket as an important propulsion device has naturally led to a consideration of its behavior over a wide range of operating chamber pressures. Earlier studies of hybrid combustion have concentrated on the high-pressure regime in which the regression rate is controlled by the turbulent diffusion mechanism in the boundary layer formed over the vaporizing surface. For this operating regime a relatively comprehensive theoretical description has been developed.[1-6] For most propellants the theoretical model is in good agreement with experimental observations at pressures above about 200 to 300 psi.[7,8] The theory shows that in diffusion-limited combustion the regression rate is independent of pressure for a given mass flux through the port.[6,8]

For each propellant there is a pressure threshold above which the diffusion-limited theory becomes valid. Below this threshold there is a decrease in the regression rate with a decrease in the pressure at a fixed oxidizer mass flux.[9,10] The next step in the development of hybrid combustion theory must be a description of the low-pressure regime, in which the regression rate is pressure sensitive.

Smoot and Price attempted to correlate their data in a semiempirical fashion, assuming heterogeneous attack to be the rate-controlling factor.[11] An analysis by one of the present authors, however, has shown the heterogeneous reactions alone cannot lead to the observed pressure dependence.[8]

Miller has proposed a model in which the pressure dependence is attributed to the broadening of the gas-phase flame zone caused by reduced reaction rates.[12] Several objections may be raised to this treatment. For example, isothermal conditions are assumed, and convective transfer

is neglected relative to diffusive transport. These assumptions are not applicable to hybrid combustion.

A third treatment, advanced by Kosdon and Williams, is an analysis of small departures from the pressure-independent, diffusion-limited regime.[13] Comparisons of this theory with measurements taken under conditions far from the diffusion-limited regime, for which the theory cannot be valid, show much better agreement than in the small-departure regime, to which the theory should be applicable.[13]

The presence of pressure sensitivity in the regression rate leads to the possibility of an acoustic combustion instability mechanism similar to that encountered in solid propellants. A review of the existing literature shows that little of the research conducted in this country has been directed specifically toward the combustion instability problem in hybrid motors. A study of available instability data suggests, however, the existence of at least three major categories of hybrid combustion instability phenomena:

1. Instability due to the lag time associated with vaporization and combustion of liquid droplets (with liquid injection). This type of instability is related to that in liquid propellant motors but is probably considerably more complex, owing to the influence of the solid-liquid interface processes that affect lag times.

2. Unstable burning associated with periodic accumulation and breakoff of char layers or melted layers at the surface. The resulting instability is generally low in frequency (like "chuffing") and occurs during operation at low regression rates.

3. The combustion instability mechanism mentioned previously, which is related to that encountered in solid propellants. Here the acoustic admittance of the reacting turbulent boundary layer plays a key role, and the instability becomes more severe with a pressure-sensitive regression rate.

The first year's effort on this program has been devoted largely to the third type of instability, which is potentially the most critical. Because

the presence of acoustic instability depends on the presence of a pressure-sensitive regression rate behavior, an understanding of the steady-state combustion mechanism that leads to pressure sensitivity in this regime is a prerequisite to development of a combustion instability theory. For this reason the main objective of the first year's effort has been to define, both experimentally and theoretically, the dependence of regression rate on pressure in the kinetically controlled regime for several representative hybrid propellant combinations. It was found that a relatively simple analytical model based on classical turbulent flame theory exhibits good agreement with the observed regression rate/pressure dependence.

II. BACKGROUND

Before proceeding to a discussion of the work carried out under the current program, it is worthwhile to review the previous status of hybrid combustion fundamentals. The basic premise underlying existing theory is that the combustion process may be described through a boundary layer model. It has been well established[1,2] that in a boundary layer with combustion and a mass addition rate typical of the hybrid application, transition occurs at a length Reynolds number, Re_x of approximately 10^4, or very near the leading edge of the grain. Therefore, a turbulent boundary layer treatment is required for a heat transfer theory of hybrid combustion. All present treatments of turbulent flow are necessarily semiempirical, but the cumulative efforts of a number of investigators such as Lees[14] and Spalding[15] have resulted in a reasonably satisfactory and remarkably simple description of heat and mass transfer in turbulent boundary layers with chemical reactions.

A detailed development of the theory describing hybrid combustion in the pressure-insensitive (or high-pressure) regime is presented in Appendix A. It is shown that in a hybrid motor in which radiative heat transfer is negligible, the regression rate is given by:

$$\rho_f \dot{r} = \frac{\dot{Q}_c}{h_v} = 0.036 G \left(\bar{\rho}/\rho_e\right)^{0.6} B'^{0.23} Re_x^{-0.2} \qquad (1)$$

The radiative heat transfer to the solid grain is given by:

$$Q_r = \sigma \varepsilon_w \varepsilon_g (T_r^4 - T_w^4) \qquad (2)$$

When radiation is present to a significant degree, as in a motor with high metal loading, the regression rate is described by the expression:

$$\rho_f \dot{r} = \frac{\dot{Q}_c}{h_v} \left[e^{-Q_r/Q_c} + \frac{Q_r}{Q_c} \right] \tag{3}$$

where $\dot{Q}_c/h_v$ is given by Eq. 1. It will be noted that when radiation is low, i.e., when $\dot{Q}_r/\dot{Q}_c \ll 1$, Eq. 3 reduces to Eq. 1. Equation 3 also shows the trade-off between convective and radiative transfer which occurs because of the decrease in convective heat transfer with increasing surface mass addition. Procedures required to use these equations, including the method of evaluating the effective heat of gasification, h_v, and the mass transfer number, B, for a given propellant, are discussed in Appendix A.

III. THEORETICAL STUDIES

Theoretical studies in this program were divided into three parts: (1) derivation of an expression for the gas-phase emissivity ε_g which appears in Eq. 2; (2) calculation of asymptotic regression rates at high pressure, using Eq. 3, for the propellant systems chosen for experimental study during this investigation; and (3) formulation of a theoretical description of regression rate behavior in the low-pressure, kinetics-limited domain. Parts 1 and 2 were required to complete part 3, because the theory of the latter expresses the regression rate in terms of the asymptotic limit obtained in part 2. Details of the studies are presented in Appendices B, C, and D.

The main theoretical result of the first year's investigation was a combustion model describing the regression rate behavior in the pressure-sensitive regime. From this model the following equations were derived (Appendix D):

$$\frac{\dot{r}}{\dot{r}_\infty} = \left(\frac{z}{\theta}\right)^{\frac{1}{2}} \left[1 - \frac{1}{\theta}\left(1 - e^{-\theta}\right)\right]^{\frac{1}{2}} \tag{4}$$

where:

$$\theta \equiv C \frac{\ell_1}{\ell_2} \frac{GRe_L^{-0.2} B^{0.23}}{p^{n/2} U_f^{1 + n/2} e^{-E_f/2RU_f}} \tag{5}$$

The constant C is related to flame speed kinetics. The characteristic length ℓ_1 is associated with the scale of the combustion zone, and ℓ_2 is identified with the scale of turbulence. At present the coefficient $C\ell_1/\ell_2$ must be treated as an empirically determined constant for a given propellant system.

Typical results obtained from Eq. 4 are shown in Figs. 1 and 2. These results have been obtained by setting $\theta = 1$ at 10 atm pressure (to evaluate the parameter $C\ell_1/\ell_2$) and using the thermochemical flame temperature versus pressure behavior of a hybrid propellant system consisting of a 60 percent polyurethane/40 percent aluminum fuel with oxygen as the oxidizer. Figure 1 shows the effect of changes in the gas-phase activation energy on the regression rate behavior when the order of the gas-phase reaction is held constant. Figure 2 shows the increased effect of changes in n with E_f held constant. It can be seen that n is a more powerful parameter than E_f in affecting the shape of the regression rate curve. The proper choices for these parameters, as well as for $C\ell_1/\ell_2$ must be found by comparison with experimental data.

When the validity of Eq. 4 has been established by comparison with experimental data, it will be incorporated into the hybrid regression rate computer code for use during the second phase of the program.

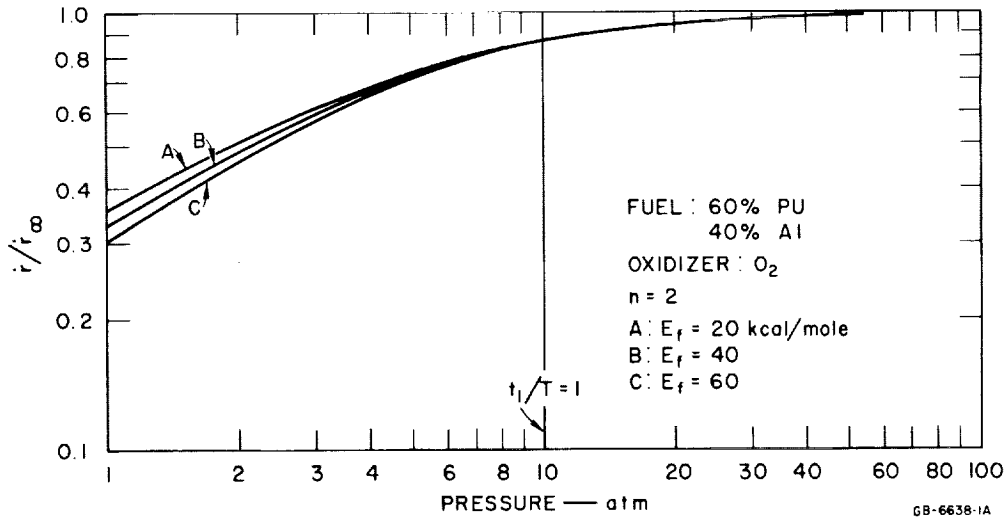

FIG. 1 INFLUENCE OF ACTIVATION ENERGY ON REGRESSION RATE BEHAVIOR

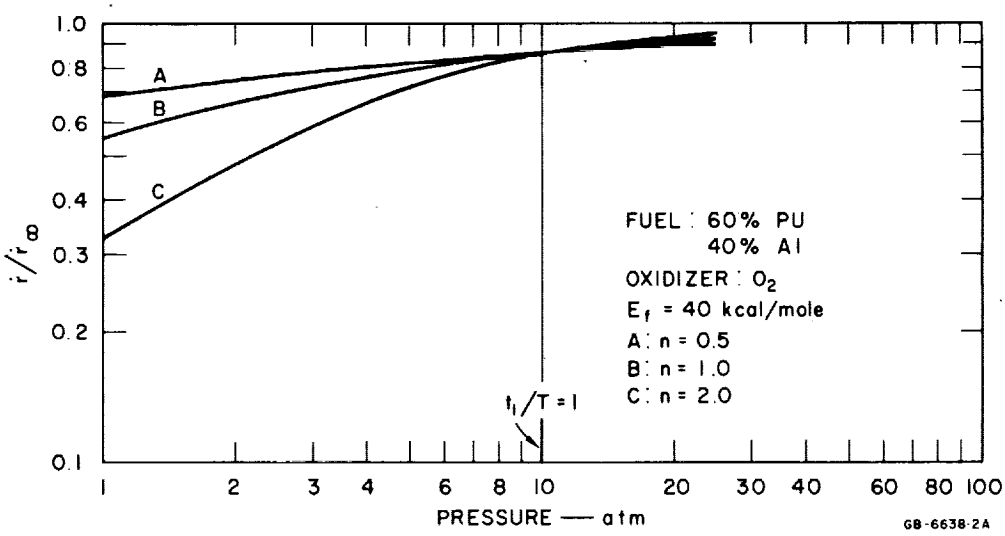

FIG. 2 INFLUENCE OF GAS-PHASE ORDER ON REGRESSION RATE BEHAVIOR

IV. EXPERIMENTAL STUDIES

The experimental effort during the first year of the program was directed toward three objectives: (1) to delineate in detail the regression rate behavior in the pressure-sensitive regime; (2) to begin defining the combustion instability mechanism in the same regime; and (3) to begin developing basic data on the structure of the boundary layer combustion process for eventual incorporation into an instability theory. During this year most of the effort centered on the first objective. This was the essential first step toward understanding combustion instability; before the latter can be described theoretically, it is necessary to understand the mechanism underlying regression rate dependence on pressure in the low-pressure regime, since instability is likely to result from the same mechanism. Studies on objectives 2 and 3 were relatively preliminary in character and will receive greater emphasis in future work, when the nature of combustion instability is investigated in more detail.

A. Measurements of Regression Rate Behavior in the Pressure-Sensitive Regime

Polyurethane and polybutadiene-acrylic-nitrile binders with varying aluminum loading were chosen as fuels and oxygen was used as the oxidizer in most of these tests. PU and PBAN were chosen for comparative binder tests because their surface behavior during regression is quite different. PU sublimes cleanly at the regressing surface, while the regression of PBAN consists of the stripping of hydrogen from the surface, leaving a carbonaceous char layer that subsequently breaks away in particular form.

Tubular burners of two sizes were used during the experimental studies. The smaller of the two was designed to accept $2\frac{1}{2}$-in. O.D. grains

whose internal port size and length could be chosen to suit the requirements of any given test. Two initial port sizes, 1 in. and $1\frac{1}{2}$ in. in diameter, were used. This burner was originally designed to operate with gaseous oxidizers (normally oxygen) and incorporated a tubular entrance section 12-in. long which is designed to deliver a smooth, uniform oxidizer flow to the head end of the grain. It can be operated at pressures up to 600 psia. During the later phases of this part of the investigation, this burner was modified for use with liquid fluorine.

A larger motor case that accepted 5-in. O.D. grains was also fabricated. This burner incorporated a liquid oxidizer injector, but may also be used with gaseous oxidizers if desired. Nitrogen tetroxide (N_2O_4) was used as the oxidizer for the tests carried out with this motor. It can also be operated at pressures up to 600 psia.

Appendix E provides a detailed description of the apparatus and procedures used in these experimental studies.

Initial data from the PU and PBAN propellant systems were concentrated at an oxidizer mass flux of approximately 0.1 $lb/in.^2$-sec. Data were obtained from 1-in.- and $1\frac{1}{2}$-in.-diameter motors at four pressure levels ranging from about 30 psia to about 260 psia (the exact pressure level for each firing is given in the figures that follow). Even though the nozzle was not always choked at the lowest pressure (the critical pressure ratio across the nozzle is 1.77 for $\gamma = 1.2$ corresponding to a chamber pressure of 26 psia), measurement of the regression rate is significant.

Figures 3 through 5 show the weight loss behavior as a function of time for the PBAN binder system containing 0, 20, and 40 percent aluminum in a 1-in. I.D. configuration. Similar data obtained from grains having an initial I.D. of $1\frac{1}{2}$ in. are shown in Figs. 6 through 8. In each case theoretical calculations are shown for the highest pressure level.

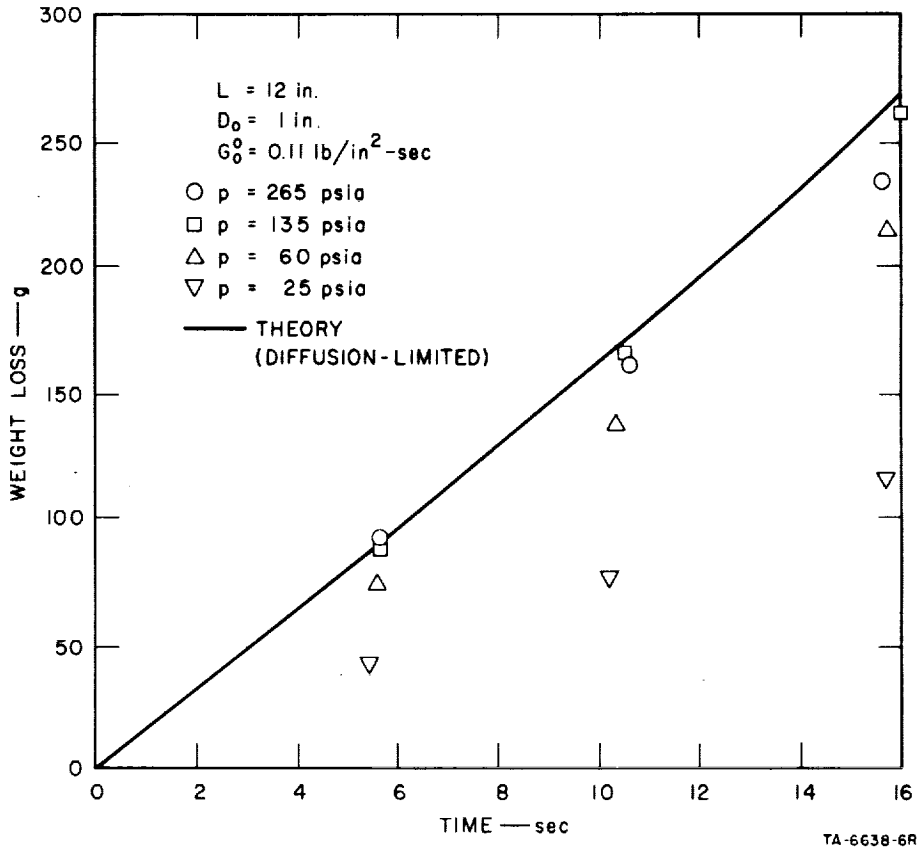

FIG. 3 WEIGHT LOSS OF A PURE PBAN HYBRID GRAIN (D_o = 1 in.)

It can be seen that there is a significant drop in weight loss (and therefore regression rate) as the pressure is lowered at all three metal loadings. At the highest pressure the weight loss agrees well with the calculated value based upon diffusion-limited theory.

Typical chamber pressure traces measured at the head end of the grain for two of the PBAN systems at high and low pressure are shown in Figs. 9 and 10. It can be seen that the pressure trace from the aluminized grain is more ragged at high pressure. The initial small pressure rise noted during the first stages of the high-pressure runs is caused by the preflow during the ignition period.

A more interesting presentation of the regression rate data can be obtained by plotting the weight loss at a given pressure divided by

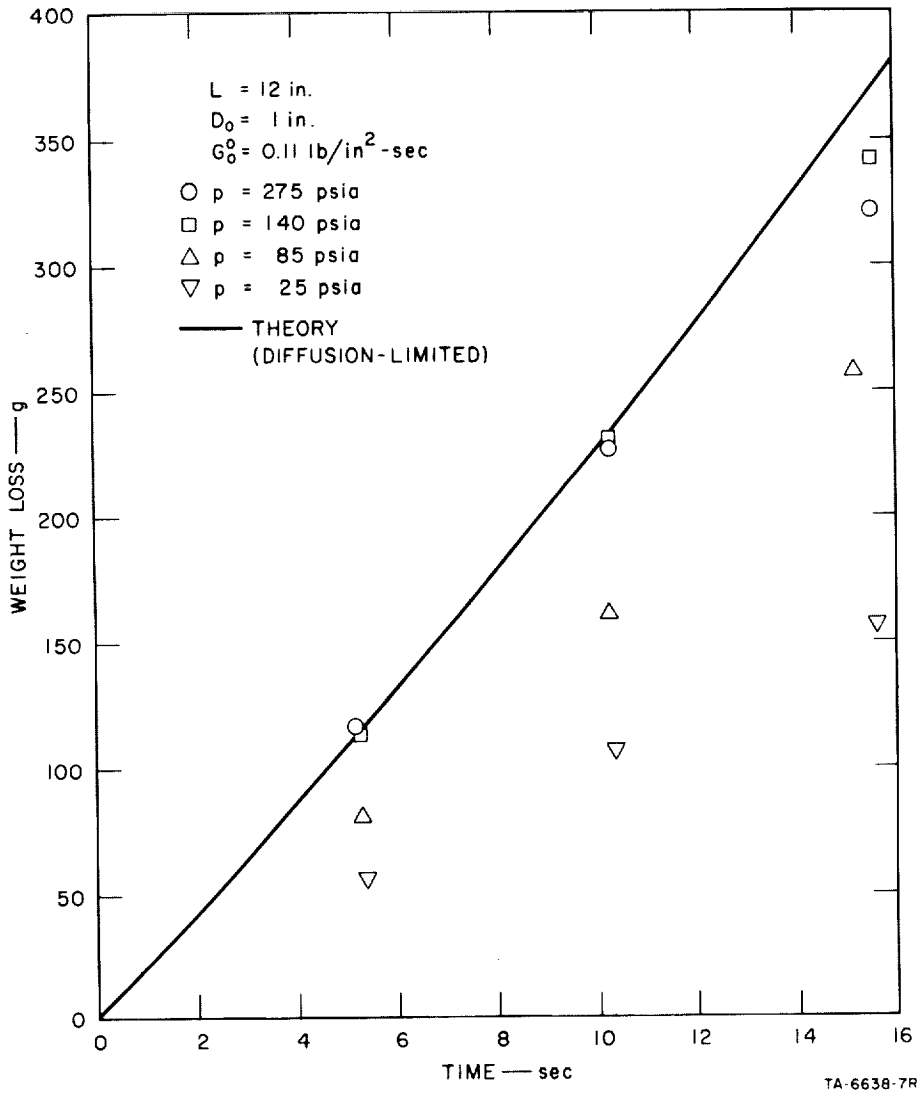

FIG. 4 WEIGHT LOSS OF A PBAN HYBRID GRAIN CONTAINING 20 PERCENT ALUMINUM (D_o = 1 in.)

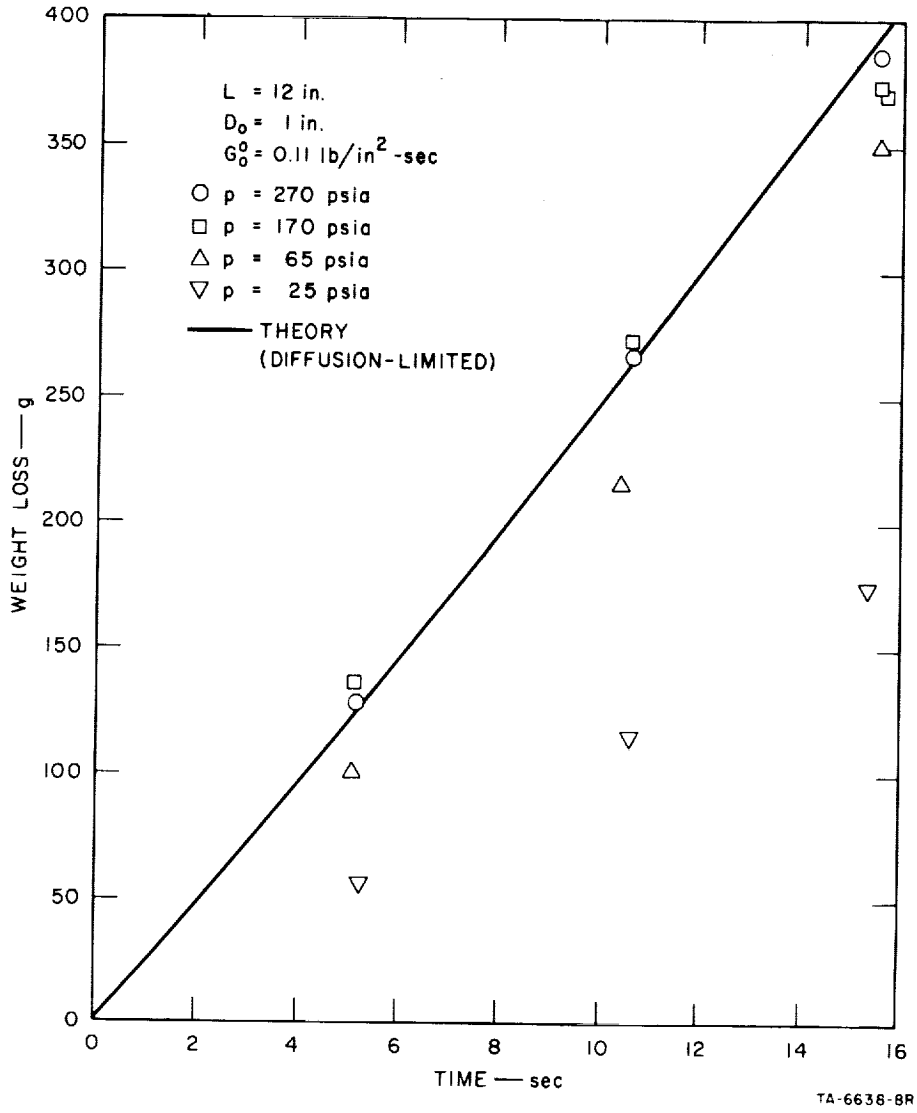

FIG. 5 WEIGHT LOSS OF A PBAN HYBRID GRAIN CONTAINING 40 PERCENT ALUMINUM (D_o = 1 in.)

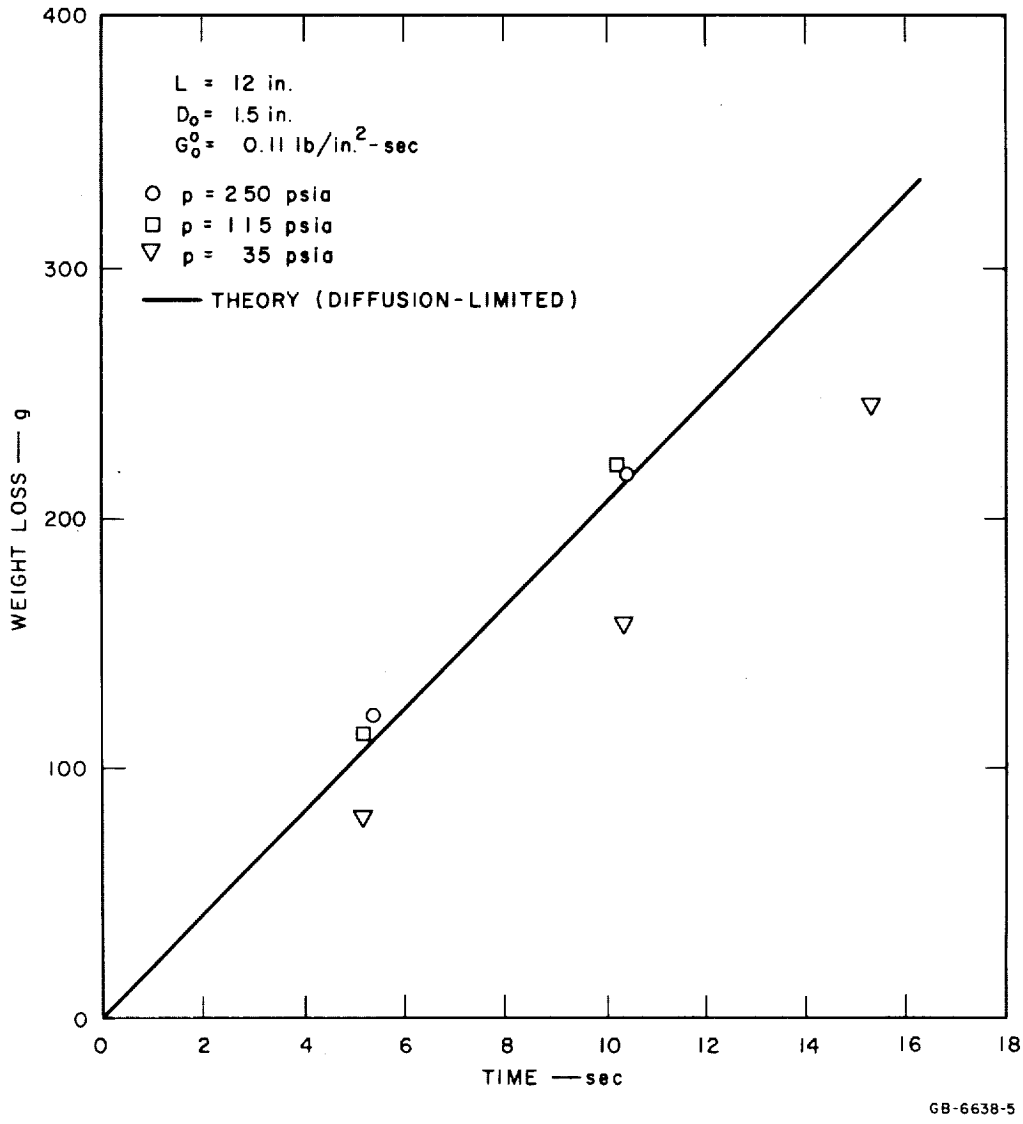

FIG. 6 WEIGHT LOSS OF A PURE PBAN HYBRID GRAIN (D_o = 1.5 in.)

the weight loss at the highest pressure as a function of pressure. At any given time this curve will depict the behavior of the average regression rate up to that time. Results for the 1-in.- and $1\frac{1}{2}$-in.-diameter PBAN runs are plotted in this manner in Figs. 11 and 12. The data show a similar pressure dependence for both diameters and show that the regression rate decays to approximately 0.4 of its high pressure value at 1 atm.

It is also evident from Figs. 11 and 12 that there is a scatter of approximately ±10% in the data points obtained from weight loss measurements.

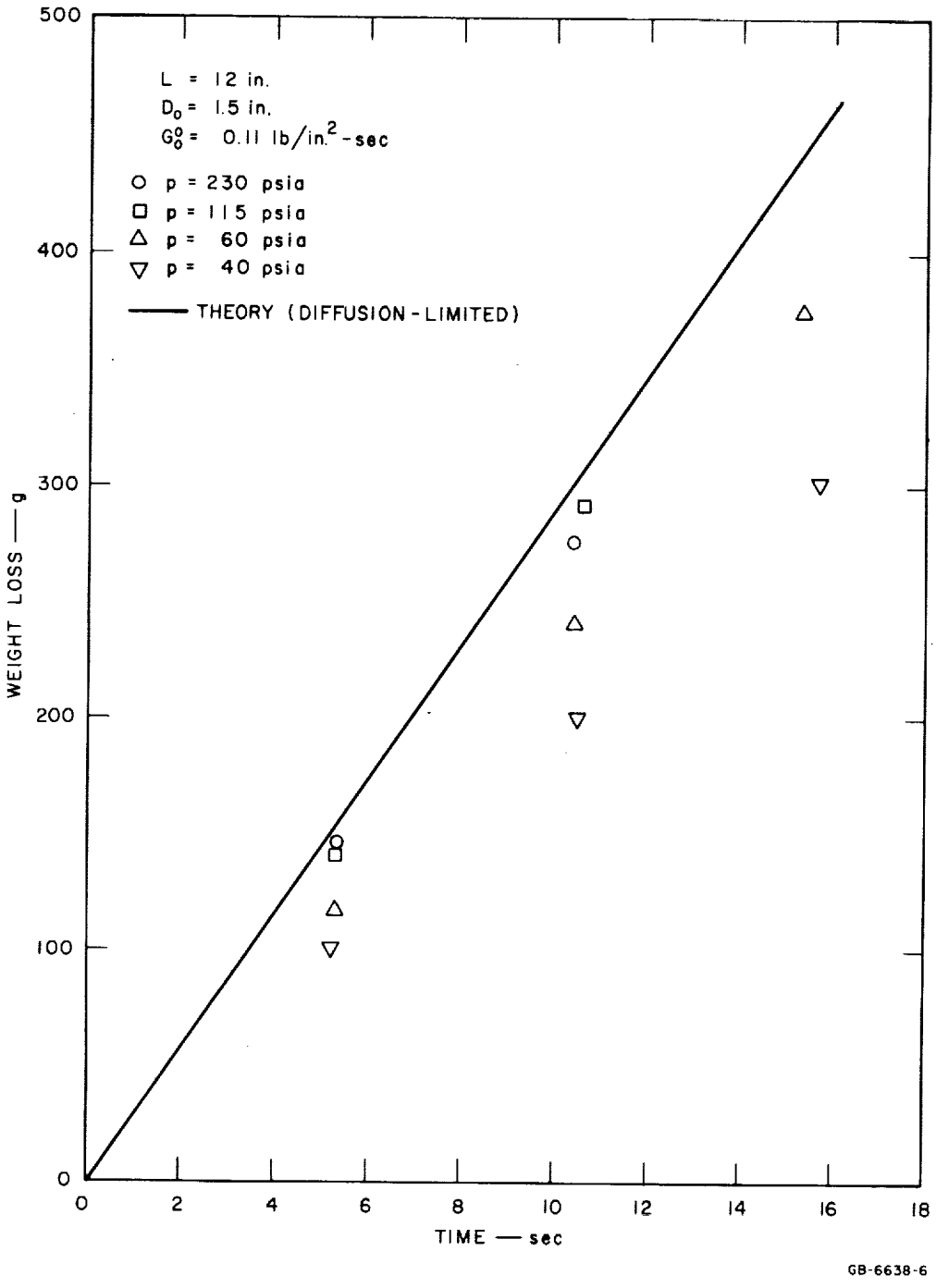

FIG. 7 WEIGHT LOSS OF A PBAN HYBRID GRAIN CONTAINING 20 PERCENT ALUMINUM (D_o = 1.5 in.)

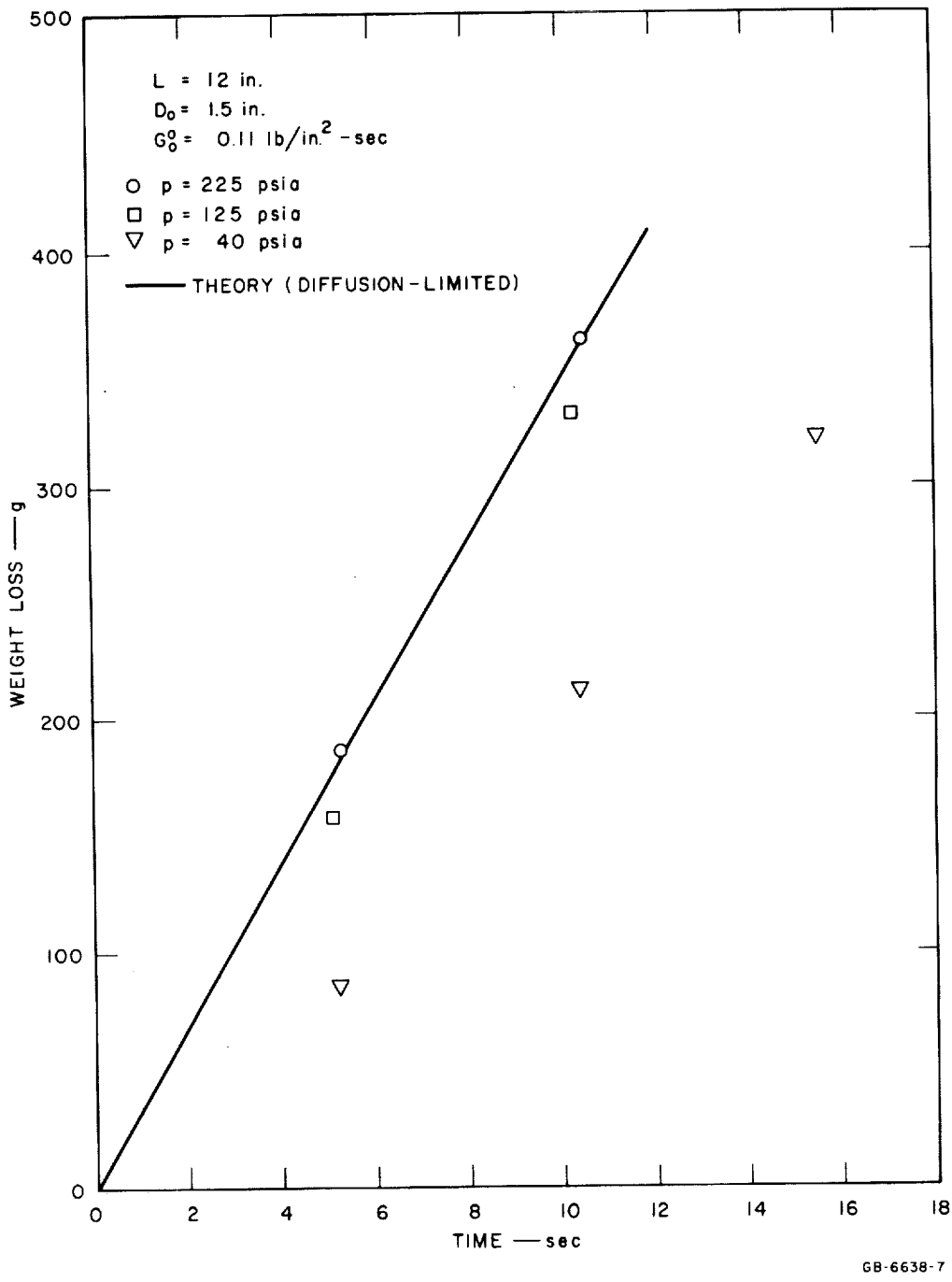

FIG. 8 WEIGHT LOSS OF A PBAN HYBRID GRAIN CONTAINING 40 PERCENT ALUMINUM (D_o = 1.5 in.)

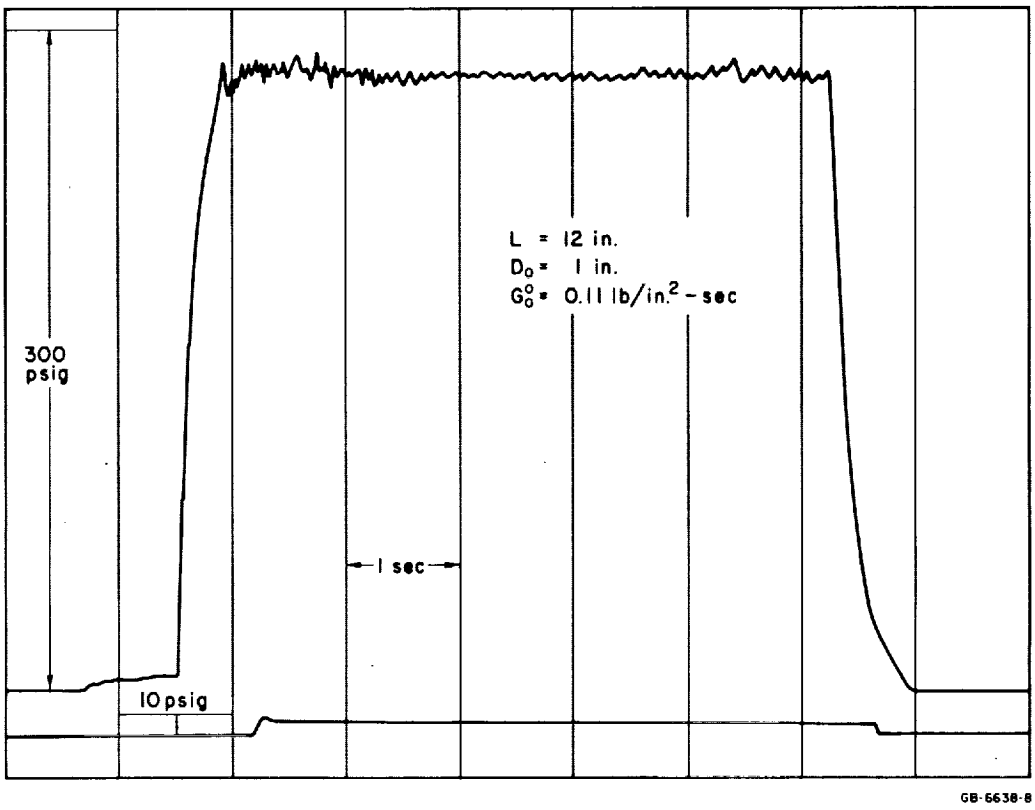

FIG. 9 TYPICAL CHAMBER PRESSURE TRACES FROM THE FIRING OF A PURE PBAN HYBRID GRAIN

The agreement between theory and experiment obtained at high pressure shown in the previous figures is much closer, indicating that most of the scatter makes its appearance in the kinetically dominated regime. In general, however, regression rate data obtained from weight loss measurements exhibit scatter because they represent the quotient of two measured quantities, with the inherent possibility of doubling the experimental errors.

Finally, in Figs. 11 and 12, both of the regression rates averaged over 5 and 10 sec exhibit nearly identical behavior, as would be expected since the change in oxidizer mass flux between the two times is not significant.

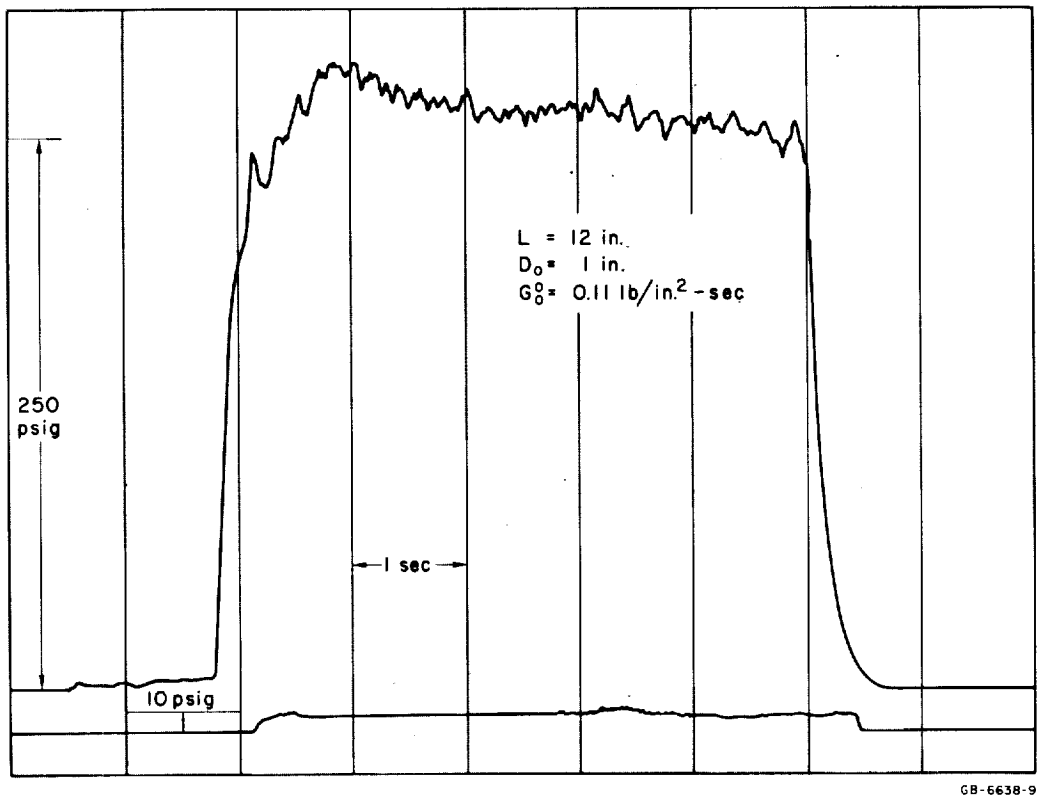

FIG. 10 TYPICAL CHAMBER PRESSURE TRACES FROM THE FIRING OF A PBAN HYBRID GRAIN CONTAINING 40 PERCENT ALUMINUM

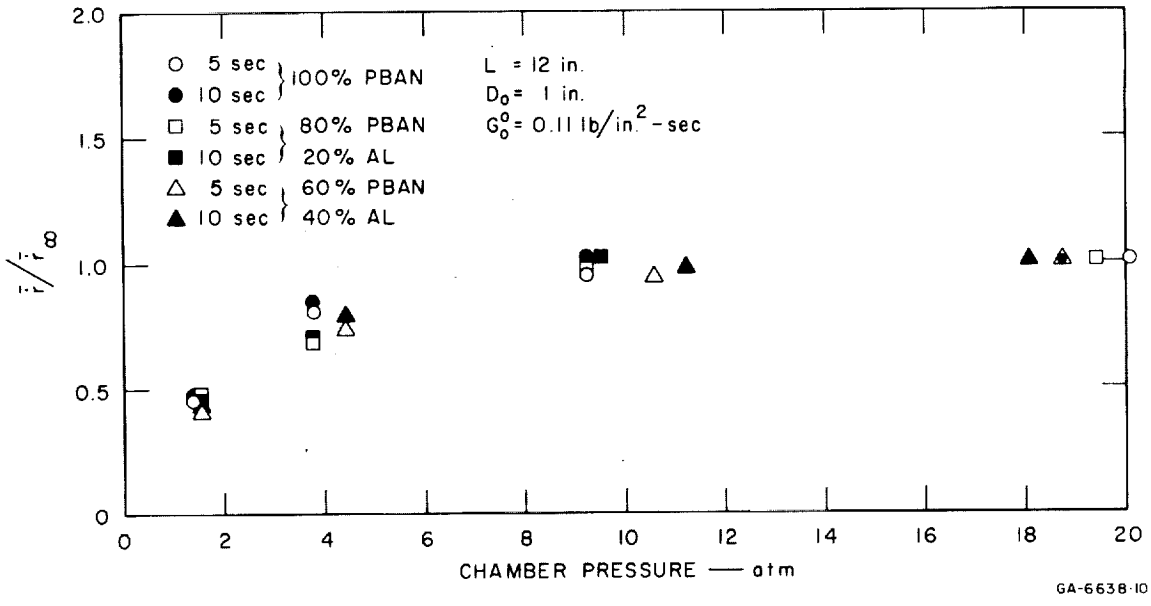

FIG. 11 EXPERIMENTAL DEPENDENCE OF REGRESSION RATE ON PRESSURE FOR THE ALUMINIZED PBAN-OXYGEN HYBRID SYSTEM (D_o = 1 in.)

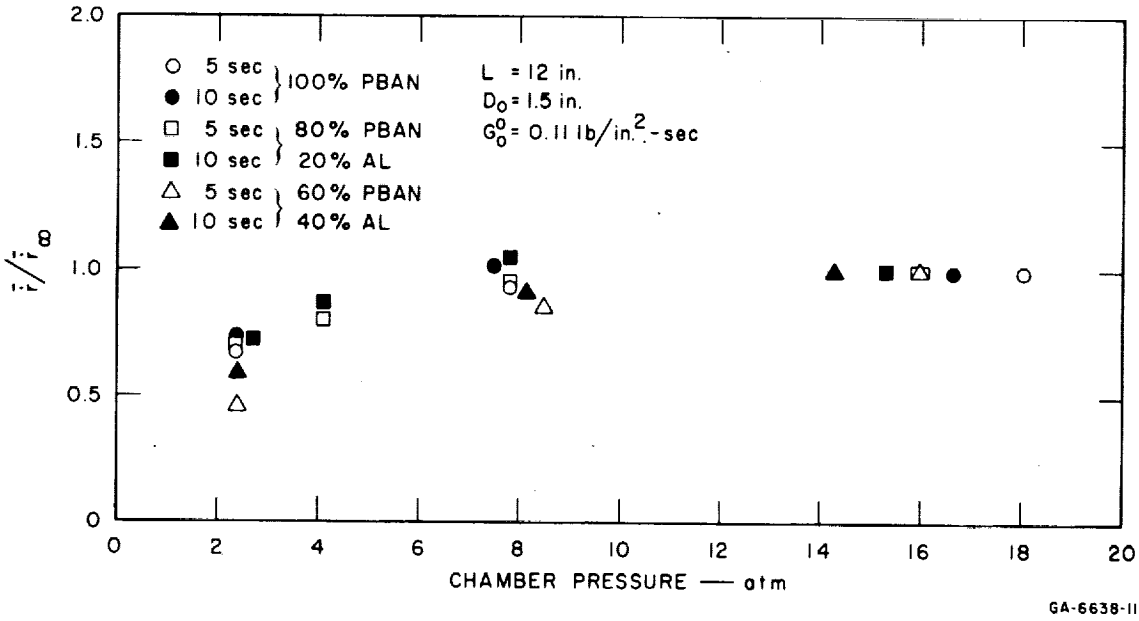

FIG. 12 EXPERIMENTAL DEPENDENCE OF REGRESSION RATE ON PRESSURE FOR THE ALUMINIZED PBAN-OXYGEN HYBRID SYSTEM (D_o = 1.5 in.)

Weight loss data for aluminized PU grains are given in Figs. 13 through 15. These data show a similar dependence of regression rate on pressure to that observed in the PBAN system discussed previously. For this reason no tests were run in a $1\frac{1}{2}$-in. initial port diameter configuration. Results of tests with varying flow, which are discussed in detail below, are also shown in Figs. 13 through 15. The dependence of the regression rate of the PU grains on pressure will be discussed in a later section.

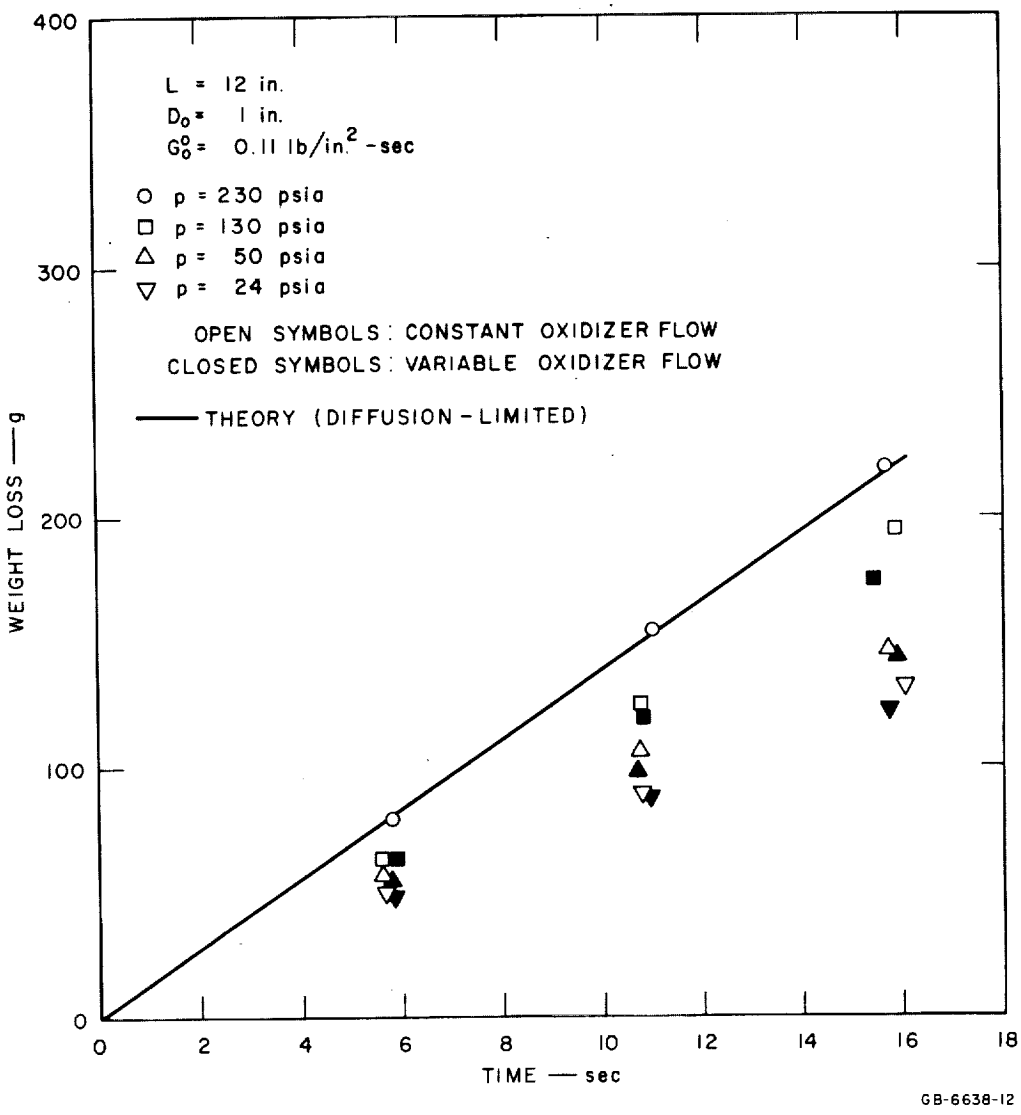

FIG. 13 WEIGHT LOSS OF A PURE PU HYBRID GRAIN (D_o = 1 in.)

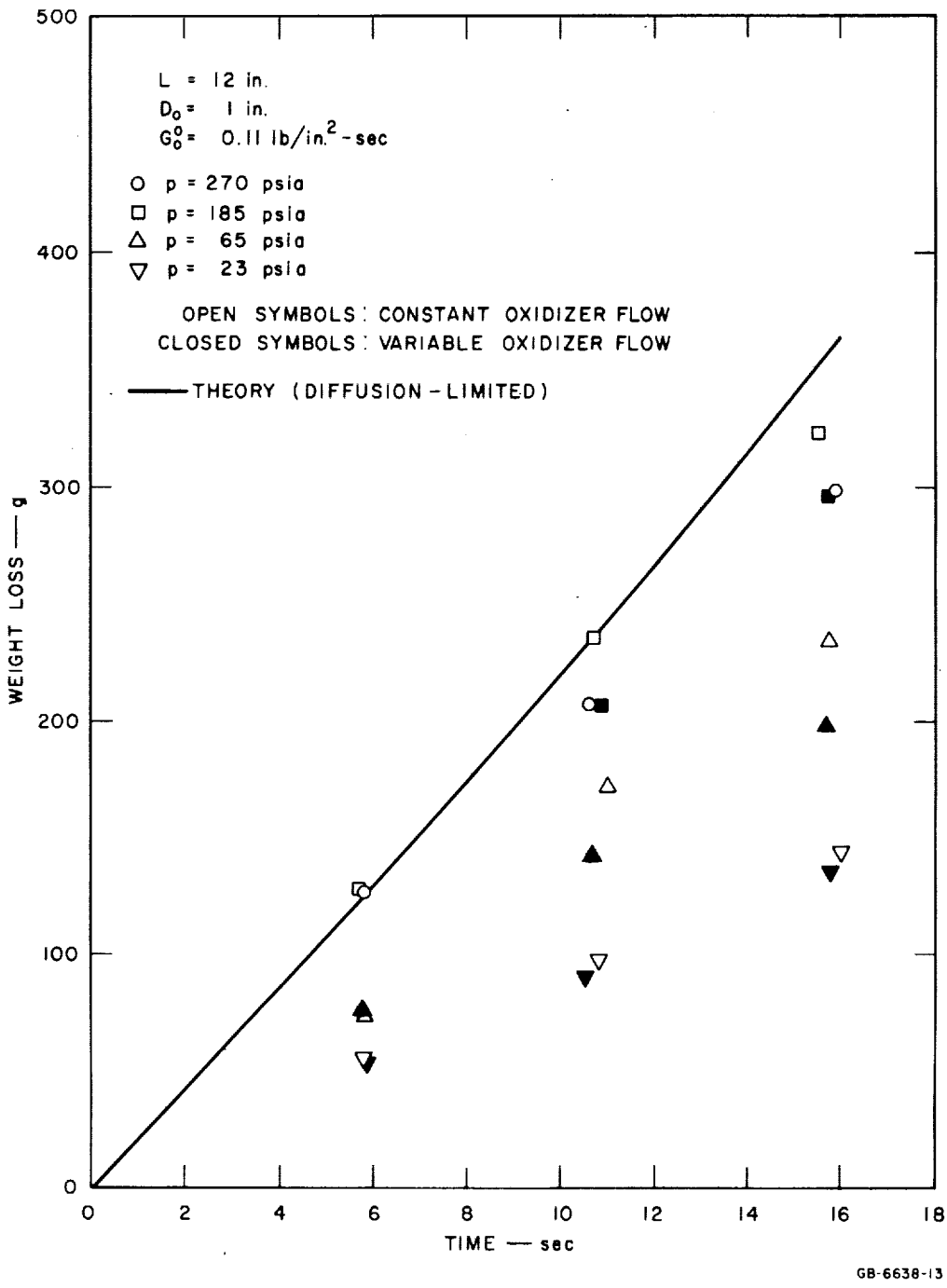

FIG. 14 WEIGHT LOSS OF A PU HYBRID GRAIN CONTAINING 20 PERCENT ALUMINUM (D_o = 1 in.)

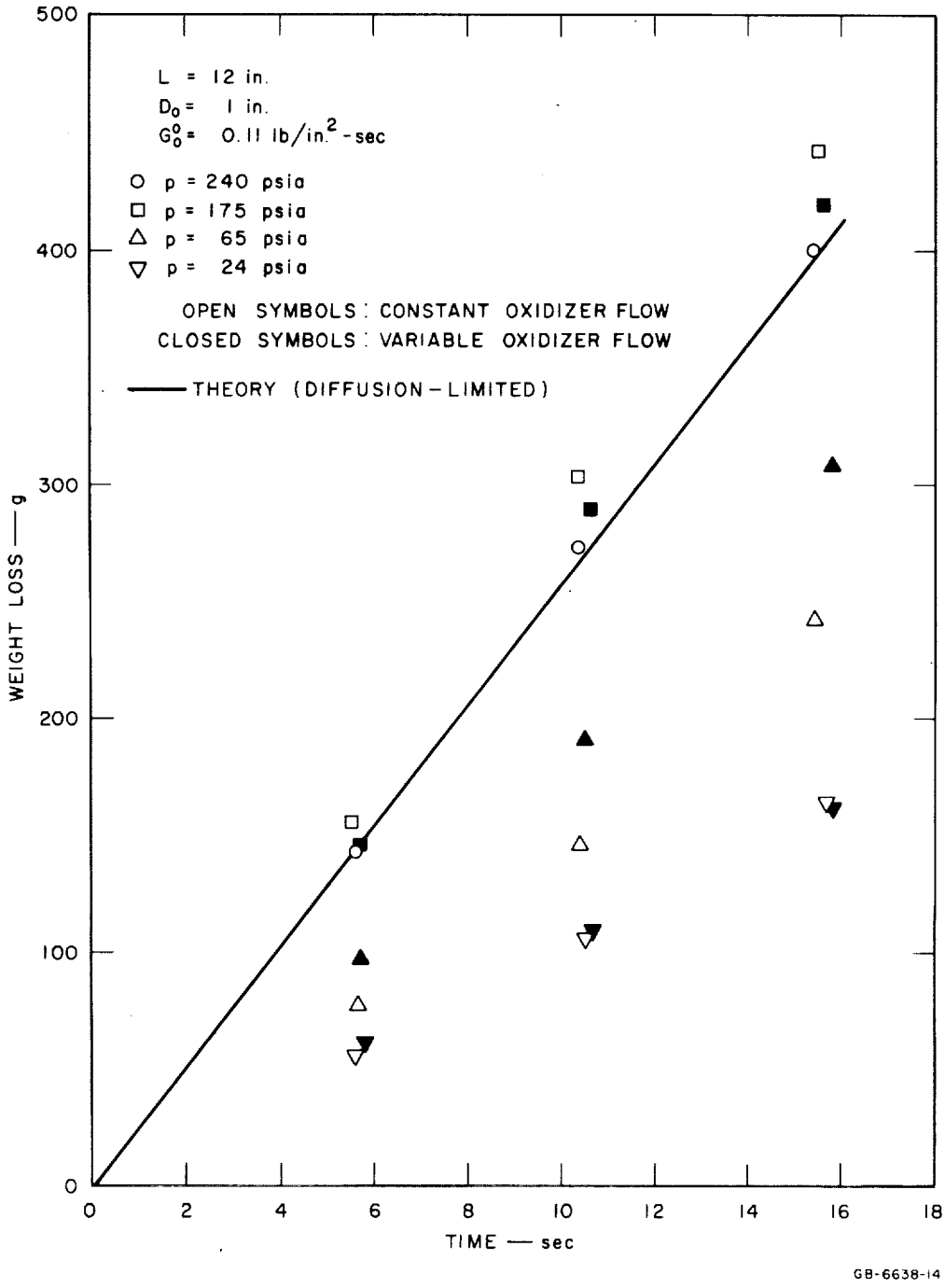

FIG. 15 WEIGHT LOSS OF A PU HYBRID GRAIN CONTAINING 40 PERCENT ALUMINUM (D_o = 1 in.)

B. Experiments with Variable Mass Flow and Variable Chamber Pressure

In the pressure-sensitive domain of hybrid combustion the pressure sensitivity may give rise to an acoustical instability, characterized by the "acoustical admittance," which is defined as the ratio of the regression rate perturbation induced by a given pressure perturbation to the pressure perturbation, or $\Delta r/\Delta p$. As pointed out earlier, the derivation of an analytical expression for the acoustic admittance depends on the initial formulation of an expression for the steady-state regression rate/pressure dependence; this has been the object of the theoretical and experimental work described above.

Experiments to be described below were conducted to define the conditions under which hybrid instability arises and to delineate the coupling mechanism. It is well known that solid propellants exhibit unstable behavior at frequencies of the order of hundreds of cycles per second.[16,19] Since the regression rates of the hybrid systems being considered here are only on the order of one-quarter of typical solid propellant burning rates, and since the characteristic frequency of maximum response depends on the square of the burning rate, it was decided to conduct a few preliminary oscillatory experiments by oscillating the oxidizer flow and the nozzle throat area at about 10 cps while observing the resulting chamber pressure. This procedure makes it possible to distinguish different coupling mechanisms.

The oxidizer mass flow can be held constant during nozzle throat area variations by employing a sonic choke at the inlet. On the other hand, mass flux perturbations that are introduced by oxidizer flow variations will give rise to pressure perturbations that are induced by the varying mass flow through the nozzle. In fact, these pressure perturbations can

be used as a measure of the mass flux perturbations. Obviously, great care must be taken in the subsequent interpretation of results to carefully separate pressure and mass flux effects.

Another facet which must be carefully considered is the chamber response. An oscillating oxidizer mass flow will not introduce a corresponding mass flux oscillation in the chamber if the chamber response function is highly damped at the frequency of interest. Obviously, the chamber response function must be understood and known before the regression rate response can be correctly deduced. This point is discussed in detail in Appendix F. In Fig. 16 the calculated chamber response is shown for two cases, isothermal and isentropic behavior. The isothermal response is of course somewhat lower than the isentropic response, owing to losses in the isothermal case.

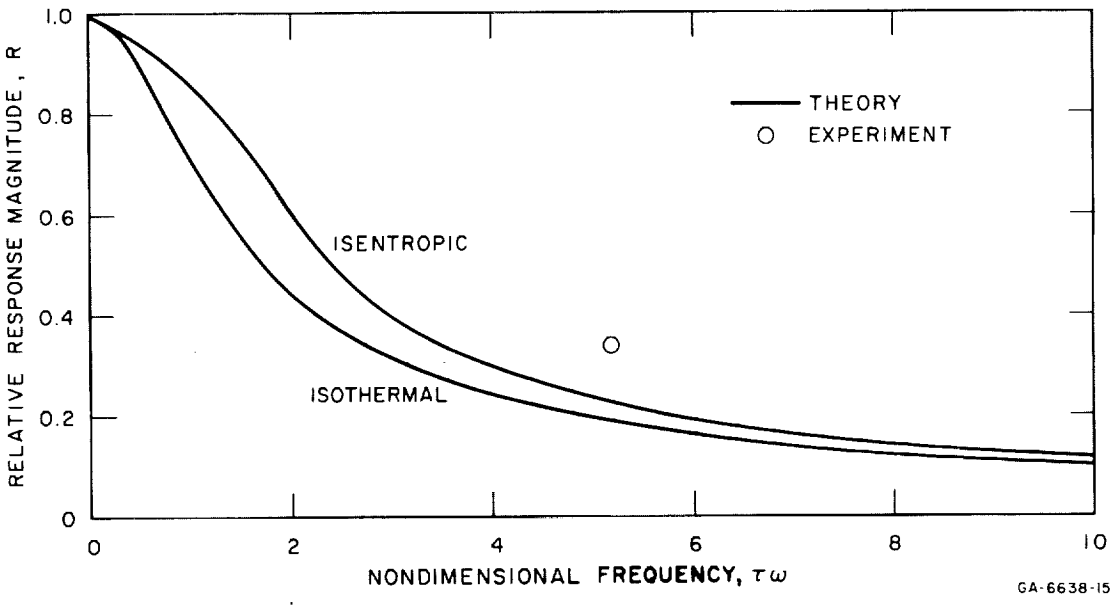

FIG. 16 CHAMBER PRESSURE RESPONSE OF THE HYBRID TEST MOTOR TO OXIDIZER FLOW PERTURBATIONS

The salient fact that emerges from a consideration of Fig. 16 is that the pressure response is very low at the higher values of frequency. Since this response is a measure of the mass flux perturbation in the chamber, it is evident that at, say, 35 cps a very large upstream oxidizer mass flow perturbation will be required to obtain a relatively small mass flux perturbation in the chamber.

A similar calculation could be made for the variable pressure-constant mass flux case. The general shape of the solution would show a similar frequency dependence. It is clear that care must be taken to avoid attributing chamber response effects to the propellant response which is of main interest.

The experimental systems used for the oscillatory oxidizer flow and chamber pressure studies are shown in Figs. 17 and 18. A ball valve which is driven by a variable speed motor was inserted in the oxidizer flow line just above the inlet sonic choke (see Fig. 17) to provide flow variations. The frequency of oscillation is determined by the speed of the motor and the peak amplitude by the upstream pressure. To achieve chamber pressure oscillations separately, a nozzle slug assembly was built as shown in Fig. 18. The maximum frequency obtainable from both the ball valve and the oscillating probe was limited to about 30 cps by mechanical inertia.

Two experimental results are of particular interest in these two tests: first the determination of whether the mean regression rate (corresponding to the mean pressure) is changed by the presence of the oscillation, and second, the comparison of the observed magnitude of the chamber pressure oscillation to the computed magnitude, which is based upon a quasi-steady relationship between regression rate and pressure.

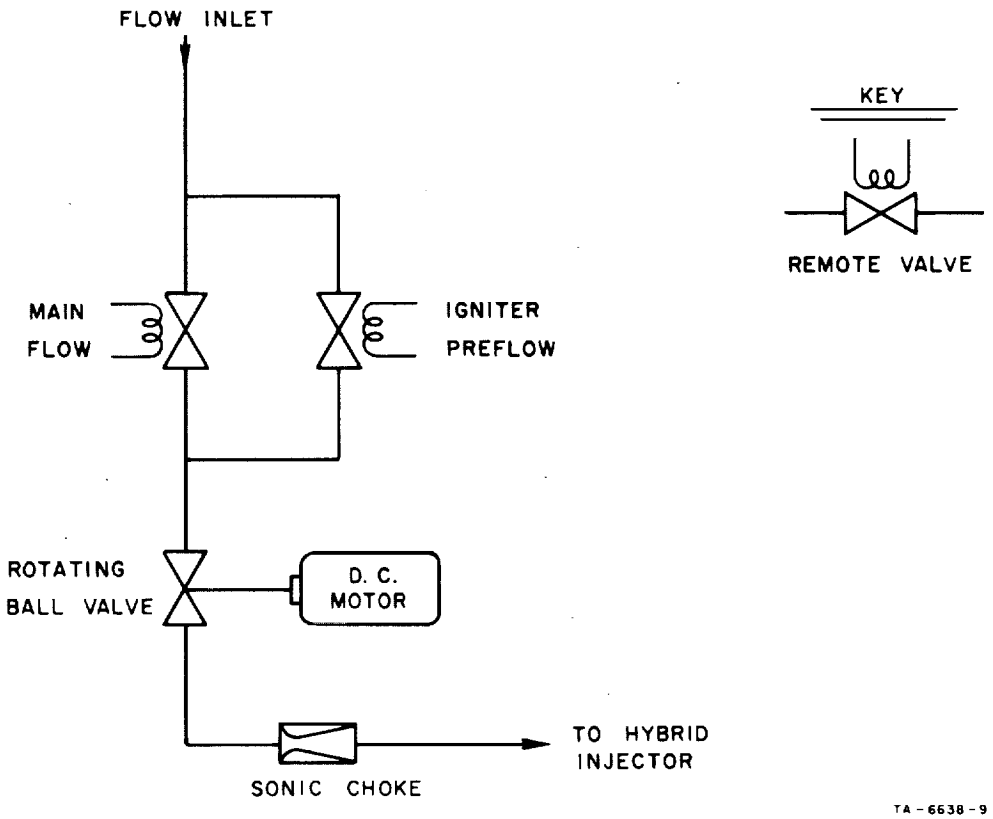

FIG. 17 LAYOUT OF FLOW SYSTEM FOR OSCILLATORY OXIDIZER FLOW STUDIES

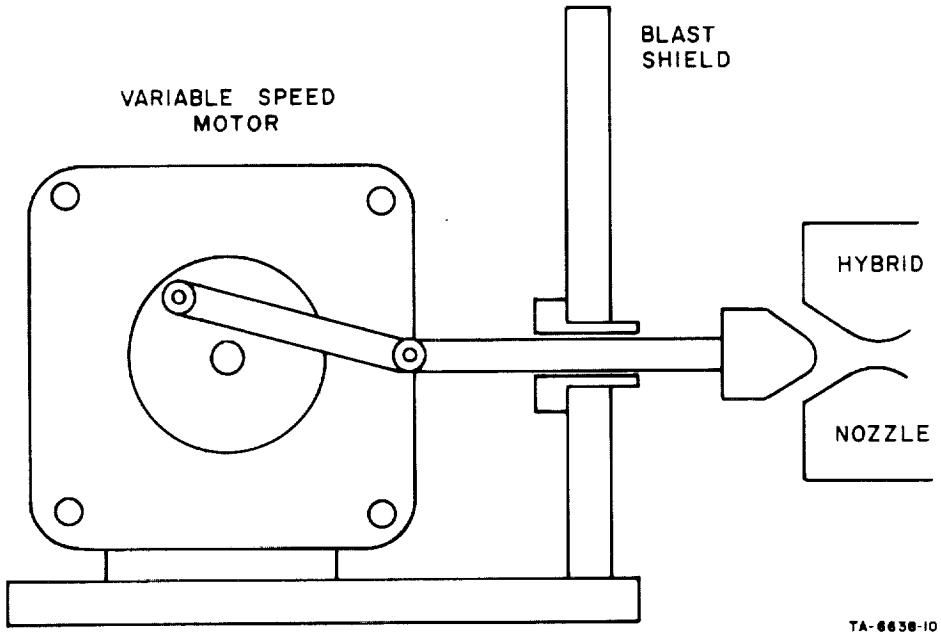

FIG. 18 DRIVE MECHANISM FOR OSCILLATORY CHAMBER PRESSURE STUDIES

Weight loss data obtained in the PU system under conditions of varying flow were previously shown in Figs. 13 through 15. The mass flux was varied approximately by a factor of 2 at a frequency of about 10 cps. It can be seen that the variable flow rate data follow the same trends as the constant flow rate data with no discernable differences. Similar results were obtained in the PBAN system and for pressure changes induced by a variable throat area. A complete summary of all mean regression rate data is presented in a later section.

For a typical run in which the mass flux was varied between 0.075 and 0.15 $lb/in.^2$-sec (with an average value of 0.11) at 12 cps, the chamber pressure was observed to oscillate with an amplitude of ± 7 psi at an average value of 43 psia. Using representative values of V = 20 $in.^3$ and T = 5000°R, the calculated value of the nondimensional frequency $\tau\omega$ is 5.2 and the value of the response is 0.35. As shown in Fig. 16, this response is approximately 50 percent higher than the calculated quasi-steady value. Thus, although the mean regression rate is undisturbed by the oscillating mass flux, evidence of a propellant response is apparent. Further interpretation of this data must await the theoretical analysis of the transient regression rate behavior, which is planned for the second year of the program.

C. Instability Observations

The mean regression rate data reported above, obtained for both 1-in.- and 1.5-in.-diameter grains, exhibited a similar mean regression rate/

pressure dependence for both grain sizes. However, during the burning of the 1.5-in.-diameter grains, an instability wave was observed to develop when the tube diameter reached approximately 1.75 in. This event appears to be an inherent instability in the combustion process.

Typical wave forms for the PBAN-oxygen propellant system operating at a mean pressure of 2.5 atm are shown in Fig. 19. The upper trace in

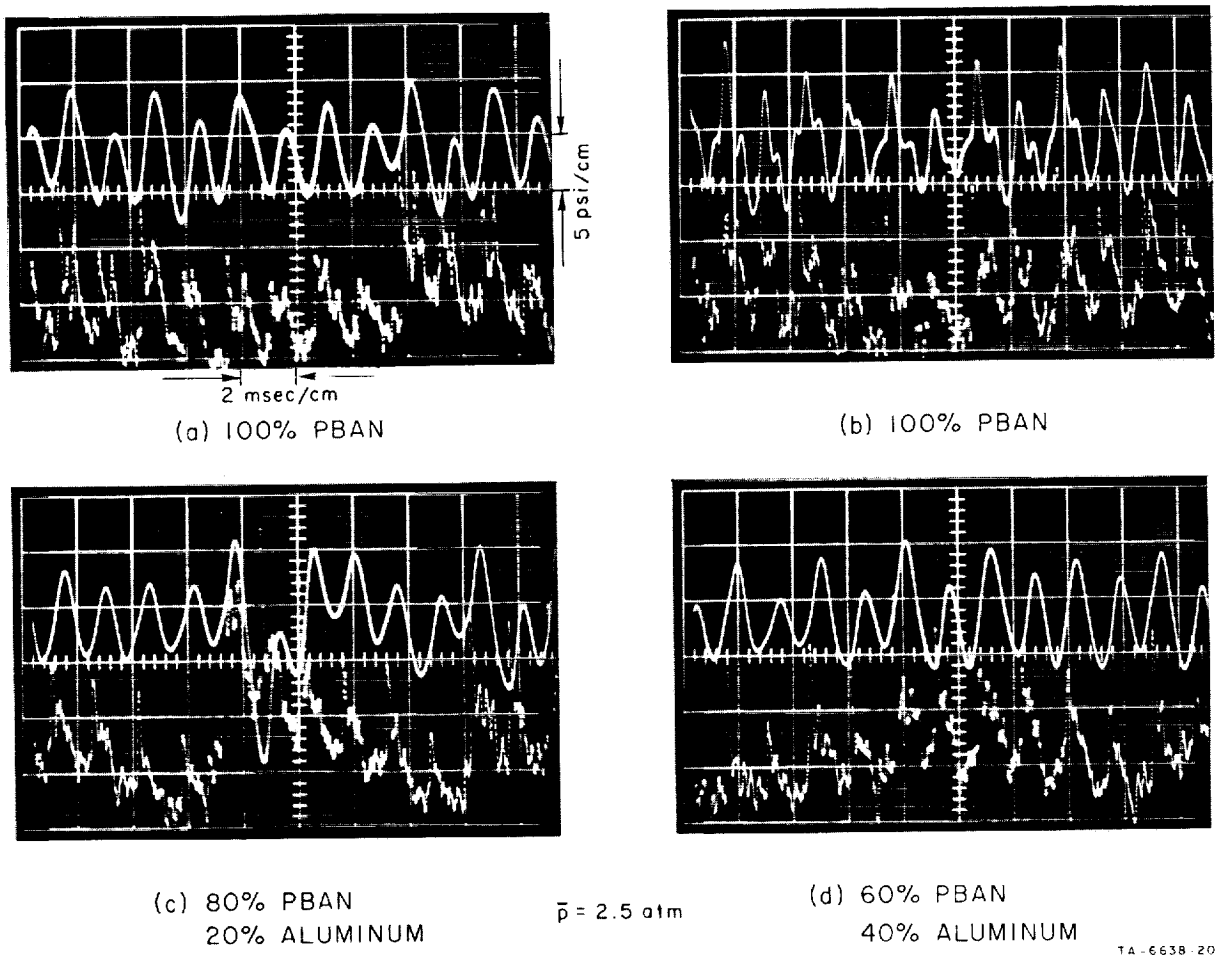

FIG. 19 INHERENT HYBRID INSTABILITY WAVE OBSERVED AT LOW PRESSURE IN PBAN-OXYGEN PROPELLANT SYSTEM

each chart is the energy in the frequency band between 150 and 1500 cps. At this mean pressure level the mean regression rate is approximately 0.6 of the asymptotic value at high pressure. The frequency of the predominant mode is about 650 cps, and the peak-to-peak amplitude of the wave is of the order of 10 psi, or 25 percent of the mean pressure. This wave form has been observed with all metal loadings up to 40 percent, as shown in Fig. 19. Such behavior is consistent with the previous observation that all formulations exhibited the same regression rate/pressure dependence. It is not surprising that the presence of metal particles has no damping effect, because the observed frequency is too low to be affected by particle damping phenomena. Of perhaps more fundamental importance is the observation that the addition of burning metal particles does not influence either the dependence of the mean burning rate on pressure or the frequency of the observed instability wave. Such behavior implies that the burning process (i.e., flame speed) of the volatile products released by the vaporization of the binder is of primary importance in establishing the pressure-dependent regime of hybrid combustion.

The rather low frequency which is observed indicates the excitation of a longitudinal rather than a transverse mode. In this connection it was found during the studies with variable mass flow that a very low frequency variable mass flow had a definite effect on the instability process. Typical results for the unfilled PBAN binder system are shown in the sequence of photographs presented in Fig. 20. The mass flux was varied 30 percent at a frequency of approximately 10 cps. Photograph (a) shows that on the average the disturbance is magnified near peak values of the mass flux (or chamber pressure, since the two are interrelated) and damped near trough values. Photographs (b) and (c) show the behavior near a peak at progressively faster sweep rates. The upper trace is again filtered to show the energy between 150 and 1500 cps. In this case the

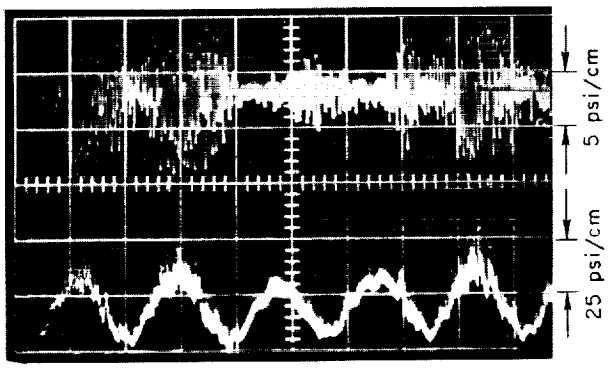

(a) 50 msec/cm SWEEP RATE

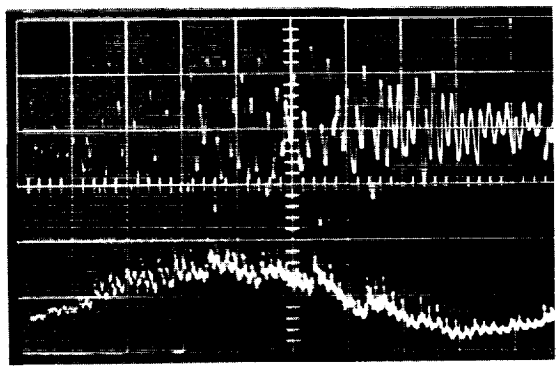

(b) 10 msec/cm SWEEP RATE

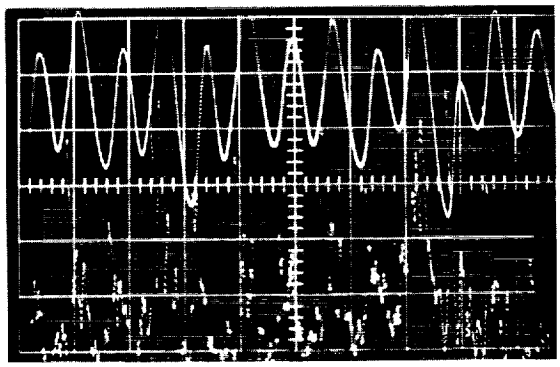

(c) 2 msec/cm SWEEP RATE

$\bar{p}$ = 6 atm

TA-6638-21

FIG. 20 EFFECT OF MASS FLOW VARIATIONS ON LOW PRESSURE INSTABILITY IN PURE PBAN-OXYGEN PROPELLANT SYSTEM

instability amplitude is about 15 psi at a mean pressure level of about 90 psia. The frequency is about 650 cps as before.

Figure 21 shows the behavior of the unfilled PBAN binder system operating at 15 atm with a steady oxidizer flow rate. At this pressure level the mean burning rate is accurately predicted by the heat-transfer-limited theory, and a severe pressure-coupled instability would not be expected. Figure 21 shows that a small pressure disturbance of about 10 psi (compared to a mean level of 225 psia) is present; this disturbance does not exhibit the pure waveform of the instability observed at lower pressures. It is also of interest to note that the lower unfiltered trace

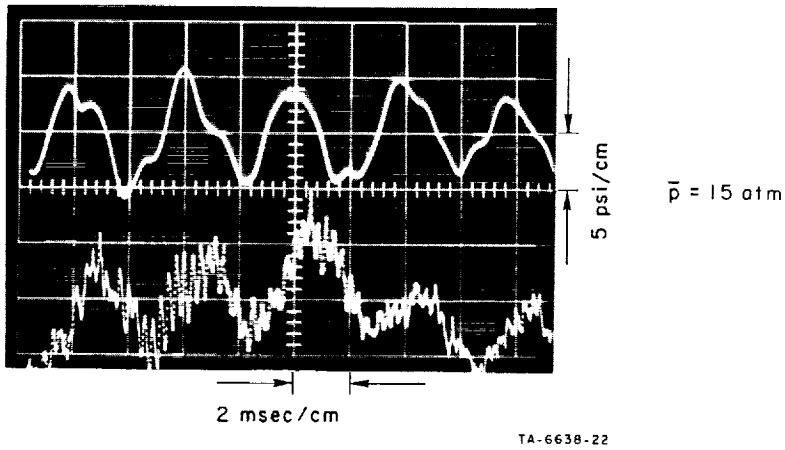

FIG. 21 INSTABILITY WAVE OBSERVED AT HIGH PRESSURE IN PURE PBAN-OXYGEN PROPELLANT SYSTEM

contains a 2-psi wave at a frequency of about 3500 cps. This high-frequency wave may represent a transverse mode of instability. In all cases the instability arose spontaneously without external excitation.

According to the thermochemical calculations presented in Appendix G the value of the specific heat ratio γ is approximately 1.2 for all of the PU and PBAN propellants. The critical pressure ratio across the exit nozzle required to maintain sonic flow at the throat is given by

$$\frac{p_c}{p_a} = \left(\frac{\gamma + 1}{2}\right)^{\frac{\gamma}{\gamma - 1}} \qquad (6)$$

For $\gamma = 1.2$, the value of this ratio is 1.77, giving $p_c = 26$ psia for standard conditions. The lowest experimental mean pressure ratio was 2.5 with a sinusoidal variation of $\pm$ 0.3. Therefore, the observed behavior cannot be attributed to an unsteady choking and unchoking of the nozzle.

Assuming that the wave is longitudinal in nature (i.e., an organ pipe oscillation), the average wave speed can be calculated as twice the

length of the chamber (4 ft) times the measured frequency of the wave:

$$u_w \cong 4(650) = 2600 \text{ ft/sec}$$

At first glance, this speed appears to be lower than the speed of sound one would expect in the hybrid motor. However, two points must be borne in mind: First, the motor configuration used in these studies consisted of a 12-in.-long straightening section upstream of the grain. In this section the temperature, and therefore the speed of sound, is low. Second, the cool core in the motor itself will tend to decrease the average sonic speed. The result is that the observed wave speed is a complicated product of the environment. Future tests involving different chamber lengths will be carried out to determine the influence of the coupling between chamber length and propellant response.

The question of fundamental interest is how the propellant response acts as a driving mechanism to support the wave under certain circumstances, i.e., with a certain motor diameter at a given oxidizer mass flux. This question will be investigated in detail during the future phases of the program.

D. Regression Rate Measurements with Fluorine

In addition to the many experiments described previously with oxygen as the oxidizer component of the propellant system, a few runs were made with liquid fluorine as the principal oxidizer with only enough oxygen to burn the carbon in the binder to CO. Two fuel systems were used, 100 percent PU and 80 percent PU/20 percent Al. The objective of these experiments was to compare the low-pressure regression rate behavior of the fluorine propellant system with that of the oxygen propellant system. The total number of fluorine runs was limited by the operating costs of the cryogenic system.

A photograph of the test apparatus used in the fluorine runs is included as Fig. 22. The dewar flask contains a liquid nitrogen bath in which all components of the fluorine system up to the injector face are contained. Figure 23 shows the internal assembly, including the fluorine tank that is pressurized by helium and the coil that is used to liquify the fluorine. The injector consists of a simple central hole (0.055 in. in diameter) for the fluorine with a coaxial annulus (0.085 in. clearance) for the oxygen. Figure 24 is a diagram of the injector. The entire assembly up to but not including the pneumatic actuators for the valves is immersed in liquid nitrogen. Figure 25 is a schematic diagram of the fluorine system. The liquid fluorine, pressurized with gaseous helium is metered through a cavitating venturi. The injector is prechilled with

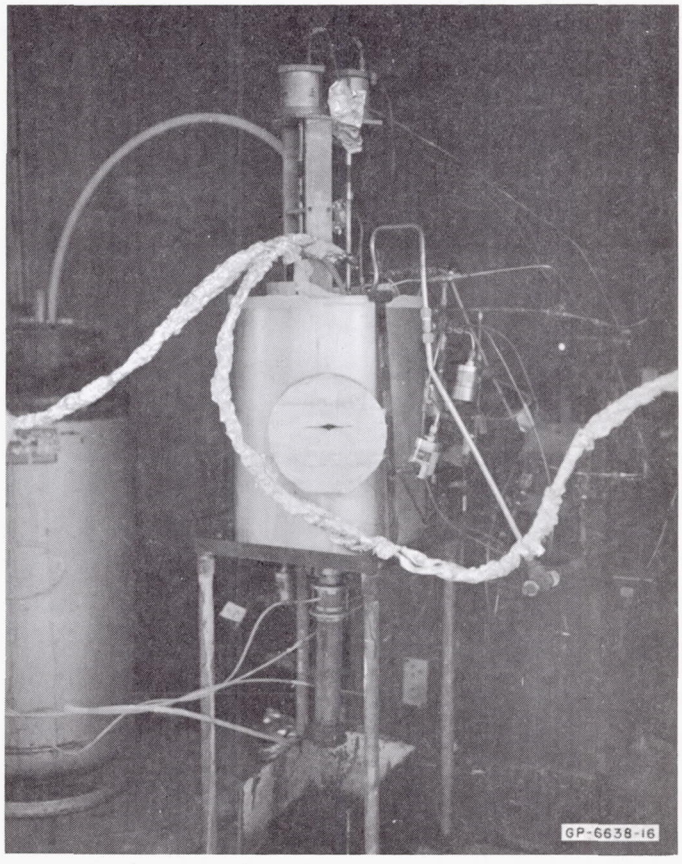

FIG. 22 FLUORINE HYBRID SYSTEM ASSEMBLY

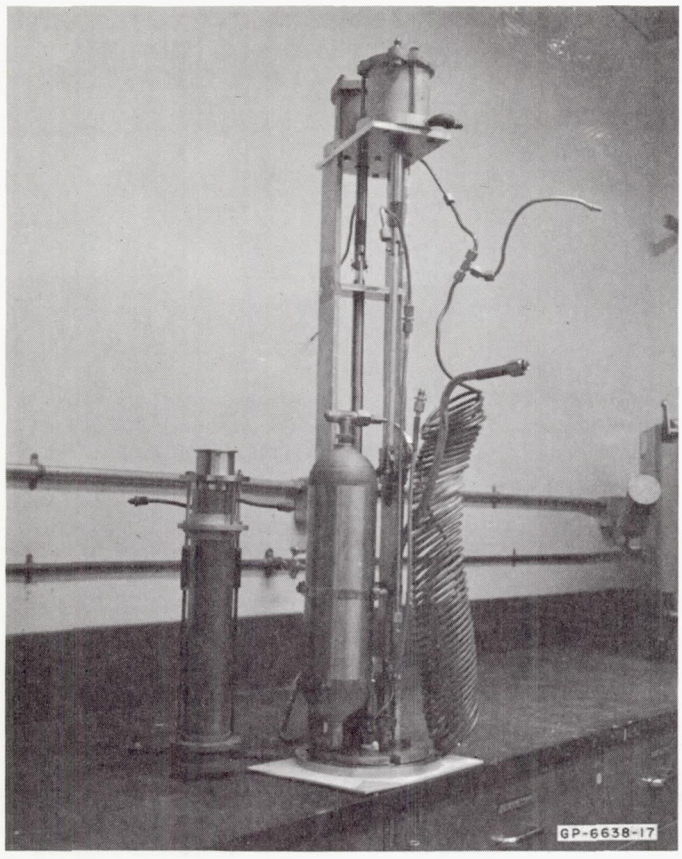

FIG. 23 INTERNAL ASSEMBLY OF FLUORINE SYSTEM

liquid nitrogen and the nozzle is cooled with circulating water. Note that no flow-straightening section such as that used in the tests with gaseous oxygen is required upstream of the grain because the rapid evaporation and expansion of the fluorine fills the inlet section uniformly.

Weight loss data obtained from aluminized PU grains (0 and 20 percent Al), are given in Figs. 26 and 27. The ratio of fluorine to oxygen was approximately 3:1; only enough oxygen was used to convert the carbon in the binder to carbon monoxide. Runs were made for 3 and 6 seconds instead of the 5 and 10 seconds used in the oxygen case to limit the total heat transfer back to the cryogenic system. Also shown in the figures is the transport-limited regression rate calculated with the hybrid

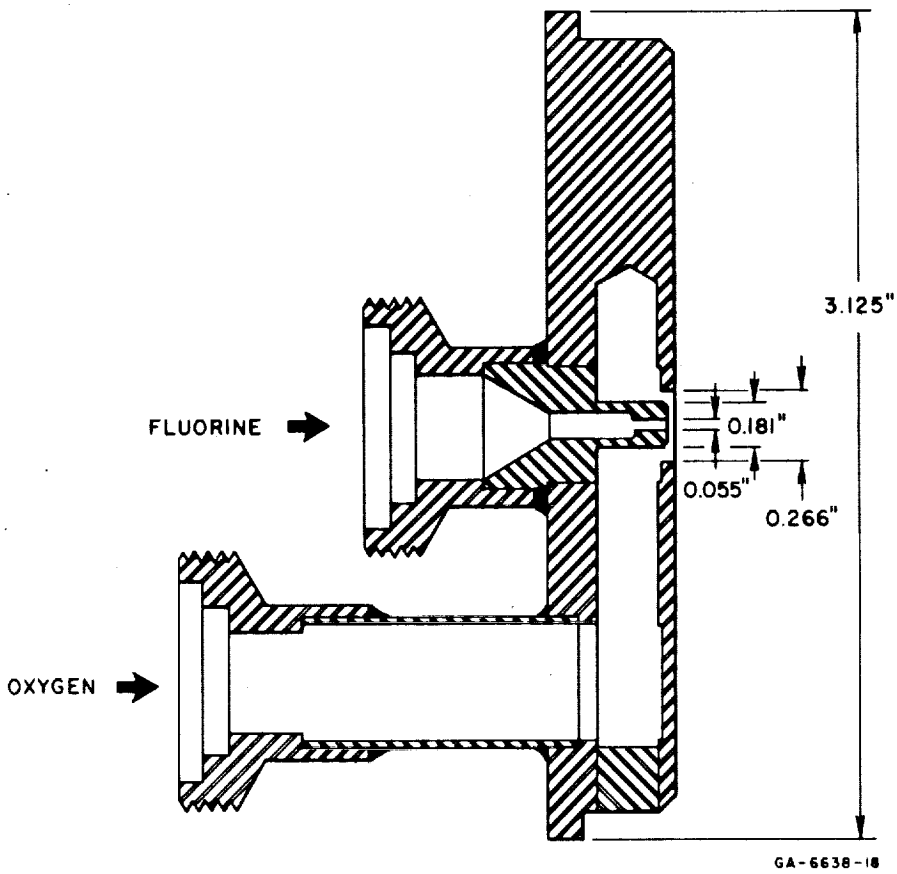

FIG. 24 INJECTOR USED WITH THE FLUORINE SYSTEM

computer code. It can be seen that the data at 50 psia and above agree reasonably well with the calculated regression rates, while the data in the vicinity of 20 psia tend to fall below the calculated values.

The 50 psia data point in the 100 percent PU system and the 20 psia data point in the 80 percent PU/20 percent Al system seem to be higher than the remaining points; unfortunately time was not available to repeat these runs but additional data will be obtained during future phases of the program. In general, the departure of the regression rate from the transport-limited value begins at a lower pressure with fluorine than with oxygen; a direct comparison is made in a later section.

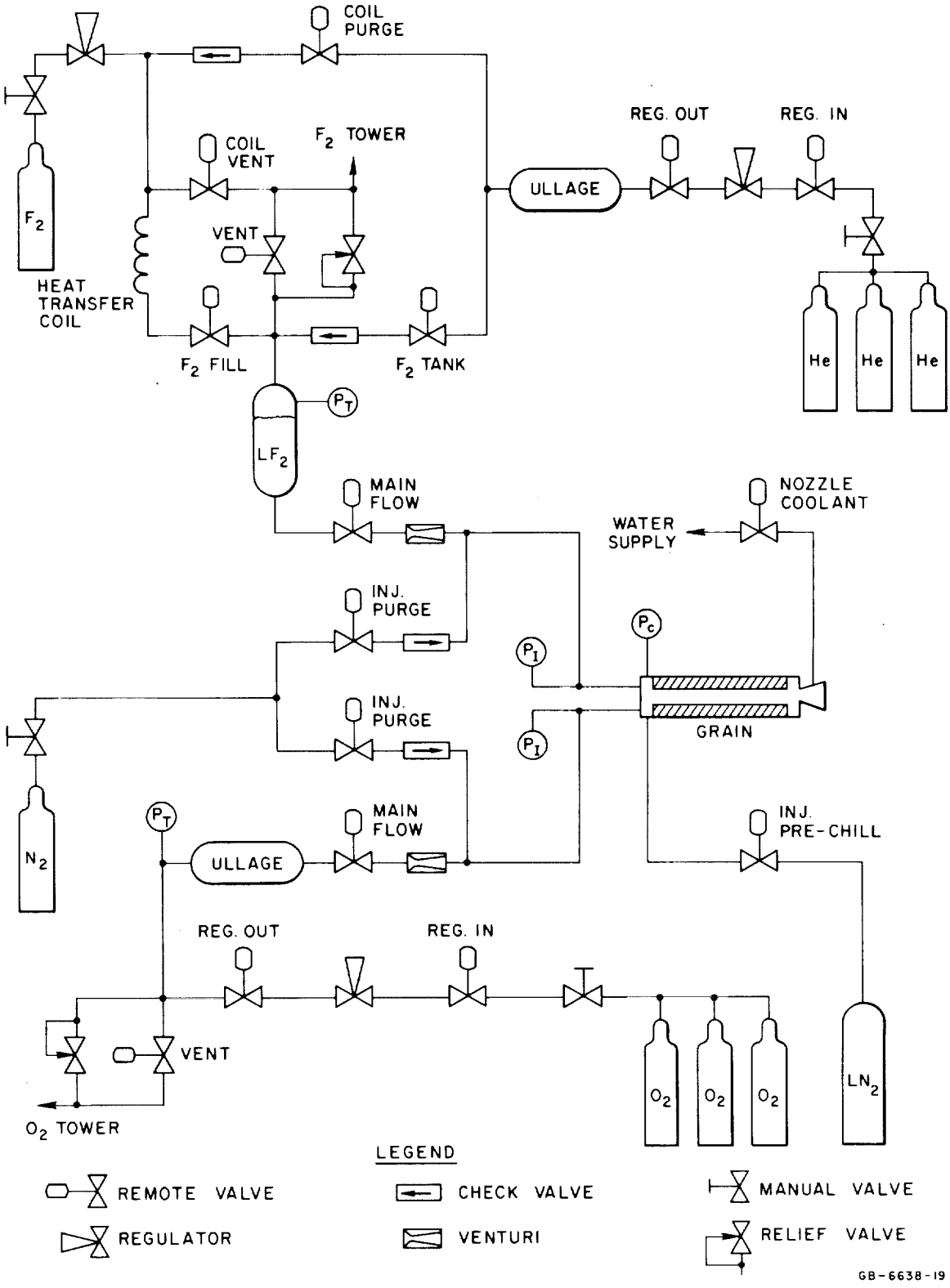

FIG. 25 SCHEMATIC OF FLUORINE FLOW SYSTEM

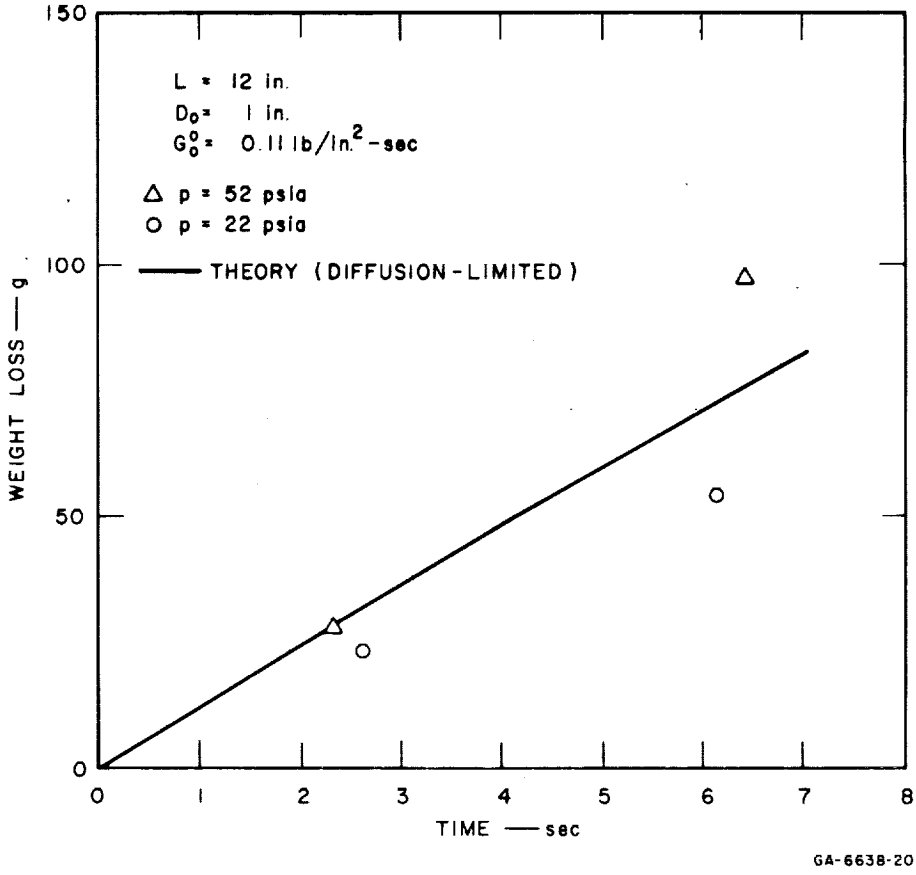

FIG. 26 WEIGHT LOSS OF A PURE PU HYBRID GRAIN BURNED WITH FLUORINE (D_o = 1 in.)

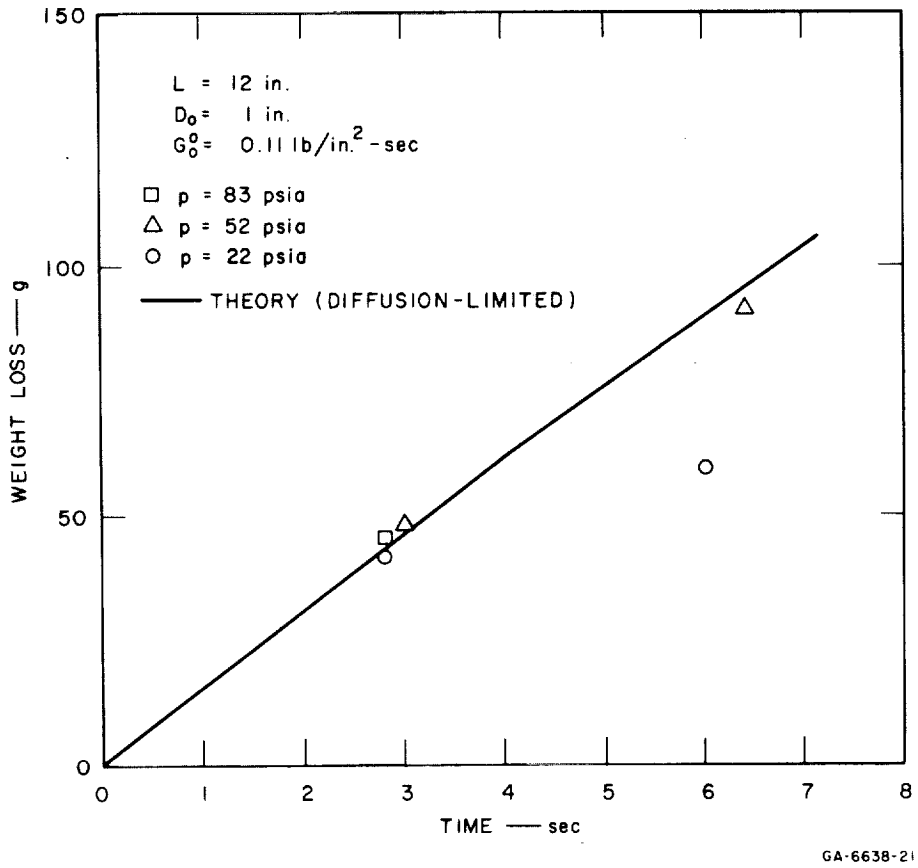

FIG. 27 WEIGHT LOSS OF AN 80 PERCENT PU/20 PERCENT ALUMINUM HYBRID GRAIN BURNED WITH FLUORINE (D_o = 1 in.)

E. Regression Rate Measurements with Nitrogen Tetroxide

The larger 5-in.-diameter motor configuration has been assembled and a limited amount of initial data has been accumulated with nitrogen tetroxide (N_2O_4) used as the oxidizing species with 100 percent PU grains. A photograph of the motor assembly is given as Fig. 28. Ignition is accomplished with the injection of hydrozene (N_2H_4) during the first second of operation. The vortex injector that was used is shown in detail in Fig. 29. N_2O_4 is injected in a vortical pattern through eight holes of 0.0595 in. in diameter; the swirling flow impinges on the wall of the injector and breaks up into a fine mist. Figure 30 is a photograph of a typical water spray pattern. It is essential to obtain good mechanical breakup of the spray pattern in a noncryogenic system such as this; the vortex injector

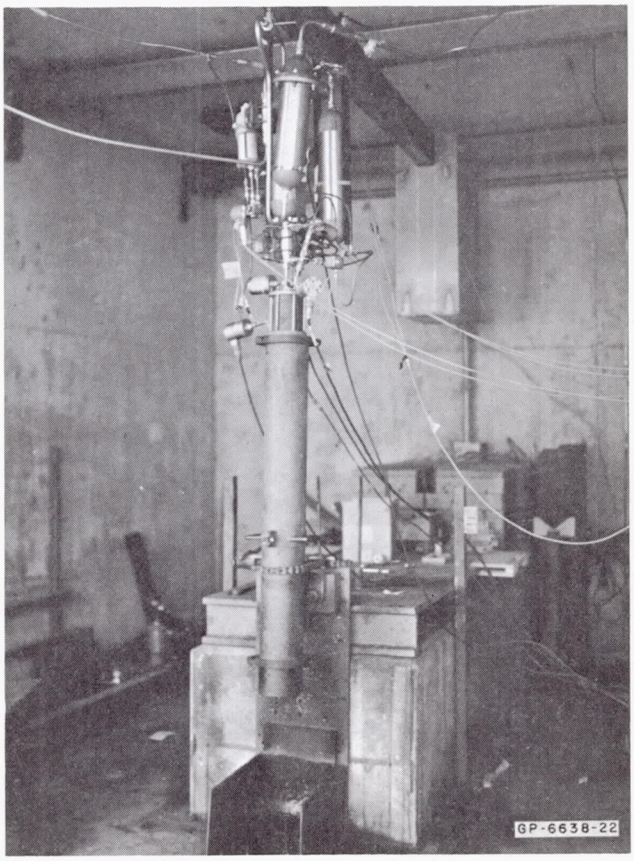

FIG. 28 N_2O_4 HYBRID SYSTEM ASSEMBLY

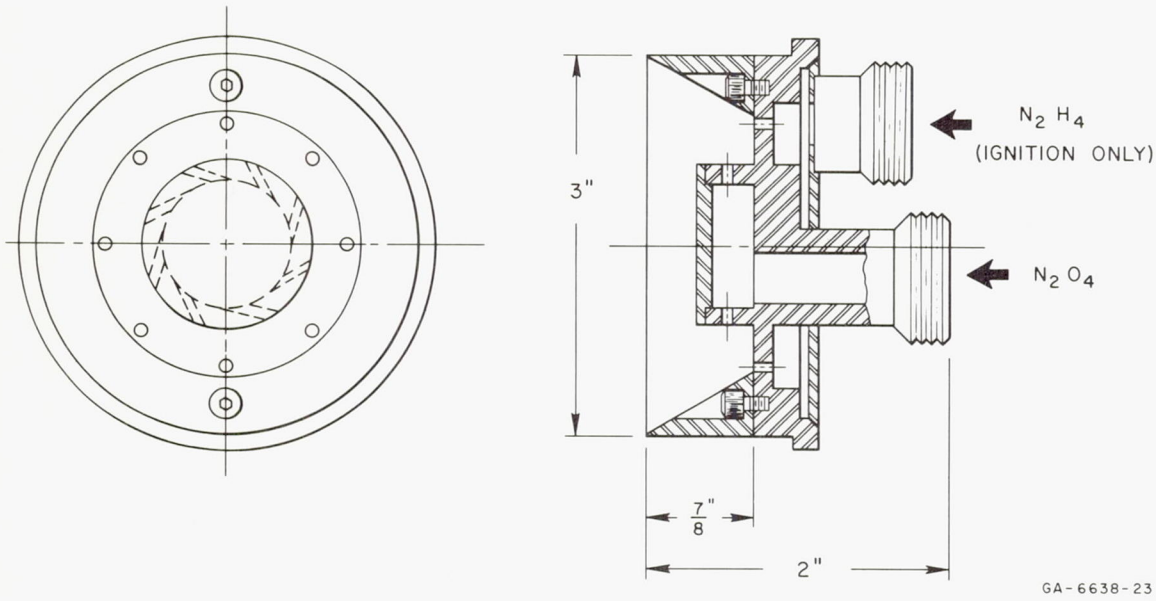

FIG. 29 INJECTOR USED WITH THE N_2O_4 HYBRID SYSTEM

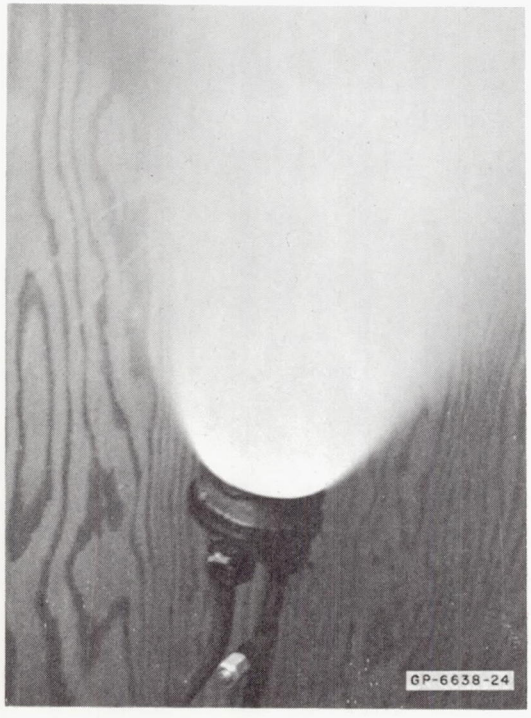

FIG. 30 WATER SPRAY PATTERN FROM N_2O_4 INJECTOR

works very well from this point of view. A schematic of the complete flow control system is presented as Fig. 31.

During the first year of the program the objective of the N_2O_4 studies was merely to design and check out the system. It will be very useful in the study of low-frequency instabilities associated with droplet vaporization lags. The larger size of the motor also makes it valuable for

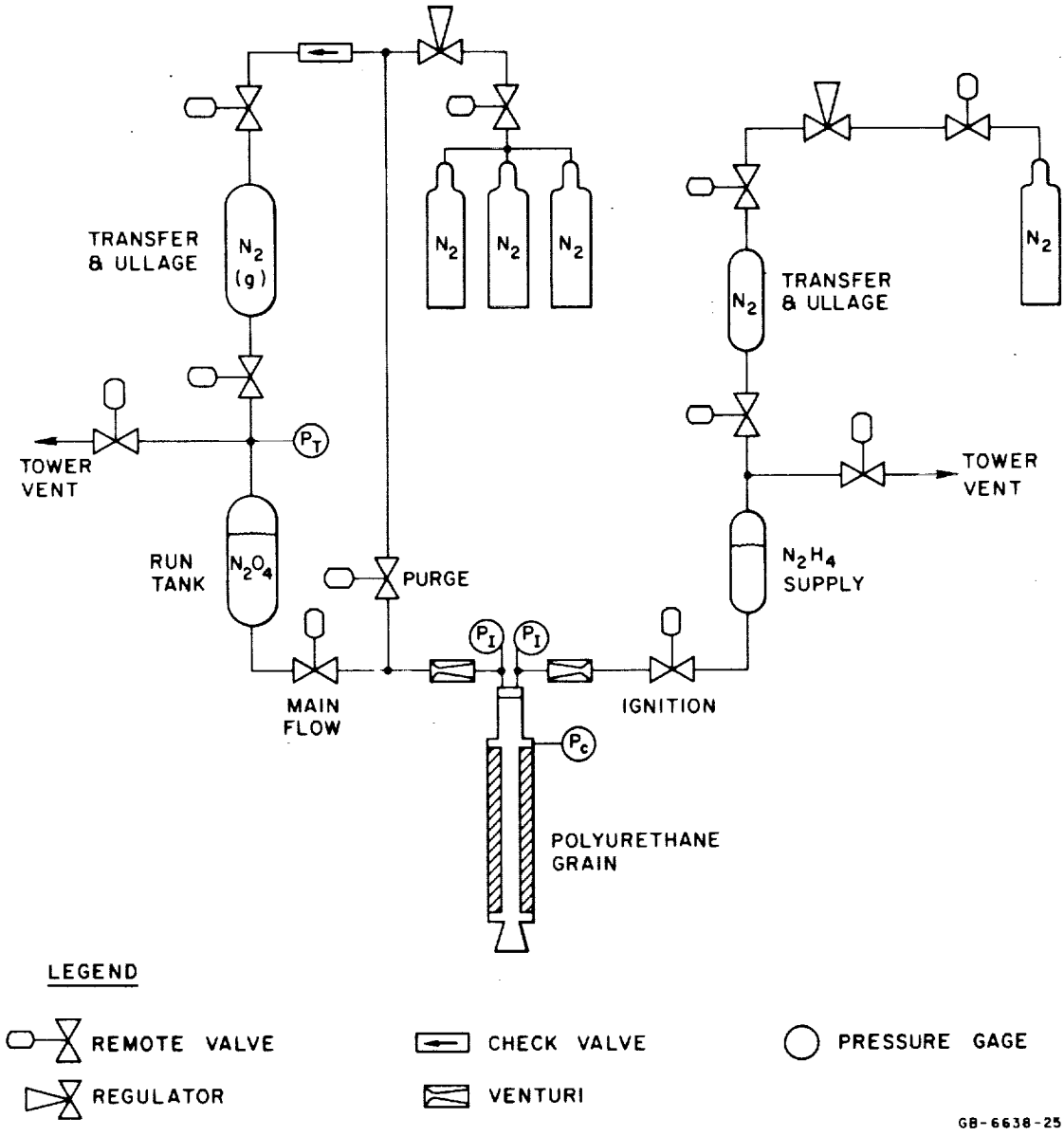

FIG. 31 SCHEMATIC OF N_2O_4 FLOW SYSTEM

scaling tests. Data obtained from two successive runs on one motor are shown in Figs. 32 and 33. The lower pressure was 100 psia (6.8 atm) at which the regression rate had fallen to about 0.8 of its asymptotic high-pressure value when oxygen was used as the oxidizer. In this case the decrease appears to be less than that, but more data are required to establish the actual dependence.

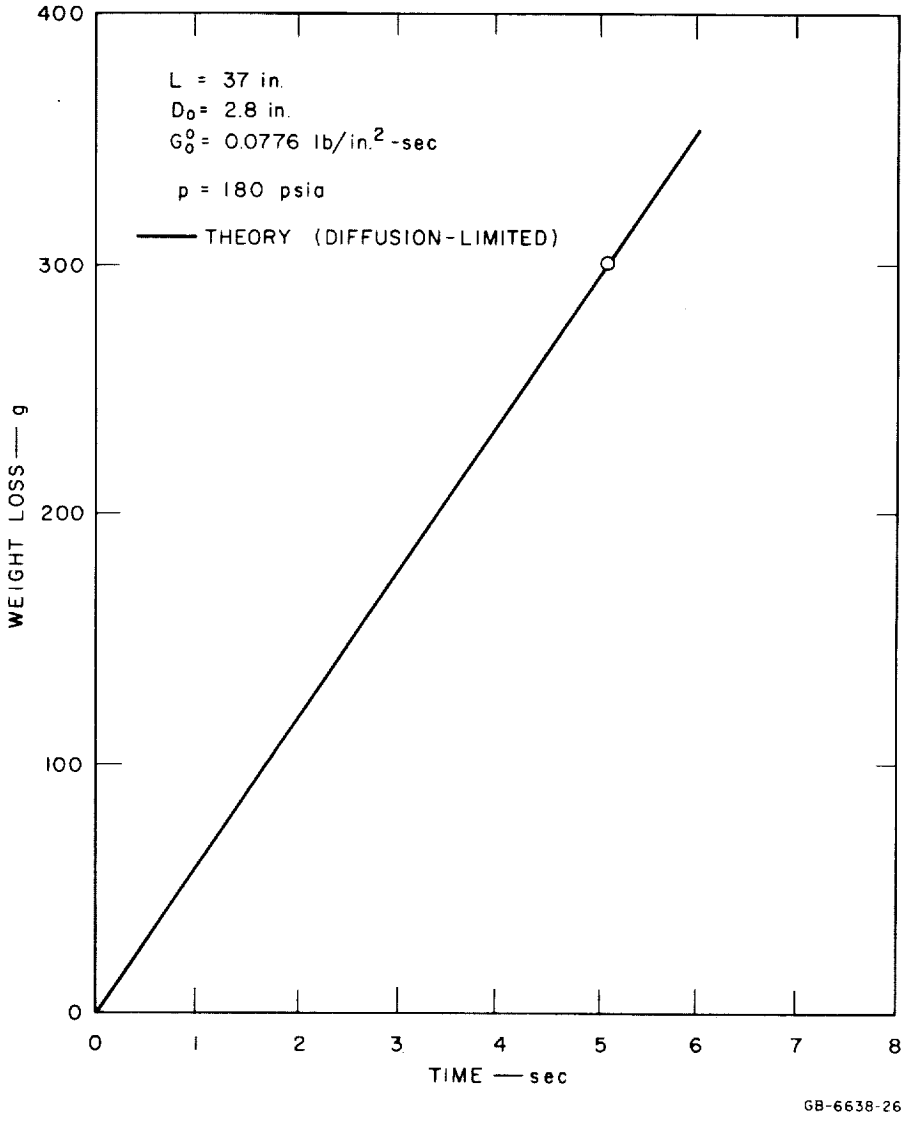

FIG. 32 WEIGHT LOSS OF A PURE PU GRAIN BURNED WITH N_2O_4 (D_o = 2.8 in.)

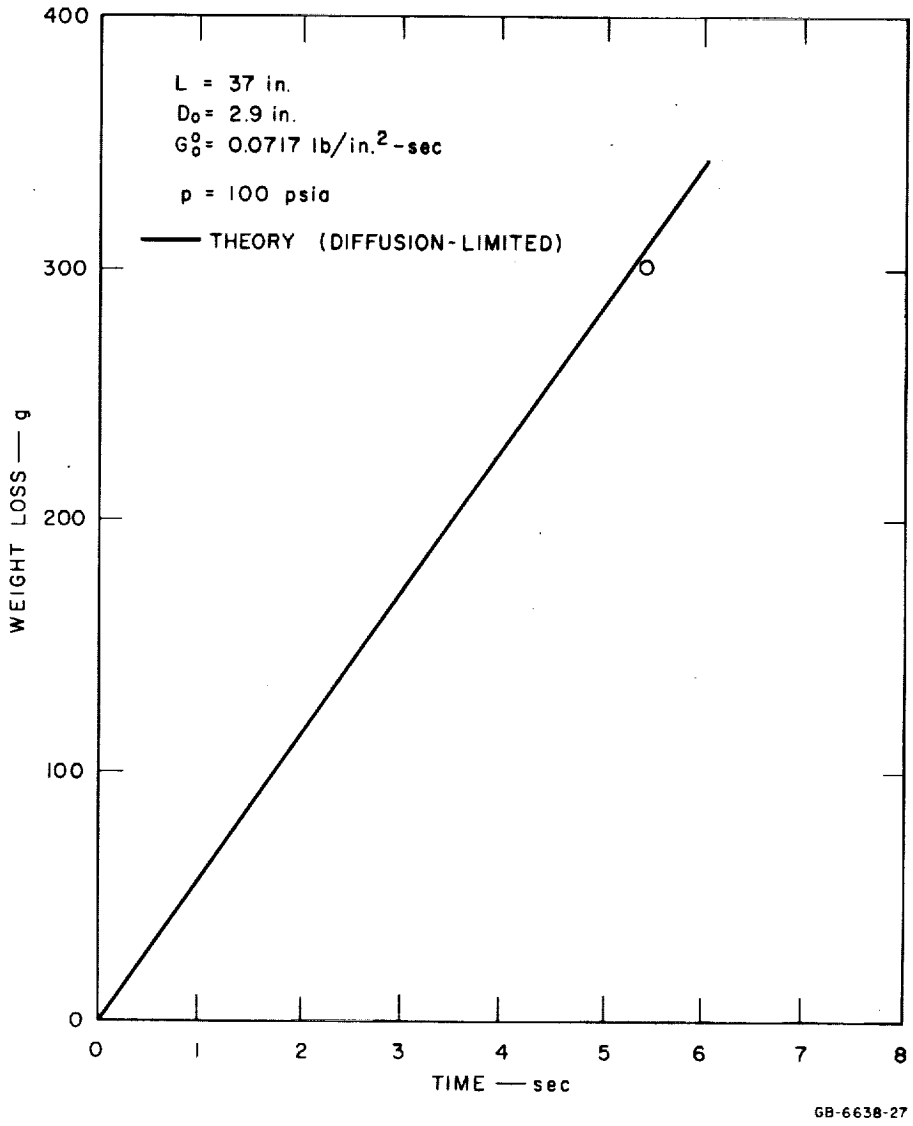

FIG. 33 WEIGHT LOSS OF A PURE PU GRAIN BURNED WITH N_2O_4 (D_o = 2.9 in.)

F. Experiments with an Orifice in the Grain

To gain additional information about the spontaneous instability described earlier, several PU grains were fired with graphite orifices cast in place one-quarter of the way down the grain from the head end. The initial internal diameter of the grain was 1.5 in. and the orifice diameter chosen was 0.75 in., giving a constriction ratio of 4. Figure 34 is a

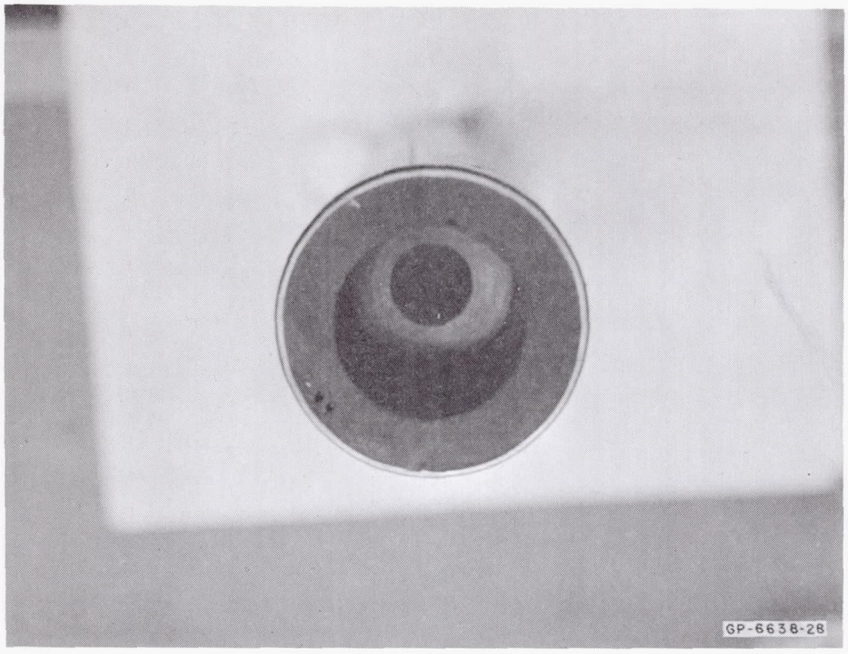

FIG. 34 AN ORIFICE INSTALLED IN A PU GRAIN

photograph of an orifice in place. Oxygen was used as the oxidizer in these tests.

Two results were of interest in these tests--the effect of the orifice on the weight loss (or regression rate) and its effect on the observed instability wave. Weight loss data are shown in Fig. 35. It can be seen that the overall effect of the orifice is to increase the burning rate by at least 50 percent. The burning rate/pressure dependence, however, is similar to that observed in the system without the orifice, indicating that the effect of the orifice is one of gross turbulent mixing and is not a direct influence on the chemical kinetics.

The spontaneous appearance of an instability wave, similar to that illustrated in Figs. 25 and 26, was observed even with the orifice in place. The results are shown in Fig. 36. The frequency of the wave is approximately 510 cps, compared to the 650 cps recorded earlier without the orifice. The amplitude of the wave is somewhat larger at the lowest

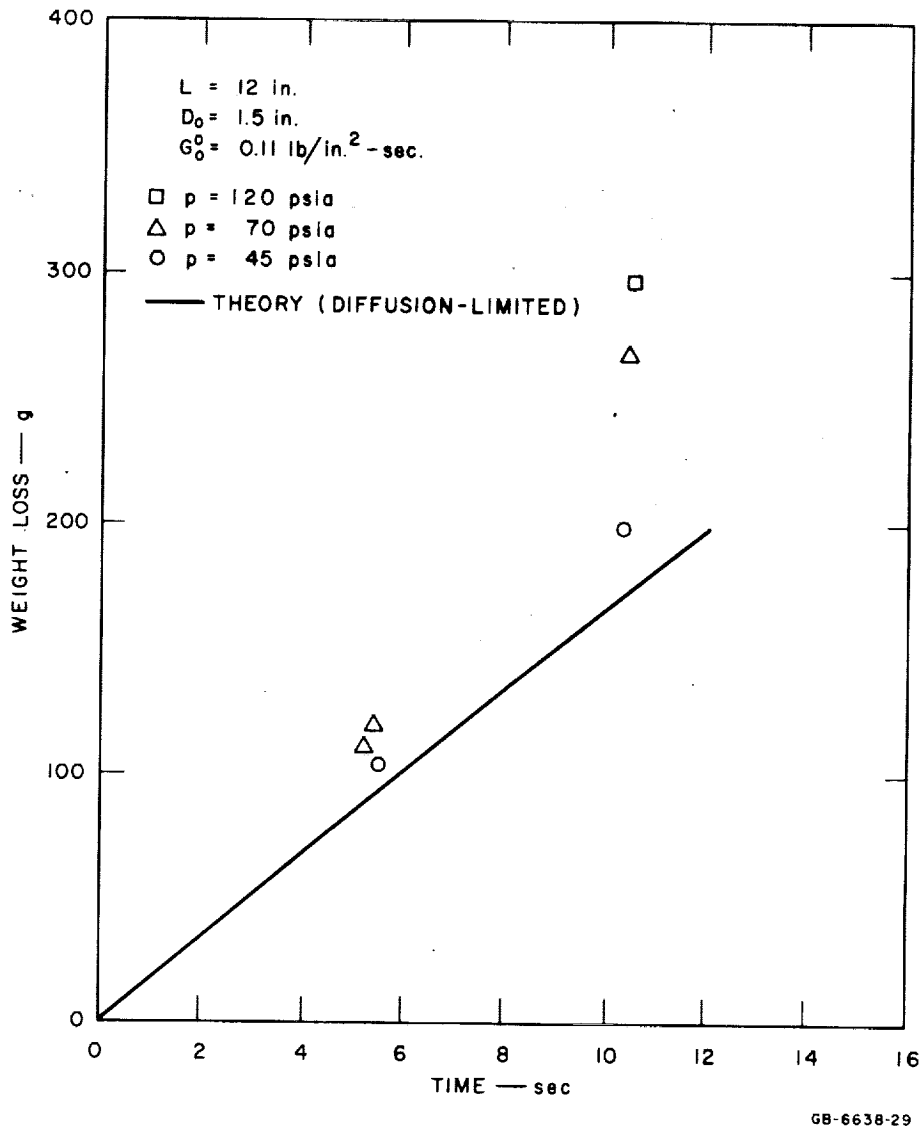

FIG. 35 WEIGHT LOSS OF A PURE PU GRAIN CONTAINING AN ORIFICE AND BURNED WITH OXYGEN (D_o = 1.5 in.)

mean pressure, but is smaller at the highest pressure, compared to the results obtained without an orifice. Other investigators[3] have used orifices to suppress the low-frequency instability associated with droplet vaporization lags; it is apparent that this device has little effect on the present acoustic mode of instability. Further investigation will be carried out as the program continues.

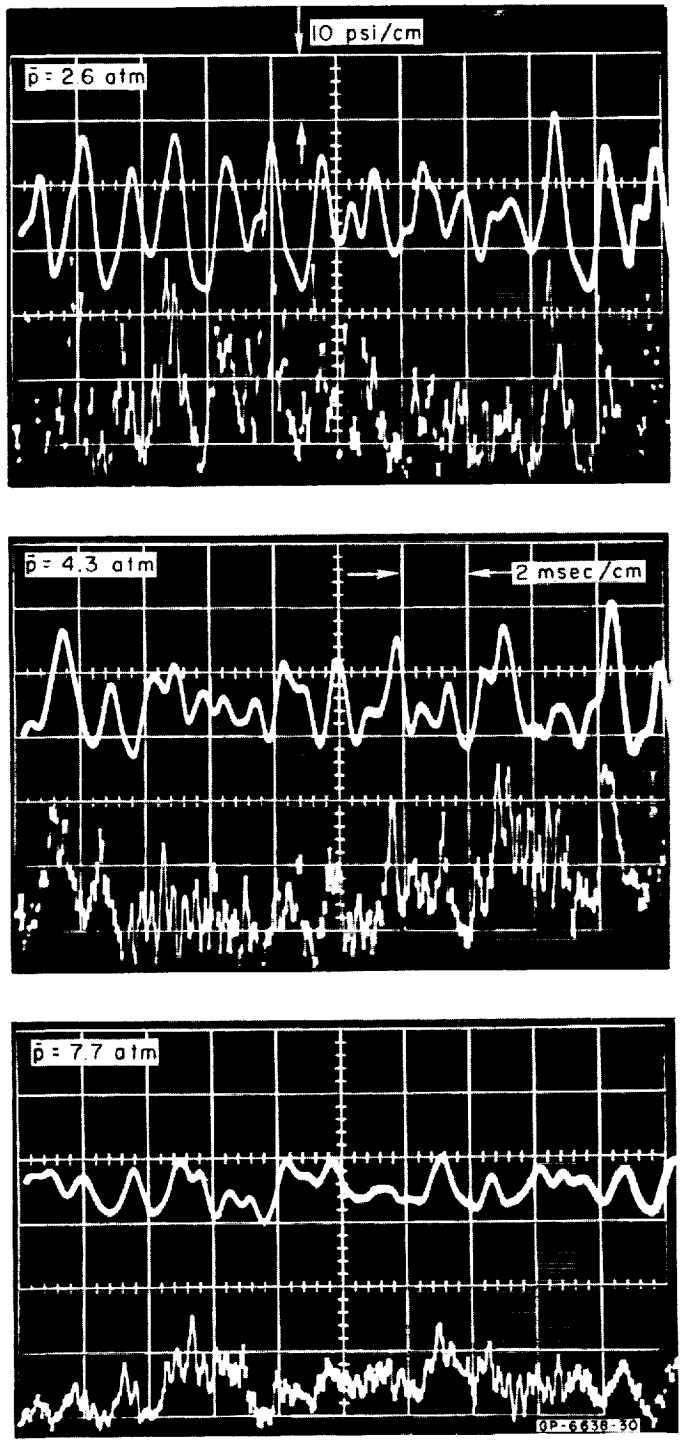

FIG. 36 SPONTANEOUS INSTABILITY OBSERVED WITH AN ORIFICE IN THE GRAIN (Pure PU)

G. Slab Burner Experiments

A small-scale slab burner, depicted in Fig. 37, has been constructed and used to obtain initial schlieren photographs of the hybrid combustion process as an aid to the parallel theoretical effort. The inlet to the burner contains a flow-straightening section to assure smooth flow conditions in the test section. Glass windows are provided in the 2 in. by 2 in. test section. Two schlieren photographs of the combustion zone over a Plexiglas slab obtained at two pressure levels are included as Fig. 38. The flow is from right to left, and the schlieren light has been blocked off at the left edge of the picture to show the luminosity of the flame zone. For these tests the Reynolds number was approximately 1.5×10^5/in. Note that the position of the flame zone, as determined from both the luminosity and the change in the density derivative observed on the schlieren picture, is approximately 10 to 15 percent of the total boundary layer thickness away from the wall. This result agrees with previous measurements obtained

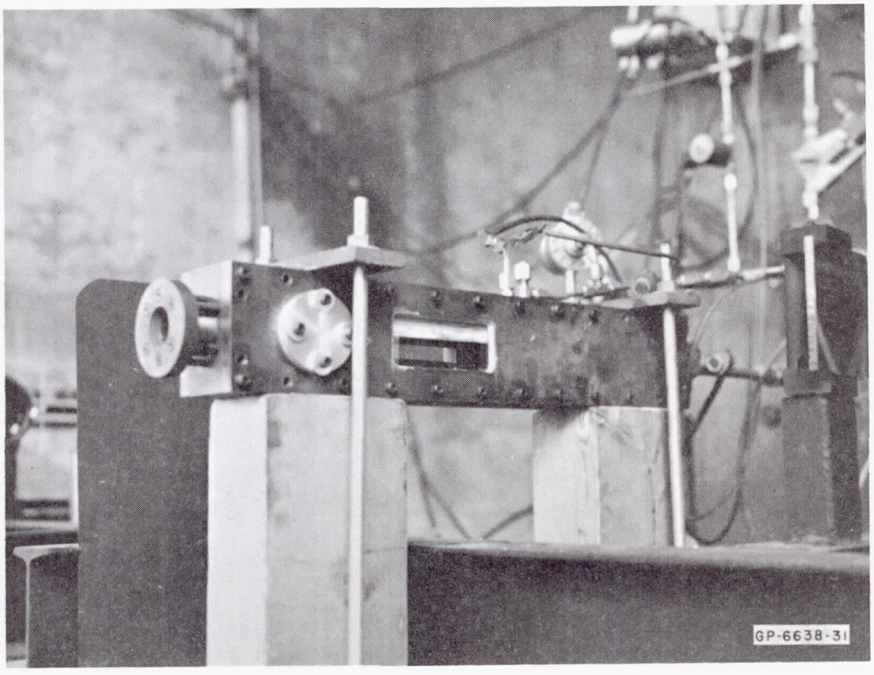

FIG. 37 SMALL-SCALE SLAB BURNER

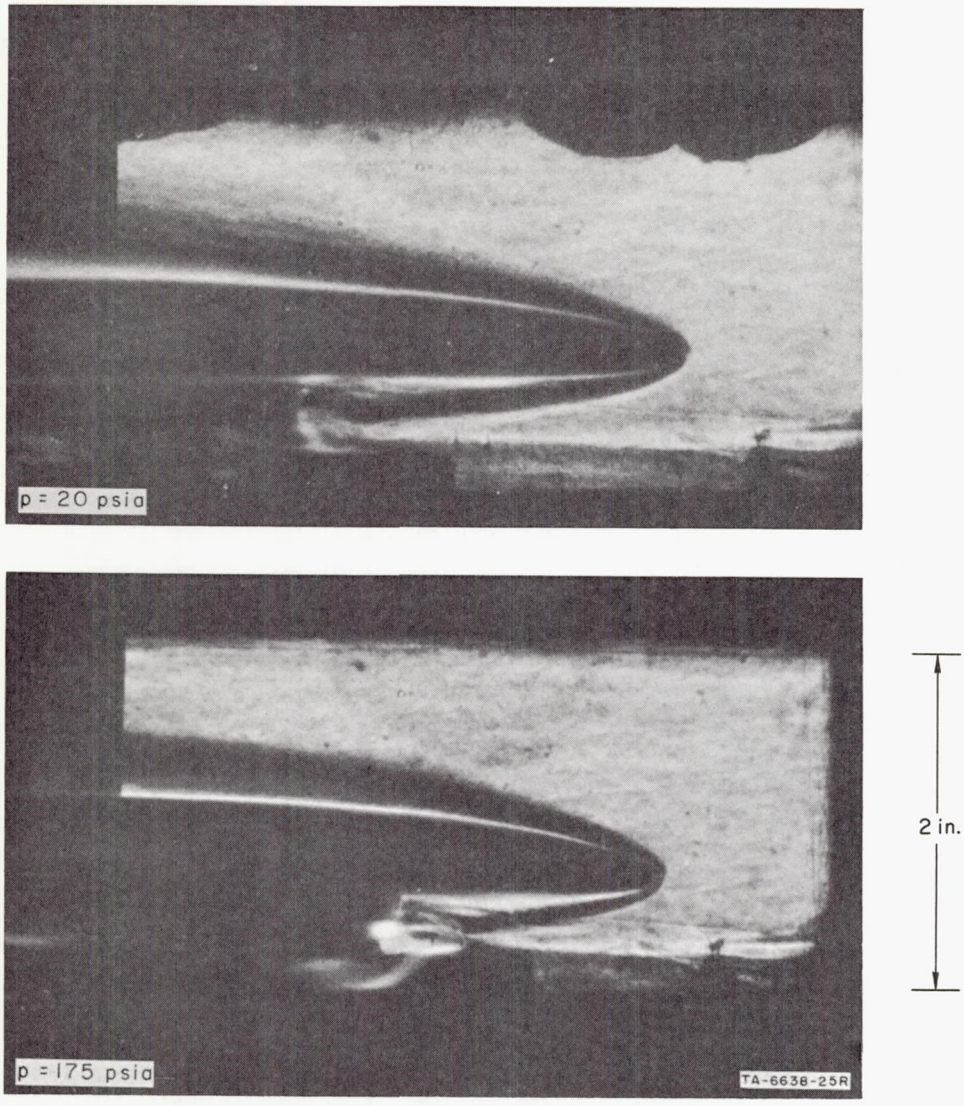

FIG. 38 SCHLIEREN PHOTOGRAPHS OF A BURNING PLEXIGLAS SLAB

at atmospheric pressure.[1] Note also that the flame zone is much thicker at low pressure where kinetics play an important role. The two pictures shown here were obtained at an oxidizer mass flux of 0.1 lb/in.^{2}-sec. Future studies will consider other propellants, other oxidizer mass fluxes, and additional levels of pressure. The observed position and thickness of the flame zone will be used to aid in the theoretical interpretation of combustion in the low-pressure regime.

H. Experiments in the Combustion Simulator

An ultimate goal of this program is to develop a theoretical description of the hybrid combustion instability mechanism, so that unstable burning can be predicted to a reasonable degree. It is quite certain that this mechanism involves a complicated interaction between the turbulence structure of the boundary layer and the reaction process. Therefore, to develop a realistic model it will be necessary to obtain some experimental data that help to reveal the real nature of the coupling mechanism. Past experience has shown that it is virtually impossible to obtain such data in slab burners or laboratory motors. For reliable measurements a technique is required that accurately simulates hybrid combustion but provides controlled burning conditions and a fixed solid/gas interface for spatial reference. To fill this requirement, a wind tunnel having a test section 7 in. by 7 in. in cross-section which contains a 6-in.-wide by 30-in.-long porous section in the upper wall has been built with Institute funds. The design incorporates honeycomb and screens in the settling chamber, followed by a 10:1 contraction ratio, to ensure smooth flow conditions in the free-stream of the test section. The similator, shown in Fig. 39, operates near atmospheric pressure. The size of the tunnel was dictated by the desire to obtain a thick enough boundary layer over the porous section to allow accurate probing of the layer. A mixture of hydrogen and nitrogen is injected as the fuel through the porous section for the combustion experiments. This fuel is used because of the wide flammability limits of the hydrogen-air flame which make it possible to vary the maximum temperature in the boundary layer over wide limits. The significance of this point will be discussed later. The boundary layer thickness which is obtained is approximately two inches, depending on the rate of wall mass injection. The test section has a moveable lower wall so that a wide range of axial pressure gradients can be imposed. The value of the simulator is that it allows detailed diagnostic measurements to be carried out

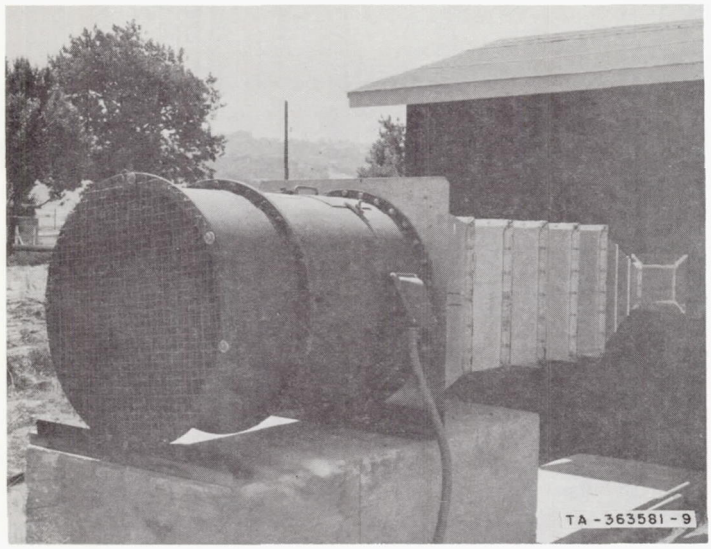

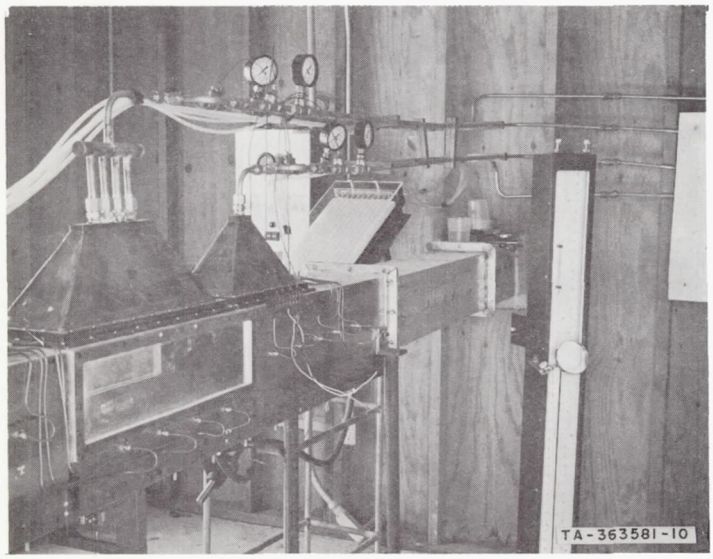

FIG. 39 HYBRID COMBUSTION SIMULATOR

in a relatively thick, burning, turbulent boundary layer over a stationary (i.e., nonregressive) surface.

The theoretical analysis presented earlier requires as an input an estimate of the rms turbulence level in the presence of the flame zone. The functional dependence of the turbulence level on such parameters as mass flux, Reynolds number, and mass transfer number is of primary

importance in attaining a general understanding of the process. Current results, which are discussed in detail in the next section of this report, indicate that good agreement is obtained between the theoretical and experimental regression rate/pressure dependence, but that the mass flux dependence is less satisfactory.

Earlier turbulence measurements in a similar apparatus[20] showed a marked interaction between the flame zone and the turbulent structure, even though those measurements were restricted by the apparatus to a thin region near the wall. The indication to be gained is that further experiments closer to the flame zone with more sophisticated instrumentation will be required before any real understanding of the interaction is attained. For this reason, a constant-temperature hot wire anemometer, capable of being used with cooled probes, is being purchased for use during the second year of the program.

Because hot wire measurements are required to define the fluctuation parameters of interest, only a limited number of experiments, consisting of temperature profile measurements, were carried out in the simulator during the first year's effort. Temperature profiles obtained in a zero-pressure gradient flow at two values of the mass transfer number B are shown in Fig. 40.

Of particular interest is the observed change in the profile at a fixed value of B as the maximum temperature is reduced. This reduction is achieved by changing the proportion of hydrogen in the hydrogen-nitrogen fuel mixture injected through the porous plate. For the present experiments at B = 7.2 the reduction in maximum temperature from 950°C to 730°C was achieved by reducing the mass fraction of hydrogen in the incoming mixture from 4 to 3.5 percent. As the temperature is lowered the flame zone broadens considerably. From the point of view of the effect on turbulence structure in the boundary layer, such behavior simulates the

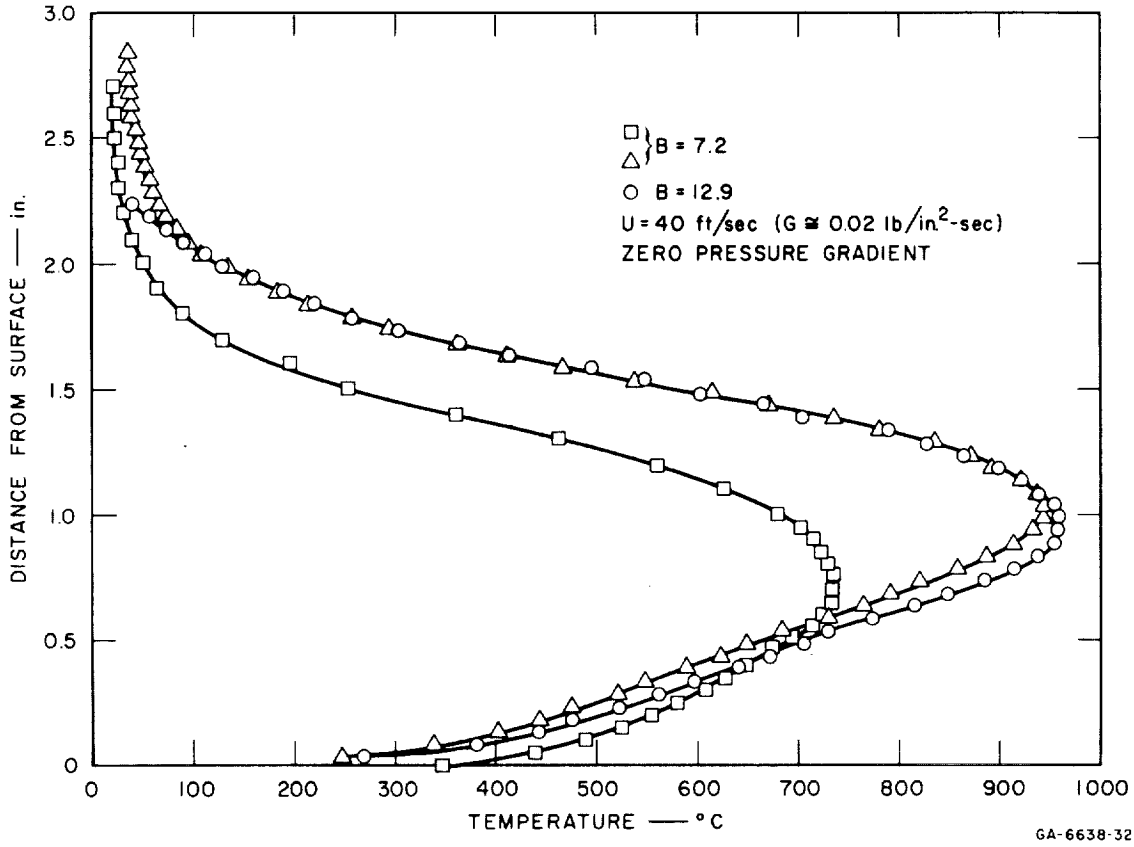

FIG. 40 TEMPERATURE PROFILES IN A BURNING TURBULENT BOUNDARY LAYER

observed effects in the pressure-sensitive regime wherein the flame zone thickness grows as chemical kinetic processes begin to exert an influence. Turbulence measurements under the two conditions shown would help to establish the dependence of the characteristic mixing time on the flame zone thickness and heat release distribution.

Also shown in Fig. 40 is a profile obtained at B = 12.9. Note that this profile nearly matches the high-temperature profile for B = 7.2. Turbulence measurements with the higher rate of wall mass injection would also be valuable as an aid to the theoretical analysis of turbulent mixing and combustion. Such experiments are planned for the second phase of the program.

V. EXPERIMENTAL RESULTS AND COMPARISON WITH THEORY

A complete synopsis of the experimental mean regression rate data is presented in Figs. 41 and 42 for the PU-oxygen and PBAN-oxygen propellant systems respectively. The results are presented as the mean regression rate over 5 sec of operation versus the mean pressure in logarithmic coordinates. The tests encompass three types: (1) constant oxidizer flow rate, constant nozzle area; (2) constant oxidizer flow rate, variable nozzle area; and (3) variable oxidizer flow rate, constant nozzle area. For the variable tests, the mean regression rate is plotted versus the mean pressure.

First, it is observed from Figs. 41 and 42 that the presence of metal loading does not materially affect the observed pressure sensitivity when the results are presented in terms of the ratio $\bar{\dot{r}}/\bar{\dot{r}}_{\infty}$. (It should be noted that $\bar{\dot{r}}_{\infty}$ for the 40 percent aluminum-loaded systems is approximately twice that for the systems with no aluminum.) Also, within the scatter of the data, which seems to increase somewhat as the pressure is lowered, the variable mass flux and nozzle area tests (which both induced pressure variations) gave results that are consistent with each other and with the results from tests with constant conditions.

Also shown in the figures are theoretical curves for the 100 percent binder and the 60 percent binder/40 percent aluminum fuel systems. These curves have been generated by assuming that $t_1/T = 1$ at 9 atm, $n = 2$, and $E_f = 60$ kcal/mole. The slight difference in the two curves at low pressure stems from the slightly different behavior of flame temperature with pressure for the two systems (see Appendix G). For comparison, the least-square-error line through the data points is also shown.

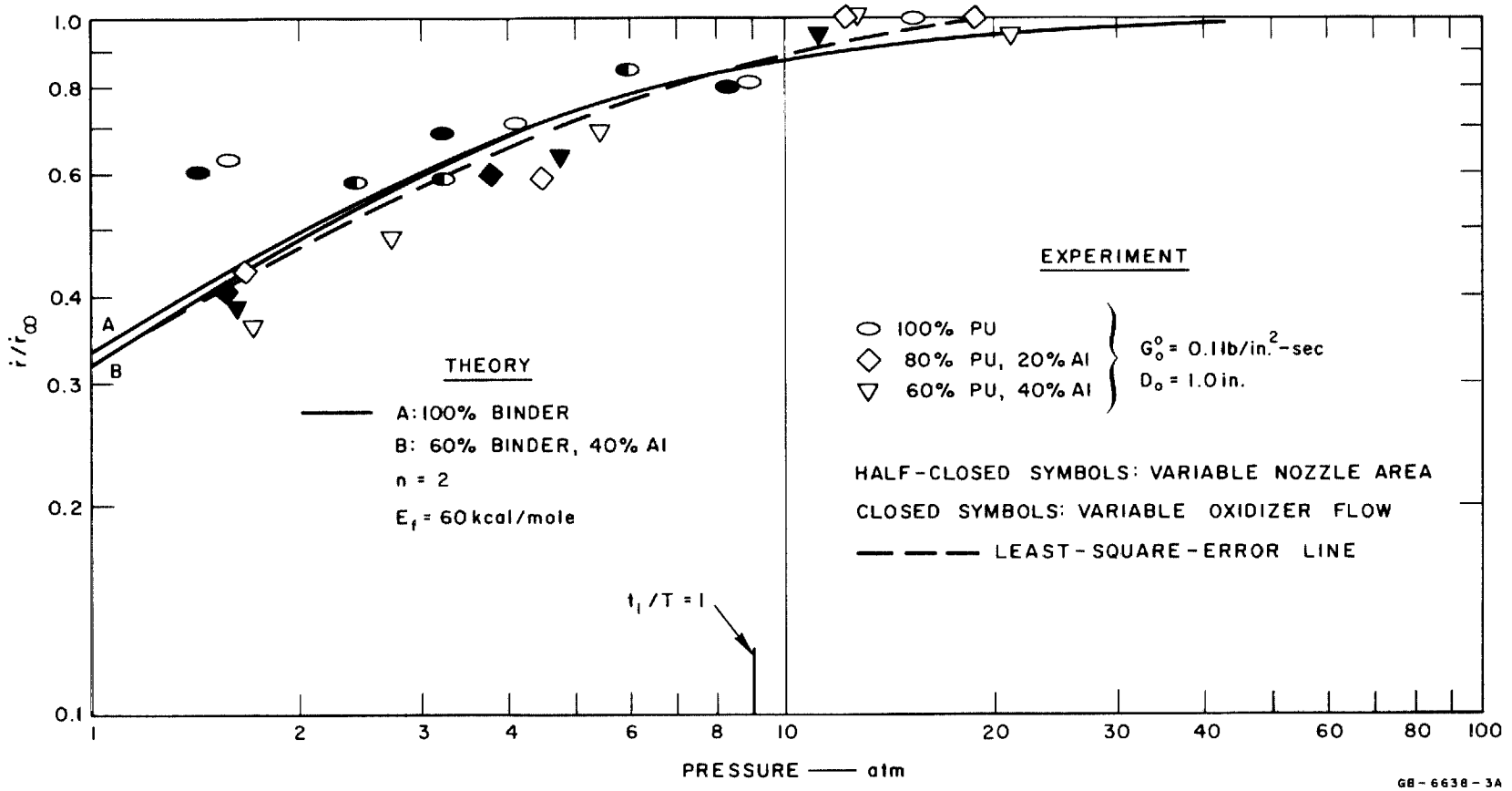

FIG. 41 REGRESSION RATE BEHAVIOR OF PU-OXYGEN PROPELLANT SYSTEM

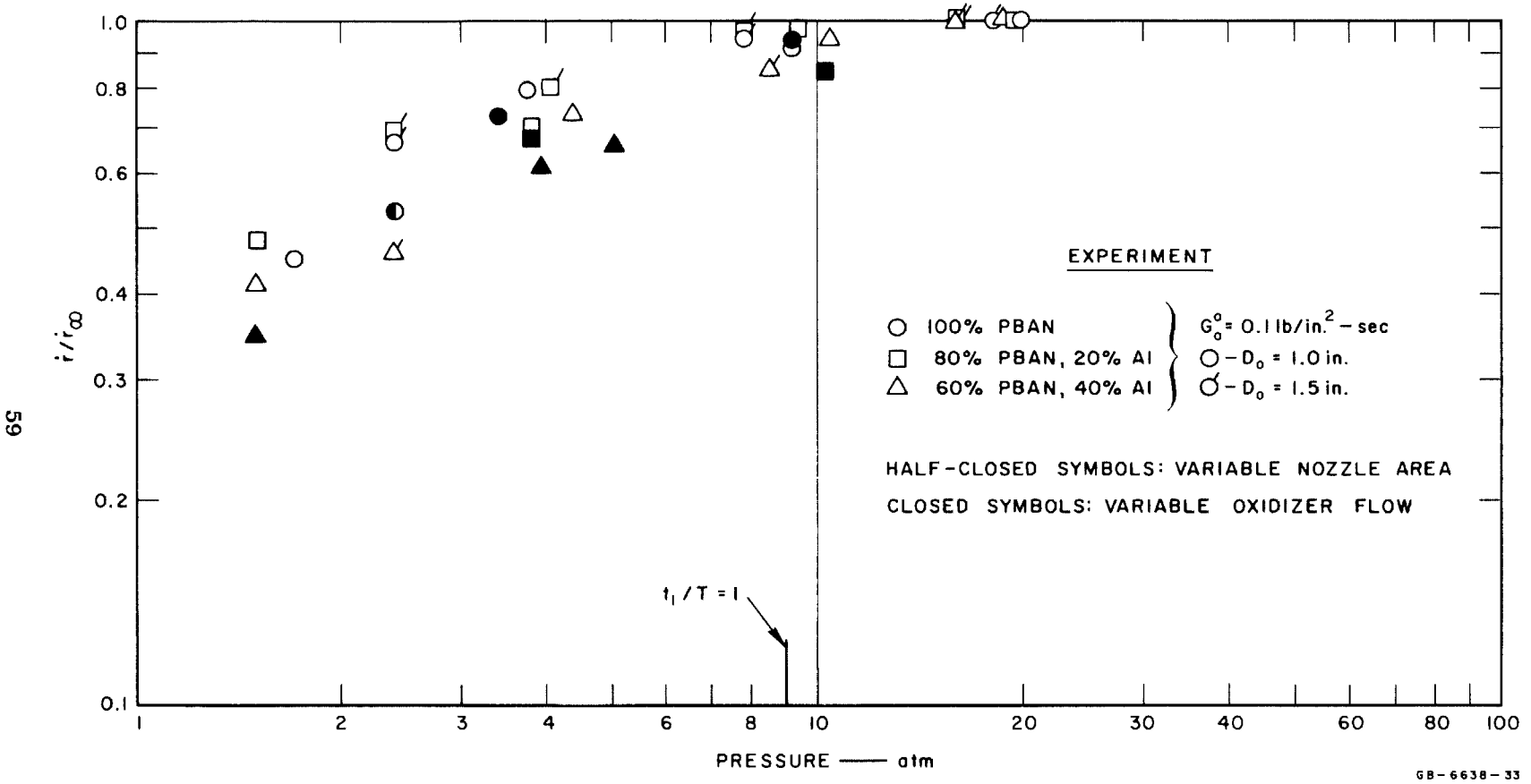

FIG. 42 REGRESSION RATE BEHAVIOR OF PBAN-OXYGEN PROPELLANT SYSTEM

As shown in Section III, the exact choice of gas-phase activation energy is not critical to the calculated value of regression rate ratio, whereas the choice of gas-phase order n has a sizeable effect. The present choice of n = 2 gives very good agreement between the theory and the least-square-error curve through the data. This value of n implies that the preponderance of heat release takes place in bimolecular reactions, as would be expected in a hydrogen/carbon/oxygen gas-phase flame.

The data shown in Figs. 41 and 42 were obtained at an oxidizer mass flux of 0.1 lb/in.^{2}-sec. The data of Smoot and Price[9,10] show a similar dependence of regression rate on pressure at this mass flux and indicate further that the length ratio ℓ_1/ℓ_2 in Eq. 5 is a function of mass flux.

This behavior is demonstrated by the data shown in Fig. 43. At high values of oxidizer mass flux and a fixed pressure, the analysis predicts a regression rate proportional to $G^{0.4}$ while the experimental regression rate becomes independent of the mass flux. It is not surprising that the unknown length ratio is some function of the mass flux because the transport of oxidizer through the boundary layer is a function of G. Further experiments at different values of mass flux must be carried out to settle this point. It is certainly true, however, that the theoretical prediction at a fixed mass flux agrees remarkably well with the data.

The results from the test firings with fluorine are shown in Fig. 44. In this case the critical pressure, at which the parameter θ is unity, is considerably lower than in the oxygen case, being about 2.25 atm instead of 9 atm (the theoretical curve for the oxygen system is shown for comparison). This behavior reflects the greater reactivity of fluorine compared to oxygen, thereby lowering the pressure threshold at which chemical kinetic processes begin to exert an influence. This implies that fluorine systems are less likely to exhibit acoustic instability; this point will be investigated as the program proceeds.

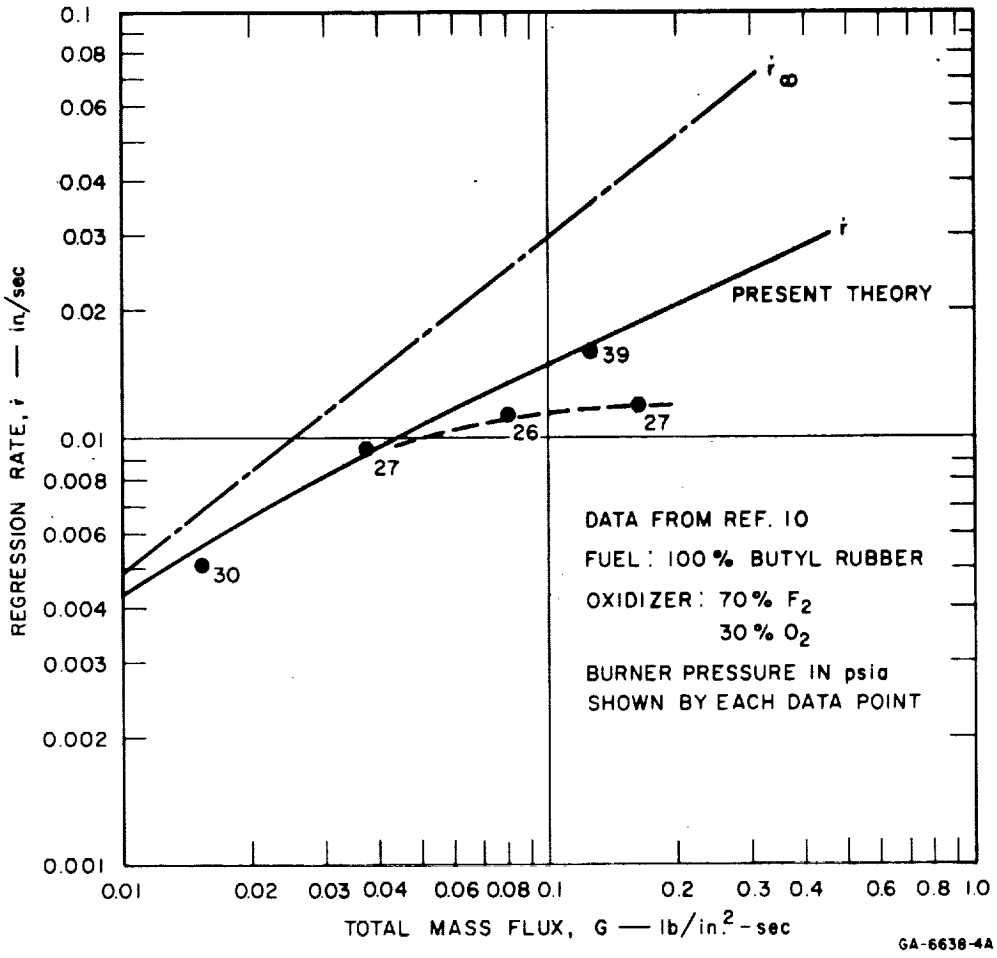

FIG. 43 EFFECT OF MASS FLUX ON REGRESSION RATE

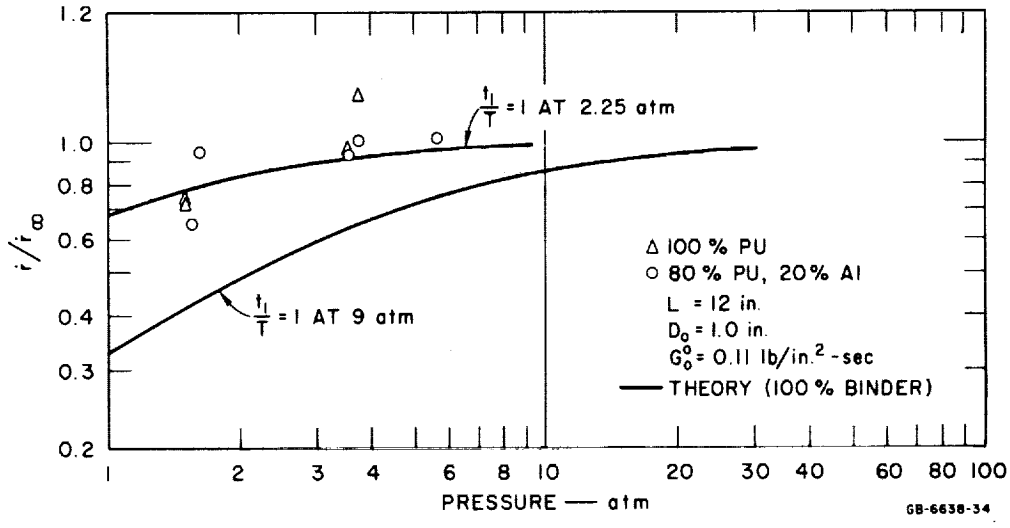

FIG. 44 REGRESSION RATE BEHAVIOR OF PU-FLUORINE PROPELLANT SYSTEM

VI. CONCLUSIONS AND RECOMMENDATIONS

During the past year a major effort has been made to characterize the behavior, both experimentally and theoretically, of typical hybrid propellant systems in the regime where the regression rate is pressure-dependent. The occurrence of a pressure dependence leads to the strong possibility of an acoustic instability, arising through the response of the regression rate to pressure perturbations. To obtain a mathematical model of the response function, it is first necessary to understand the steady-state pressure-sensitive behavior of hybrid propellants.

Two binders were chosen for the experimental investigation--cleanly gasifying PU and charring PBAN to determine whether different surface kinetics play a first-order role in the combustion process. Aluminum loadings of 0, 20, and 40 percent were employed with both binder systems to ascertain the role of radiation in the pressure-sensitive regime. Oxygen, fluorine, and nitrogen tetroxide were used as oxidizers to help establish the role of oxidizer reactivity in the combustion process.

The main results of the first year's effort can be summarized as follows:

1. The regression rate/pressure dependence observed at low pressures is independent of binder pyrolysis characteristics and aluminum loading for a given oxidizer.

2. A noticeable decrease is observed in the regression rates of PU and PBAN fuels below 10 atm when oxygen is used as the oxidizer and below 2.5 atm when fluorine is used. These values pertain to an oxidizer mass flux of 0.1 lb/in.^{2}-sec and would decrease with increasing mass flux. The lower threshold pressure for fluorine is a consequence of its generally greater reactivity.

3. A relatively simple analytical model based on the wrinkled-flame-sheet turbulent flame theory has been developed. The model agrees well with the data obtained at a fixed oxidizer mass flux. Modifications are needed to improve the description of variable mass flux conditions.

4. A spontaneous longitudinal instability was observed to develop under certain conditions of diameter and mass flux. The presence of this wave is related to the ability of the regression rate to respond to a pressure perturbation of the given frequency. The wave was virtually unaffected by the addition of an orifice in the grain.

5. Experiments with a pulsed oxidizer flow showed a greater variation in the chamber pressure than could be calculated by assuming a quasi-steady regression rate. This result indicates a propellant response of the kind that arises in unstable combustion. The pulsed flow also acted to damp the higher frequency spontaneous oscillation.

6. Schlieren photographs obtained from the slab burner showed that the combustion zone in the turbulent boundary layer is much thicker at lower pressure where chemical kinetics exert a significant influence than at high pressure.

During the second phase of the study, additional regression rate data will be obtained at other values of the oxidizer mass flux to provide scaling information for further theoretical development. Longitudinal disturbances will be deliberately introduced into the chamber by firing an external powder pulse to enable a study of their growth and decay under different environmental conditions and to shed light upon previously observed spontaneous waves.

A perturbation analysis will be carried out on the steady-state model to obtain an expression for the acoustic admittance of the burning turbulent boundary. These theoretical studies will also be supported by additional experiments in the slab burner and the wind tunnel combustion simulator.

Appendix A

DIFFUSION-LIMITED THEORY OF STEADY-STATE HYBRID COMBUSTION

In the steady state, all of the heat transferred to the solid is used in vaporizing the solid material. Under these conditions the heat transferred to the surface is balanced by the mass flow rate of fuel times the total heat of gasification:

$$\dot{Q}_w = \dot{m}_f h_v = \rho_f \dot{r} h_v \tag{A-1}$$

The heat of gasification h_v is composed of the latent heat of vaporization plus the heat required to raise the temperature of the solid from ambient conditions deep in the grain up to the surface temperature.

The total heat transfer is generally composed of convective and radiative parts. The convective heat transfer can be directly characterized by the semiempirical theories which are available, whereas a description of the radiative transfer relies currently upon an empirical radiation coefficient, as will be discussed below.

Convective Heat Transfer

The convective heat transfer at the surface is governed by the conduction equation:

$$\dot{Q}_w = -\left(\frac{k}{c_p}\frac{\partial h}{\partial y}\right)_w = C_H \rho_b u_b \Delta h \tag{A-2}$$

where the subscript b refers to conditions at the flame. This equation serves to define a Stanton number C_H which is based upon the sensible enthalpy difference between the flame and the wall $[\Delta h = (c_p T)_b - (c_p T)_w]$.

Equations A-1 and A-2 can be combined to give an equation for the regression rate:

$$\rho_f \dot{r} = C_H \rho_b u_b \frac{\Delta h}{h_v} \tag{A-3}$$

It is convenient to evaluate the Stanton number in terms of the skin friction coefficient for which experimental data and well-documented empirical expressions are available. For a nonunity Prandtl number but a unity Lewis number, the heat transfer in the boundary layer is related to the shear stress by

$$- \frac{\dot{Q}}{\partial h/\partial y} = \frac{\tau}{\partial u/\partial y} \, Pr^{-0.67} \tag{A-4}$$

Since $\dot{Q}/\dot{Q}_w = \tau/\tau_w$ from Eq. 4, for a constant Prandtl number Eq. A-4 may be integrated between the surface and the combustion zone to yield

$$\frac{\dot{Q}_w}{\Delta h} = \frac{\tau_w}{u_b} \, Pr^{-0.67} \tag{A-5}$$

Dividing by $\rho_b u_b$ and using the usual definition of the skin friction coefficient, $c_f/2 = \tau_w/\rho_e u_e^2$, C_H is related to $c_f/2$ by

$$C_H = \frac{c_f}{2} \, Pr^{-0.67} \, \frac{\rho_e u_e^2}{\rho_b u_b^2} \tag{A-6}$$

If, in addition, a mass transfer number B is defined by

$$B = \frac{u_e}{u_b} \frac{\Delta h}{h_v} \tag{A-7}$$

the regression rate Eq. A-3 becomes for a unity Lewis number:*

---

* The present treatment may be easily extended to the case of Le $\neq$ 1. Appropriate corrections are discussed by Lees.[14]

$$\rho_f \dot{r} = \rho_e u_e \frac{c_f}{2} Pr^{-0.67} B \qquad \text{(A-8)}$$

The mass transfer number B may be regarded as a thermodynamic constant that characterizes the propellants, since the value of B is determined by physical properties of the gas-phase and solid-phase components. Also, since $B' \equiv Pr^{-0.67} B$ is the similarity parameter of a boundary layer with mass injection, the velocity profiles will have a similar shape everywhere in the boundary layer if B' is constant.[1] In a turbulent boundary layer, Pr is very near to unity so that B' and B are not just proportional but equal for practical purposes. Thus, B really plays a dual role as a thermochemical parameter and as a boundary layer flow parameter.

To put Eq. A-1 in a useful form, it is necessary to evaluate the skin friction coefficient c_f for a turbulent boundary layer with mass injection and combustion. The skin friction coefficient of an incompressible turbulent boundary layer is given by[21]

$$\frac{c_{f_o}}{2} = 0.03\ Re_x^{-0.2} \qquad \text{(A-9)}$$

It has been shown[1,22] that the effect of mass injection upon the friction coefficient can be expressed by

$$\frac{c_f}{c_{f_o}} = \left[\frac{\ell n(1 + B')}{B'}\right]^{0.8} \left[\frac{1 + \frac{13B'}{10} + \frac{4B'^2}{11}}{(1 + B')(1 + \frac{B'}{2})^2}\right]^{0.2} \qquad \text{(A-10)}$$

In the range $5 < B' < 100$, which corresponds to typical hybrid operation, Eq. 10 is adequately represented by the simpler formula:

$$\frac{c_f}{c_{f_o}} = 1.2B'^{-0.77} \qquad \text{(A-11)}$$

The presence of combustion manifests itself upon the skin friction coefficient by producing a variable property boundary layer. Variable property effects have been analyzed by many investigators, including Mager,[23] Burggraf,[24] and Crocco.[25] Marxman[6] has shown that the resulting skin friction correction appears as a multiplying density ratio of the form $(\bar{\rho}/\rho_e)^{0.6}$, where $\bar{\rho}$ is a suitably defined reference density. For most hybrid propellants of interest $\bar{\rho}/\rho_e$ can be taken as unity to a good approximation.[6]

The final expression for the regression rate with convective heat transfer alone is

$$\rho_f \dot{r} = 0.036 G (\bar{\rho}/\rho_e)^{0.6} B'^{0.23} Re_x^{-0.2} \qquad \text{(A-12)}$$

A notable fact revealed by Eq. A-12 is the strong coupling between the convective heat transfer and the mass injection rate which manifests itself in the small power on B'. This implies that large changes in either the heat of reaction (i.e., Δh) or the heat of gasification h_v will only induce small changes in the regression rate.

Radiative Heat Transfer

The heat transfer by radiation is formulated by analogy with an equilibrium flow, even though nonequilibrium conditions certainly exist in the hybrid boundary layer. This is done because little is known about nonequilibrium radiation. In this case

$$\dot{Q}_r = \sigma \varepsilon_w \varepsilon_g \left(T_r^4 - T_w^4 \right) \qquad \text{(A-13)}$$

where the parameter ε_g represents the emissivity of the radiating field. In all practical cases $T_w^4 \ll T_r^4$ and can therefore be neglected. A new formulation for ε_g is given in Appendix B.

It has been shown[6] that the convective and radiative heat transfer cannot be directly added because of the coupling that exists between the convective heat transfer and the mass injection rate. The energy of radiation tends to increase the rate of fuel vaporization, and this increase, in turn, tends to decrease the rate of convective heat transfer to the wall. The resulting trade-off can be expressed by[6]

$$\rho_f \dot{r} = \frac{\dot{Q}_c}{h_v} \left[e^{-\dot{Q}_r/\dot{Q}_c} + \frac{\dot{Q}_r}{\dot{Q}_c} \right] \tag{A-14}$$

where $\dot{Q}_c$ is the convective heat transfer that would be present in the absence of radiation. For small values of $\dot{Q}_r/\dot{Q}_c$ (such as would occur in a typical hybrid with low metal loading in the grain), the trade-off between the terms is nearly exact, and $\dot{r}$ can be calculated with little error by using $\dot{Q}_c$ alone.

Treatment of Particle Loading in the Grain

The preceding section considered the effect of radiation on the hybrid burning rate. Many systems that contain an appreciable metal loading in the fuel exhibit a significant radiative heat transfer to the grain because of the presence of solid combustion products. Systems also exist that have a high particle loading in the surface but exhibit little radiation because the products of combustion are gaseous. Therefore, it is necessary to determine the effect of particle loading on the regression rate of both radiative and nonradiative systems.

It can be shown that the presence of particles in the flow has a negligible direct effect on the shear stress distribution or velocity profile shape in the boundary layer.[26] From this, one can infer that the variation of c_f/c_{f_o} with surface injection should also be unaffected to first order by the addition of particles. However, it is physically

apparent that the blocking effect, which reduces c_f, should depend upon only the gas mass addition rate at the surface so long as the particles occupy negligible volume compared with that occupied by the gas, as they do in any practical application. Based on this assumption, the regression rate equation should be written in terms of the bulk density of the vaporizing component. This can be accomplished by defining an effective heat of gasification by the equation:

$$\rho_v h_{v_{eff}} = \rho_f h_v = \rho_v \left[\left(c_{p_v} + \frac{\rho_p}{\rho_v} c_m \right) \Delta T + L_v \right] \qquad \text{(A-15)}$$

$$= \rho_v \left(h_{v_b} + \frac{K}{1-K} c_m \Delta T \right)$$

This equation describes the fact that the one component is both heated to the surface temperature and vaporized, while the other component is only heated. The increase in the effective value of h_v with increasing metal loading tends to counteract the increase in the surface heat transfer, which is caused by the surface mass addition. These results indicate that the regression rate of a grain can be significantly increased by the mere addition of particles whether or not these particles provide any significant radiative heat transfer to the grain. The important grain density from the standpoint of regression rate is the bulk density of the binder.

Evaluation of the Mass Transfer Number

The mass transfer number B which is a governing parameter in the convective heat transfer equation, can be evaluated according to the scheme of Marxman.[6] This requires the calculation of both the sensible enthalpy difference between the flame zone and the regressing surface and the effective heat of gasification. The latter quantity is given by Eq. A-15. It can be shown[21] that the sensible enthalpy at the flame zone is equal to

the heat of reaction per unit mass of propellant (fuel and oxidizer) at the local mixture ratio which may be taken as three-fourths of the stoichiometric value.

The heat of reaction per unit mass of reactant is given by

$$Q_c = \Delta h = \frac{\Sigma \nu_r \Delta h_r^o - \Sigma \nu_p \Delta h_p^o}{\Sigma \nu_r M_r} \qquad \text{(A-16)}$$

A sample calculation for the Plexiglas*-oxygen hybrid system would proceed as follows: The stoichiometric mixture ratio for this system is 1.92. Assuming that the local O/F ratio at the flame is 1.4, the balanced reaction is

$$C_5H_8O_2 + 4.37\ O_2 \rightarrow 2.26\ CO + 2.74\ CO_2 + H_2O$$

Then, using standard heats of formation, the heat of reaction per unit mass is

$$Q_c = \frac{1(-92.8) - 2.26(-26.4) - 2.74(-94.1) - 4(-57.8)}{100 + 4.37\ (32)} \times 10^3 \qquad \text{(A-17)}$$

$$= 1900 \text{ cal/g} = 3430 \text{ Btu/lb}$$

Assuming the wall temperature is 600°K and the ambient temperature deep in the grain is 300°K, and using 0.4 cal/g -°K as the specific heat of the species at the wall,

$$\Delta h = 1900 - 0.4(300) = 1780 \text{ cal/g} \qquad \text{(A-18)}$$

Using a value of h_v of 350 cal/g results in

$$\frac{\Delta h}{h_v} \cong 5.1$$

---

* Trademark, Rohm & Haas, Co.

The mass transfer number B is now related to $\Delta h/h_v$ by the curve in Fig. A-1 (which is reproduced from Ref. 27). For the example above, the result is B = 9.3.

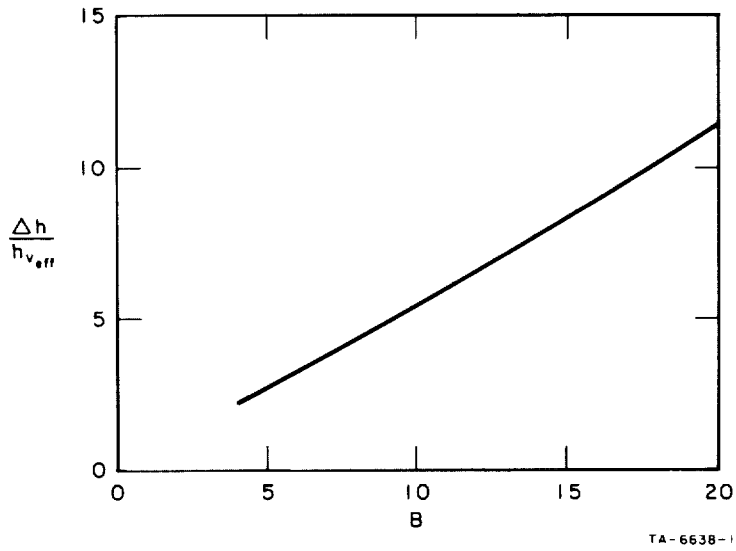

FIG. A-1 THEORETICAL HYBRID MASS TRANSFER NUMBER

Appendix B

GAS-PHASE EMISSIVITY

A calculation of gas-phase emissivity can be carried out by beginning with a fundamental description of the radiative process. Consider the radiation delivered to a cylindrical wall from an annular zone of high-temperature particles. In a hybrid motor with a cool core the radiative heat transfer comes from this type of annular region. The radiation delivered to an incremental area dA lying in the x-z plane (see Fig. B-1) from volume dV is

$$d^2\Phi = \frac{I\ dV}{4\pi r^2}\,\tau \sin\beta \cos\varphi\ dA \qquad \text{(B-1)}$$

where I is the intensity generated per unit volume at the location of dV and τ is the transmissivity of the intervening medium between dV and dA.

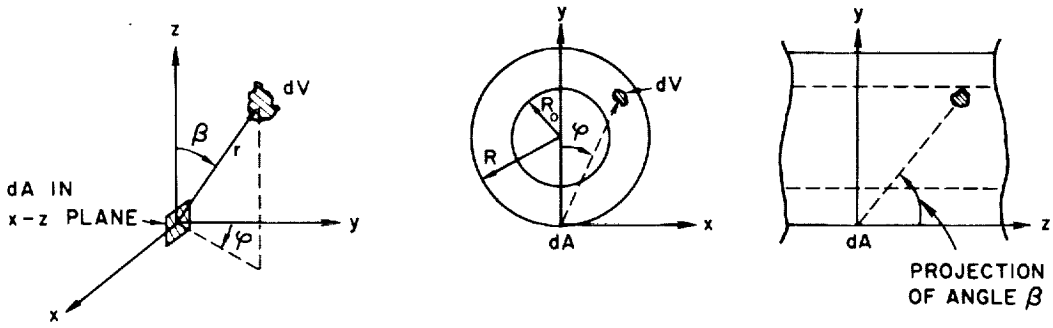

FIG. B-1 COORDINATE SYSTEM FOR CALCULATION OF EMISSIVITY

Assuming the emissivity of individual particles to be unity,

$$I = 4\pi r_p^2 n\sigma T_r^4 \tag{B-2}$$

The transmissivity is obtained by assuming the absorption process to be of first order; i.e.,

$$\frac{dI}{dr} = \gamma I \tag{B-3}$$

where γ is a constant. The solution is

$$\tau = \frac{I}{I_0} = e^{-\gamma r} \tag{B-4}$$

A photon of light will be intercepted by any particle whose center lies within the distance r_p from the path of the photon. If the particle emissivity (absorptivity) is unity, the absorptivity coefficient γ is equal to the average number of particles encountered per unit path length:

$$\gamma = \pi r_p^2 n \tag{B-5}$$

Using

$$dV = r^2 \sin\beta \, dr \, d\varphi \, d\beta \tag{B-6}$$

as the differential volume in spherical coordinates, the above equations can be combined to give

$$d^2\Phi = \sigma n r_p^2 T_r^4 e^{-\pi n r_p^2 r} \sin^2\beta \cos\varphi \, dr \, d\varphi \, d\beta \, dA \tag{B-7}$$

The gas-phase emissivity is then obtained by integrating over the volume after dividing by σT_r^4:

$$\varepsilon_g = n r_p^2 \int_\beta \int_\varphi \int_r e^{-\pi n r_p^2 r} \sin^2\beta \cos\varphi \, dr \, d\varphi \, d\beta \tag{B-8}$$

The integration limits for the integrals of Eq. B-8 can be established as follows: For $\varphi > \varphi_e = \sin^{-1}(R_0/R)$, the r integration can be carried out directly between r = 0 and the value of r established by the equation

$$2R \cos \varphi = r \sin \beta \tag{B-9}$$

For $\varphi < \varphi_e$ the r integration must be split into two parts to account for the fact that no radiation is generated in the cool core. The two regimes of r integration are given by

$$\left.\begin{aligned} 0 < r < s_1 &= \frac{R \cos \varphi - (R_0^2 - R^2 \sin^2 \varphi)^{\frac{1}{2}}}{\sin \beta} \\ \frac{2R \cos \varphi}{\sin \beta} - s_1 < r < \frac{2R \cos \varphi}{\sin \beta} &= s_2 \end{aligned}\right\} \tag{B-10}$$

The integration over β proceeds from a lower limit of zero to an upper limit which is dependent upon the z-coordinate of the end of the annulus and upon the value of the angle φ. At the end of the annulus

$$\beta = \tan^{-1} \frac{2R \cos \varphi}{z_e} = \beta_e \tag{B-11}$$

The final integral must then be multiplied by four to account for all four quadrants. Using the results above,

$$\begin{aligned} \varepsilon_g = \frac{4}{\pi} \int_0^{\varphi_e} \int_0^{\beta_e} \left[1 - e^{-\tau m r_p^2 s_1} + e^{-\tau m r_p^2 (s_2 - s_1)} - e^{-\tau m r_p^2 s_2} \right] \cos \varphi \sin^2 \beta \, d\beta \, d\varphi \\ + \frac{4}{\pi} \int_{\varphi_e}^{\pi/2} \int_0^{\beta_e} \left[1 - e^{-\tau m r_p^2 s_2} \right] \cos \varphi \sin^2 \beta \, d\beta \, d\varphi \end{aligned} \tag{B-12}$$

Because of the nature of the exponential functions in Eq. B-12 the integrals must be evaluated numerically.

The particle number density n that appears in this analysis can be calculated from[27]

$$n(x) = \frac{3\lambda}{4\pi} \frac{K}{1 - K} \frac{1}{\rho_p r_p^3} \frac{\rho_e}{\dot{m}_g} \int_0^x \rho_v \dot{r} P \, dx \tag{B-13}$$

for a grain containing nonvolatile material, and

$$n(x) = \frac{3K}{4\pi} \frac{1}{\rho_p r_p^3} \frac{\rho_e}{\dot{m}_g} \int_0^x \rho_v \dot{r} P \, dx \tag{B-14}$$

for a completely vaporizing grain. The density ρ_v is the bulk density of the vaporizing component of the grain.

An expression similar to Eq. B-12 can be developed to account for gas-phase radiation in systems that do not produce particulate combustion products. In this case the absorptivity coefficient γ is proportional to the pressure

$$\gamma = \alpha p$$

where the proportionality constant α must be obtained experimentally.

Appendix C

DIFFUSION-LIMITED REGRESSION RATE CALCULATIONS

A computer program based on the work in Appendices A and B was written in BASIC language for solution at a time-sharing computer terminal. A complete description of the program, including a sample output format, is given at the end of this discussion. The regression behavior of circular cylinders is described, such as those studied experimentally during the current program.

Theoretical calculations of the mass transfer number for the polyurethane (PU) and polybutadiene-acrylic-nitrile (PBAN) binder systems have been carried out as a function of metal loading, with oxygen considered as the oxidizer. The results are shown in Fig. C-1.

The gas flow rate $\dot{m}_g$, which enters both the convective heat transfer expression and the expression for the particle number density, must account

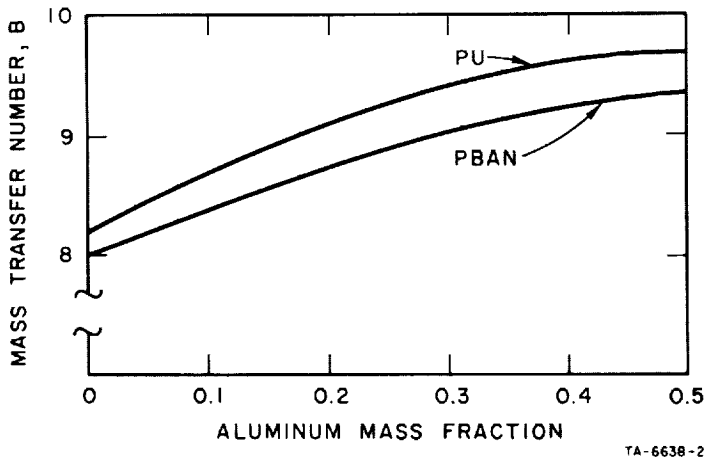

FIG. C-1 VARIATION OF MASS TRANSFER NUMBER WITH ALUMINUM LOADING FOR PU AND PBAN BINDERS

for the oxidizer used in the production of particles. It is composed of the head-end oxidizer flow rate plus the gas evolved from the surface minus the oxidizer used to form the combustion particles. The resulting expressions are[27]

$$\dot{m}_g = \dot{m}_o + \left(1 - \frac{K\zeta}{1-K}\right) \int_0^x \rho_v \dot{r} P \, dx \qquad \text{(C-1)}$$

if particles in the grain produce particulate combustion products,

$$\dot{m}_g = \dot{m}_o + \frac{1}{1-K} \int_0^x \rho_v \dot{r} P \, dx \qquad \text{(C-2)}$$

if particles in the grain produce only gaseous combustion products, and

$$\dot{m}_g = \dot{m}_o + (1 - K_1 - K_1\zeta_1) \int_0^x \rho_v \dot{r} P \, dx \qquad \text{(C-3)}$$

if a completely vaporizing grain produces particulate combustion products. The mass of oxidizer consumed in producing the product particles is accounted for by ζ and ζ_1.

The results of regression rate calculations for the hybrid systems utilized during the current program are shown and discussed in Section IV, Experimental Studies. It should be emphasized that the analysis embodied by the computer code described below is restricted to the transport-limited domain of hybrid combustion wherein chemical kinetics do not exert any controlling influence.

The inputs required for operation of the program are shown in Fig. C-2. The equations which are solved can be concisely stated as follows (Cases 1, 2, and 3 referred to below are described in Fig. C-2):

$$\rho_v \dot{r} = \rho_f \dot{r} \, (1 - K) = \frac{\dot{Q}_c}{h_{v_{eff}}} \left[e^{-\dot{Q}_r/\dot{Q}_c} + \frac{\dot{Q}_r}{\dot{Q}_c} \right] \qquad \text{(C-4)}$$

```
HY-EXP     12:35    SF MON 09/16/68

100 THE PROGRAM ENTITLED "HY" IS BASED UPON HEAT-TRANSFER
101 LIMITED HYBRID THEORY.  IT CALCULATES THE REGRESSION BE-
102 HAVIOR OF A CIRCULAR TUBE FUEL GRAIN.  THE INPUTS WHICH ARE
103 NECESSARY FOR OPERATION OF THE PROGRAM ARE DEFINED AS
104 FOLLOWS ACCORDING TO THE LINE NUMBERS OF "HY":
105            50 DO--INITIAL INNER DIAM. (IN.)
106            51 L --LENGTH  (IN.)
107            52 D2--OUTER DIAM.  (IN.)
108            53 K --MASS FRACTION OF NON-VOLATILE SURFACE MAT'L.
109            54 K1--MASS FRACTION OF VOLATILE SURFACE MAT'L.
110                   WHICH FORMS PARTICULATE COMBUSTION PRODUCTS
111            55 K2--TOTAL DENSITY OF FUEL GRAIN  (LB/IN3)
112            56 K3--EFFECTIVE HEAT OF GASIFICATION  (BTU/LB)
113            57 MO--OXIDIZER FLOW RATE  (LB/SEC)
114                    (IF MO VARIES, IT MAY EITHER BE READ AS
115                     DATA OR DESCRIBED BY AN EQUATION.)
116            58 PO--CHAMBER PRESSURE  (PSIA)  (SEE THE ABOVE.)
117            59 J --CASE NUMBER
118                    J=1  IF PARTICLES IN THE GRAIN PRODUCE
119                         PARTICULATE COMBUSTION PRODUCTS
120                    J=2  IF PARTICLES IN THE GRAIN PRODUCE
121                         GASEOUS COMBUSTION PRODUCTS
122                    J=3  IF A COMPLETELY VOLATILE GRAIN PRODUCES
123                         PARTICULATE COMBUSTION PRODUCTS
124            60 UO--OXIDIZER TEMP. AT INLET  (OR)
125             61 U5--COMBUSTION TEMP. AT AN O/F RATIO WHICH IS
126                    3/4 OF THE STOICHIOMETRIC VALUE AT 5 ATM.
127                    PRESSURE (OR)
129            64 C7--GAS-PHASE RADIATION CONST.
130            65 K4--MASS OF OXIDIZER CONSUMED PER UNIT MASS OF
131                   NON-VOLATILE SURFACE MAT'L. IN PRODUCING
132                   PARTICULATE COMBUSTION PRODUCTS
133            66 K5--MASS OF OXIDIZER CONSUMED PER UNIT MASS OF
134                   VOLATILE SURFACE MAT'L. IN PRODUCING
135                   PARTICULATE COMBUSTION PRODUCTS
136            67 C8--MASS OF PARTICULATE COMBUSTION PRODUCTS
137                   FORMED PER UNIT MASS OF NON-VOLATILE
138                   SURFACE MAT'L.
139            69 E2--EMISSIVITY (ABSORPTIVITY) OF FUEL SURFACE
140            70 B --MASS TRANSFER NUMBER
141            73 K6--DENSITY OF PARTICULATE COMBUSTION PRODUCTS (LB/IN3)
142            77 C2--BOUNDARY LAYER DENSITY CORRECTION FACTOR
143            78 S --OXIDIZER VISCOSITY AT TEMP. UO (LB/IN-SEC)
144            82 T1--TIME INCREMENT FOR CALCULATIONS (SEC)
145            83 T2--QUIT TIME (SEC)
146            84 T3--TIME INCREMENT FOR PRINTOUT (SEC)
147            85 X1--DISTANCE INCREMENT FOR CALCULATIONS (X/L)
148            103 PUT IN THE NAMES OF THE FUEL AND OXIDIZER BY
149                TYPING E.G.,
150                      103 PRINT "PMM","OXYGEN"
```

FIG. C-2 SUMMARY OF INPUT REQUIRED FOR HYBRID COMPUTER CODE

$$\frac{\dot{Q}_c}{h_{v_{eff}}} = 0.036 \left(\frac{\dot{m}_g}{A_p}\right)^{0.8} \left(\frac{x}{\mu}\right)^{-0.2} \quad B^{0.23} \tag{C-5}$$

$$\left.\begin{aligned} \dot{m}_g &= \dot{m}_o + \left(1 - \frac{K\zeta}{1-K}\right) \int_o^x \rho_v \dot{r}\, \pi\, D\, dx \qquad \text{(Case 1)} \\ \dot{m}_g &= \dot{m}_o + \frac{1}{1-K} \int_o^x \rho_v \dot{r}\, \pi\, D\, dx \qquad \text{(Case 2)} \\ \dot{m}_g &+ \dot{m}_o + (1 - K_1 - K_1\zeta_1) \int_o^x \rho_v \dot{r}\, \pi\, D\, dx \qquad \text{(Case 3)} \end{aligned}\right\} \tag{C-6}$$

$$A_p = \frac{\pi}{4} (D - 2\delta^*)^2 \tag{C-7}$$

$$2\delta^* = \begin{cases} 0.21\ D\ (x/5D)^{0.8} & x \le 5D \\ 0.21\ D & x > 5D \end{cases} \tag{C-8}$$

$$\dot{Q}_r = \sigma\, \epsilon_w\, \epsilon_g\, T_r^4 \tag{C-9}$$

$$\epsilon_g = \frac{4}{\pi} \int_o^{\varphi_e} \int_o^{\beta_e} \left(1 - e^{-\gamma s_1} + e^{-\gamma(s_2 - s_1)} - e^{-\gamma s_2}\right) \cos\varphi \sin^2\beta\, d\beta\, d\varphi$$

$$+ \frac{4}{\pi} \int_{\varphi_e}^{\pi/2} \int_o^{\beta_e} \left(1 - e^{-\gamma s_2}\right) \cos\varphi \sin^2\beta\, d\beta\, d\varphi \tag{C-10}$$

$$\gamma = \begin{cases} \pi\, n r_p^2 & \text{(Cases 1 and 3)} \\ \alpha\ p & \text{(Case 2)} \end{cases} \tag{C-11}$$

$$\left.\begin{aligned} \varphi_e &= \sin^{-1}\ (R_o/R) \\ \beta_e &= \tan^{-1}\ \frac{2R\cos\varphi}{Z_e} \end{aligned}\right\} \qquad \text{(C-12)}$$

$$\left.\begin{aligned} s_1 &= \frac{R\cos\varphi - (R_o^2 - R^2\sin^2\varphi)^{\frac{1}{2}}}{\sin\beta} \\ s_2 &= \frac{2R\cos\varphi}{\sin\beta} \end{aligned}\right\} \qquad \text{(C-13)}$$

$$\left.\begin{aligned} n &= \frac{3\lambda}{4\pi}\frac{K}{1-K}\frac{1}{\rho_p r_p^3}\frac{\rho_e}{\dot{m}_g}\int_o^x \rho_v \dot{r}\,\pi D\,dx \qquad \text{(Case 1)} \\ n &= \frac{3K_1}{4\pi}\frac{1}{\rho_p r_p^3}\frac{\rho_e}{\dot{m}_g}\int_o^x \rho_v \dot{r}\,\pi D\,dx \qquad \text{(Case 3)} \end{aligned}\right\} \qquad \text{(C-14)}$$

$$T_r \cong 2T_f/3 \qquad \text{(C-15)}$$

$$h_{v_{eff}} = h_{v_b} + \frac{K}{1-K} c_m (T_w - T_o) \qquad \text{(C-16)}$$

The general solution proceeds as follows:

1. Calculate $\dot{Q}_c/h_{v_{eff}}$
2. Calculate $\dot{m}_g$
3. Calculate n (if required)
4. Calculate $\dot{Q}_r$
5. Calculate $\dot{r}$

The details of this computational procedure are shown in the printout of the computer code given in Fig. C-3.

```
PY          12:17    SF MON 09/16/68

 49 LET F3=0
 50LETD0=1
 51LETL=12
 52LETD2=2.5
 53 LET K=0
 54 LET K1=0
 55 LET K2=3.80106E-2
 56LETK3=630
 57LETM0=.086
 58 LET P0=200
 59 LET J=2
 60 LET U0=160
 61 LET U5=3934*1.8
 62LETU2=U5*(1+3.33E-4*(P0-75))
 63 LET F6=3
 64 LET C7=0.003
 65 LET K4=0.886
 66 LET K5=0
 67 LET C8=1.888
 68 LET E1=3.307E-15
 69 LET E2=.9
 70 LET R=9.6
 71 DIM D(100)
 72 DIM N(100)
 73 LET K8=0.1437
 74 LET C6=(3*2.54E4)/(4*K8*K6)
 75 LET J1=1
 76 LET C1=0.036
 77 LET C2=1
 78 LET S=1.02 E-6
 79 LET C3=(S/L)↑0.2
 80 LET C5=3.14159
 81 LET C4=C5/4
 82 LET T1=0.25
 83 LET T2=10
 84 LET T3=.5
 85 LET X1=0.02
 87 LET Y=0
 88 LET U1=2*U2/3
 92 PRINT
 96 LET I4=INT(.1/X1+1/2)
100 PRINT
101 PRINT "FUEL","OXIDIZER"
103 PRINT "PE", "O2-E2"
106 PRINT
111 PRINT "INITIAL COND."
112 PRINT
114 PRINT "DIAM.","LENGTH","DENSITY","EFF. R-SUB-V"
116 PRINT D0,L,K2,K3
117 PRINT
118 PRINT "REF","PRESS.","OXID. FLOW","INLET TEMP.","FLAME TEMP."
120 PRINT R,P0,M0,U0,U2
121 PRINT
122 PRINT "RAD. TEMP.","GAS CONST.","WALL ABSORPT."
124 PRINT U1,C7,E2
125 PRINT
```

FIG. C-3 HYBRID REGRESSION RATE COMPUTER CODE

```
126 PRINT "METAL PCT.","PAINT. PCT.","ZETA","ZETA-1","LAMBDA"
128 PRINT K,K1,K4,K5,C8
129 PRINT
130 PRINT "DEL-T","DEL-X/L","PRINT TIME","QUIT TIME","CASE"
132 PRINT T1,X1,T3,T2,J
134 PRINT
135 PRINT
140 LET Q6=C1*C2*C3*(B)↑0.23
145 LET T4=0
147 LET T5=0
150 LET T=0
155 LET X=X1
156 LET I=1
157 LET I1=I4
160 LET M=M0
165 IF T>0 THEN 175
170 LET D(I)=D0
175 LET R3=(X*L)/(5*D(I))
180 IF R3<=1 THEN 190
181 IF R3>5 THEN 200
182 IF R3>1 THEN 210
190 LET E=D(I)*(1-0.21*(R3)↑0.8)
195 LET U=U0
196 GO TO 220
200 LET E=D(I)*(1-0.21)
205 LET U=U2
206 GO TO 220
210 LET E=D(I)*(1-0.21)
215 LET U=U0+((U2-U0)/4)*(R3-1)
220 LET A=C4*(E)↑2
225 LET Q1=Q6*(X)↑(-0.2)*(M/A)↑0.8
230 LET Q3=C5*Q1*D0*X1*L
235 LET P1=Q1/(K2*(1-K))
240 IF J=1 THEN 255
245 IF J=2 THEN 345
250 IF J=3 THEN 300
255 IF I>1 THEN 280
260 LET M=M0+(1-K*K4/(1-K))*Q3
261 LET M1=M0+Q3*1/(1-K)
265 LET Q5=Q3
270 LET N(I)=C6*C8*K/(1-K)*P0/U*1/M*Q3*(R3)↑(-0.8)
271 GO TO 366
280 LET M=M+(1-K*K4/(1-K))*Q4
281 LET M1=M1+Q4*1/(1-K)
285 IF R3>1 THEN 295
290 LET N(I)=C6*C8*K/(1-K)*P0/U*1/M*Q5*(R3)↑(-0.8)
291 GO TO 366
295 LET N(I)=C6*C8*K/(1-K)*P0/U*1/M*Q5
296 GO TO 366
300 IF I>1 THEN 325
305 LET M=M0+(1-K1-K1*K5)*Q3
306 LET M1=M0+Q3
310 LET Q5=Q3
315 LET N(I)=C6*K1*P0/U*1/M*Q3*(R3)↑(-0.8)
316 GO TO 366
325 LET M=M+(1-K1-K1*K5)*Q4
326 LET M1=M1+Q4
330 IF R3>1 THEN 340
335 LET N(I)=C6*K1*P0/U*1/M*Q5*(R3)↑(-0.8)
336 GO TO 366
340 LET N(I)=C6*K1*P0/U*1/M*Q5
```

FIG. C-3 Continued

```
341 GO TO 366
345 IF I>1 THEN 360
350 LET M=M0+(1/(1-K))*D3
351 LET M1=M
355 LET N(I)=C7*P0
356 GO TO 366
360 LET M=M+(1/(1-K))*D4
361 LET M1=M
365 LET N(I)=C7*P0
366 IF J1=2 THEN 371
368 LET P2=P1
370 GO TO 390
371 IF J=2 THEN 384
372 IF N(I)>0 THEN 375
373 LET P2=P1
374 GO TO 390
375 IF I<I4 THEN 382
376 IF I>=*I4 THEN 382
378 IF I=I1 THEN 382
380 GO TO 387
382 IF I=15 THEN 590
383 GO TO 387
384 IF I>2*I4 THEN 387
385 GO TO 375
387 LET D2=P1*P2/K3*E3*(D1)↑4
388 LET P2=D1*(D2/D1+EXP(-D2/D1))/(K2*(1-K))
390 LET D4=C5*K2*(1-K)*P2*D(I)*X1*L
391 LET D5=D5+D4
395 IF I=I1 THEN 495
400 LET D(I)=D(I)+2*P2*T1
401 IF D(I)>D2 THEN 795
405 IF X>0.995 THEN 425
410 LET I=I+1
415 LET X=X+X1
420 GO TO 165
425 IF T=0 THEN 450
430 LET M3=(M1+M2)/2-M0
435 LET M=M+M3*T1
440 LET M2=M1
442 IF T=T4 THEN 455
444 LET T=T+T1
446 IF T>T2 THEN 800
448 GO TO 155
450 LET M2=M1
452 IF J1=2 THEN 455
453 LET J1=2
454 GO TO 155
455 PRINT
460 PRINT "AVG. DEL-P","WT. LOSS","GAS FLOW","TOTAL FLOW","G-O"
461 LET D6=(V/(C4*K2*L)+(D0)↑2)↑0.5
465 PRINT (D6-D0)/2,M*453.6,M,M1,M0/(C4*(D6)↑2)
470 PRINT
471 PRINT
475 LET T=T+T1
476 LET T4=T4+T3
490 IF T>T2 THEN 800
490 GO TO 155
495 IF T=T4 THEN 506
496 LET D(I)=D(I)+2*P2*T1
500 LET I1=I1+I4
505 GO TO 405
506 IF J1=2 THEN 510
```

FIG. C-3 Continued

```
508 GO TO 405
510 IF I1=I4 THEN 520
515 GO TO 535
520 PRINT "TIME"
525 PRINT T
526 PRINT
530 PRINT "DISTANCE","REG. RATE","DEL-R","AREA","EMISSIVITY"
531 PRINT
535 PRINT X,R2,(D(I)-D0)/2,C4*(D(I))↑2,E3
536 PRINT "--",R1,"--",C4*(F)↑2
540 LET D(I)=D(I)+2*R2*T1
541 IF D(I)>D2 THEN 795
545 LET I1=I1+I4
550 GO TO 405
590 LET T5=T5+(2*T3)
600 LET R=D(I)/2
605LETR0=R-0.25
610 LET Y1=3.14159/30
615 LET Y2=ATN(1/((R*R)/(R0*R0)-1)↑(0.5))
625 LET E3=0
631 LET J5=1
633 LET K9=1
634 LET Y=Y1/100
635 LET Z=3.14159/2
640 LET J4=1
645 LET Y3=2*R*COS(Y)
646 IF Y>Y2 THEN 650
648 LET S3=(Y3/2-(R0*R0-R*R*(SIN(Y))↑2)↑(0.5))/SIN(Z)
650 LET X3=J4*X1*L
655 LET S4=Y3/SIN(Z)
660 IF Y<Y2 THEN 666
662 LET K9=0
664 LET S3=0
666 IF J5=1 THEN 670
667 LET S5=K9*EXP(-N(I-J4)*S3)-K9*EXP(-N(I-J4)*(S4-S3))+EXP(-N(I-J4)*S4)
668 GO TO 675
670 LET S5=K9*EXP(-N(I+J4)*S3)-K9*EXP(-N(I+J4)*(S4-S3))+EXP(-N(I+J4)*S4)
675 LET S6=(1-S5)*(SIN(Z))↑2*COS(Y)
680 LET Z1=(Y3*X1*L)/((X3)↑2+(Y3)↑2)
685 LET S7=S6*Z1*Y1*2/3.14159
690 LET E3=E3+S7/1.06988
695 LET Z=Z-Z1
700 LET J4=J4+1
701 IF J5=1 THEN 705
702 IF J4>I THEN 720
703 IF J4>10 THEN 720
704 GO TO 645
705 IF J4>1/X1-I THEN 720
706 IF J4>10 THEN 720
715 GO TO 645
720 LET Y=Y+Y1
725 IF Y>3.14159/2 THEN 745
740 GO TO 635
745 IF J5=2 THEN 750
746 LET J5=2
748 GO TO 633
750 GO TO 367
795 PRINT "SPECIFIED EXTERNAL DIAMETER EXCEEDED"
800 END
```

FIG. C-3 Concluded

Results of a typical calculation are shown in Fig. C-4 for a 1-in. Plexiglas (polymethylmethacrylate) grain. At each position, the regression rate that would have been obtained in the absence of radiation is printed out below the total regression rate. In this particular system, the radiation is so low that it produces little effect on the regression rate, partly because of the trade-off between radiative and convective heat transfer. Two port areas are also printed out at each position; the first is the geometric area and the second is the true flow area that is the geometric area minus the area occupied by the boundary layer displacement thickness. The flow area must be used in the calculation of the mass flux which enters the convective heat transfer equation. Results obtained for other hybrid propellant combinations are given in the main text of this report.

FUEL	OXIDIZER
PMM	O2

INITIAL COND.

DIAM.	LENGTH	DENSITY	EFF. N-SUB-V	
1	12	.0433	630	
GEE	PRESS.	OXID. FLOW	INLET TEMP.	FLAME TEMP.
9.3	215	.086	700	6101.79
RAD. TEMP.	SOLID CONST.	GAS CONST.	WALL ABSORPT.	
4067.86	0	.0005	.5	
METAL PCT.	PART. PCT.	ZETA	ZETA-1	LAMBDA
0	0	0	0	0
DEL-T	DEL-X/L	PRINT TIME	QUIT TIME	CASE
.25	.02	2	16	2

TIME
0

DISTANCE	REG. RATE	DEL-R	AREA	EMISSIVITY
.1	1.75571 E-2	0	.785398	.101923
--	1.74777 E-2	--	.693609	
.2	.017114	0	.785398	.101923
--	1.70327 E-2	--	.612729	
.3	1.75644 E-2	0	.785398	.101923
--	1.74851 E-2	--	.552242	
.4	1.74282 E-2	0	.785398	.101923
--	1.73526 E-2	--	.493575	
.5	1.73075 E-2	0	.785398	.101923
--	1.72314 E-2	--	.490167	
.6	1.71726 E-2	0	.785398	.101923
--	1.70956 E-2	--	.490167	
.7	1.70242 E-2	0	.785398	.101923
--	1.69465 E-2	--	.490167	
.8	.016936	0	.785398	.101923
--	1.67579 E-2	--	.490167	
.9	.016792	0	.785398	.101923
--	1.67137 E-2	--	.490167	
1.	1.67016 E-2	0	.785398	.101923
--	1.67033 E-2	--	.490167	

AVG. DEL-R	PT. LOSS	GAS FLOW	TOTAL FLOW	G-O
0	0	.115455	.115455	.109499

FIG. C-4 TYPICAL OUTPUT FORMAT FOR COMPUTER CALCULATIONS OF HYBRID REGRESSION RATES

TIME
2

DISTANCE	REG. RATE	DEL-R	AREA	EMISSIVITY
.1	1.57422 E-2	3.34386 E-2	.393961	.108357
--	1.56427 E-2	--	.793757	
.2	1.53011 E-2	3.25521 E-2	.390992	.108187
--	1.51991 E-2	--	.704179	
.3	1.55741 E-2	.033282	.393436	.108327
--	1.54735 E-2	--	.640423	
.4	1.61549 E-2	3.47364 E-2	.393316	.108606
--	1.60573 E-2	--	.595579	
.5	1.63661 E-2	3.48203 E-2	.393593	.108622
--	1.62693 E-2	--	.560915	
.6	1.61642 E-2	3.43915 E-2	.397124	.108538
--	1.60668 E-2	--	.559395	
.7	1.60325 E-2	3.41001 E-2	.396179	.108474
--	1.59345 E-2	--	.559395	
.8	.01595	3.39288 E-2	.395604	.108451
--	1.58515 E-2	--	.558947	
.9	1.59036 E-2	3.38383 E-2	.395301	.108433
--	1.58049 E-2	--	.558757	
1.	1.58846 E-2	3.38092 E-2	.395203	.108428
--	1.57859 E-2	--	.558696	

AVG. DEL-R	WT. LOSS	GAS FLOW	TOTAL FLOW	G-0
3.40095 E-2	5.74042 E-2	.114009	.114009	9.59955 E-2

TIME
4

DISTANCE	REG. RATE	DEL-R	AREA	EMISSIVITY
.1	1.43593 E-2	6.36564 E-2	.993211	.114131
--	1.42337 E-2	--	.330206	
.2	1.39283 E-2	6.18957 E-2	.991334	.113796
--	1.38048 E-2	--	.792161	
.3	1.40936 E-2	6.30692 E-2	.996031	.114019
--	.013971	--	.725012	
.4	1.45041 E-2	6.55232 E-2	1.00473	.114476
--	.014384	--	.663705	
.5	1.48959 E-2	6.62046 E-2	1.00716	.114616
--	1.47736 E-2	--	.623566	
.6	1.47174 E-2	6.53736 E-2	1.00424	.11446
--	.014599	--	.626744	
.7	1.45932 E-2	6.48504 E-2	1.00234	.114359
--	1.44791 E-2	--	.625562	
.8	1.45207 E-2	6.45135 E-2	1.00117	.114295
--	.014401	--	.624827	
.9	1.44737 E-2	6.43345 E-2	1.00051	.11426
--	1.43539 E-2	--	.62442	
1.	1.44501 E-2	.064263	1.00026	.114246
--	.01433	--	.624262	

AVG. DEL-R	WT. LOSS	GAS FLOW	TOTAL FLOW	G-0
6.45839 E-2	.112234	.112961	.112961	.09589

FIG. C-4 Concluded

Appendix D

DEVELOPMENT OF A MODEL FOR THE PRESSURE-SENSITIVE DOMAIN

At high pressures a thin turbulent diffusion flame is established in the boundary layer at a position where the local mixture ratio will allow combustion. Under these conditions the gas-phase reaction rates are large compared to the turbulent transport rates, and the latter are then the rate-controlling factors. As the pressure is decreased, the reaction rates decrease, the flame zone broadens, and the combustion process approaches that of a premixed turbulent flame; i.e., the combustion time becomes long compared to the mixing time.

An important point to consider is whether the gross kinetics effect on the regression rate is caused by the behavior of the heterogeneous surface reactions associated with the decomposition of the solid or by the behavior of the gas-phase reactions. When gas-phase reaction rates are high, the mainstream oxidizer mass fraction must be low between the flame zone and the wall, because high reaction rates imply a thin flame zone and consequent effective utilization of the oxidizing species. Thus, in this case, any heterogeneous reactions at the surface will be controlled by the diffusion of the small proportion of oxidizing species that is available to the wall. Since, by Reynolds analogy, the diffusional transport of mass momentum and energy is governed by the same equation, no correction to the basic hybrid model is required to cover this case. It can be concluded that the presence of pressure-sensitive heterogeneous reactions at the gas-solid interface does not explain the observed decrease in regression rates at low pressure.

The foregoing argument indicates that the gas-phase reaction rates at low pressure must be examined in order to explain the regression rate behavior. The physical explanation of the general process is that at high pressures, the gas-phase reaction rates are fast enough to consume all of the available material that is being vaporized at the surface. As the pressure is lowered, however, the gas-phase reaction rates decrease, and finally a point is reached where the flame cannot efficiently consume all of the vaporizing material and the local mixture ratio of the flame begins to shift. This shift in mixture ratio leads to a decrease in heat release, which in turn decreases the vaporization rate of the surface. At pressure well below the threshold level where the chemical reaction time is much longer than the gas-phase mixing time, the flame behavior approaches that of a premixed flame.

A detailed solution of the complete turbulent boundary layer equations, involving not only chemical kinetics but also the interaction between the turbulence mechanism and the combustion process, is obviously beyond the current scope of our understanding. These considerations naturally lead to an inquiry into whether the simplified turbulent flame theory developed in the past for premixed flames[28] can be applied to the hybrid case in which there is a transition from a premixed flame to a diffusion flame as the pressure increases. An excellent review of the wrinkled-flame-sheet turbulent flame theory has been given by Karlovitz.[28]

The theory of Karlovitz is a one-dimensional theory; therefore its applicability to a two-dimensional boundary layer problem must be carefully considered. The use of a one-dimensional theory as a first approximation is supported by schlieren photographs, which consistently show that most of the heat release takes place very chose to the surface even at low pressures.[1] Furthermore, in the vicinity of the surface, a one-dimensional approximation describes the turbulent transport processes very well,[20] lending credence to the present approach.

Application to the problem at hand leads to a description of the regression rate behavior in terms of the ratio t/T, where T is the characteristic mixing time corresponding to turbulent diffusion, and t is the characteristic reaction time for a premixed zone of dimensions corresponding to the turbulence scale.

The mean-square displacement of a particle from its original position by turbulent fluctuations is described by the equation[28]

$$\frac{d}{dt}\,\overline{X^2} = 2\,u'^2 \int_o^t R_t\,dt \qquad \text{(D-1)}$$

If the correlation function is assumed to be given by

$$R_t = e^{-t/T} \qquad \text{(D-2)}$$

Eq. D-1 can be evaluated to give the rms displacement:

$$(\overline{X^2})^{\frac{1}{2}} = u'\,t\left(\frac{2T}{t}\right)^{\frac{1}{2}}\left[1 - \frac{T}{t}\,(1 - e^{-t/T})\right]^{\frac{1}{2}} \qquad \text{(D-3)}$$

The average flame speed in the gas phase is given by:

$$S = \frac{(\overline{X^2})^{\frac{1}{2}}}{t_1} = u'\left(\frac{2T}{t_1}\right)^{\frac{1}{2}}\left[1 - \frac{T}{t_1}\,(1 - e^{-t_1/T})\right]^{\frac{1}{2}} \qquad \text{(D-4)}$$

In the mixing (heterogeneous) limit, $t_1/T \to 0$ and $S \to u'$ where u' is a characteristic turbulent velocity in the combustion zone. Since the turbulent flame speed must be compatible with the regression rate at the wall, the regression rate ratio is given by

$$\frac{\dot{r}}{\dot{r}_\infty} = \left(\frac{2T}{t_1}\right)^{\frac{1}{2}}\left[1 - \frac{T}{t_1}\left(1 - e^{-t_1/T}\right)\right]^{\frac{1}{2}} \qquad \text{(D-5)}$$

The remaining task is to express the ratio t_1/T in terms of flow parameters such as pressure and temperature.

From a physical point of view, it is convenient to express the time ratio in terms of length and velocity ratios as

$$\frac{t_1}{T} = \frac{\ell_1}{u_f} \frac{u'}{\ell_2} \tag{D-6}$$

In Eq. 41, ℓ_1 is the distance that the flame front propagates into unburned gas at the (kinetic) flame speed u_f while ℓ_2 is a characteristic scale of turbulence. Using the Denison and Baum formulation[39] for the flame speed u_f and the asymptotic behavior of S to describe u', the time ratio becomes

$$\frac{t_1}{T} = C \frac{\ell_1}{\ell_2} \frac{GRe_x^{-0.2} B^{0.23}}{p^{n/2} U_f^{1+n/2} \exp(-E_f/2RU_f)} \tag{D-7}$$

The constant C is required to complete the kinetic formulation of u_f and must be determined by comparison with data.

The length ℓ_2, which can be thought of as related to the integral scale of turbulence, is probably nearly constant over a wide range of flow conditions. On the other hand, the length ℓ_1 could, for example, conceivably depend upon the mass flux because of changes induced in the relative availability of fuel and oxidizer in the vicinity of the flame zone by changes in the mass flux. At present the disposition of this point must be left to experiment.

Appendix E

REGRESSION RATE MEASUREMENTS WITH OXYGEN

The basic components of the $2\frac{1}{2}$-in.-diameter motor that was used to obtain regression rate measurements in the low-pressure regime are shown in exploded view in Fig. E-1. A 12-in.-long flow-straightening section is used upstream of the inlet to the grain to ensure uniform flow conditions. Screens and a porous plate are used at the injector end of the straightening section to help spread the incoming stream from the injector. At the grain end of the straightening section, an inlet for propane and a spark plug are provided as the ignition system.

An existing flow control facility was adapted for the gaseous oxidizers used in the small-scale tests. The facility was designed for liquid engine tests with cyrogenic oxidizers and therefore was constructed of 304 stainless steel with Teflon* and/or Kel-F† seats and seals. The flow system schematic is shown in Fig. E-2. The oxidizer mass flow is kept constant throughout a test by passing the flow through a sonic choke that is operated above the critical pressure ratio.

The grain is ignited by preflowing a small amount of oxygen and propane into the chamber and igniting it with a spark plug. The ignition system is preset so that it operates near the lower flammability limit for the oxygen-propane mixture, thus yielding an oxygen-rich high-temperature source. The time for the flame to spread from the head end of the grain

---

* Trademark, E. I. duPont de Nemours and Co.

† Trademark, 3M Company.

FIG. E-1 SMALL-SCALE TUBULAR HYBRID MOTOR

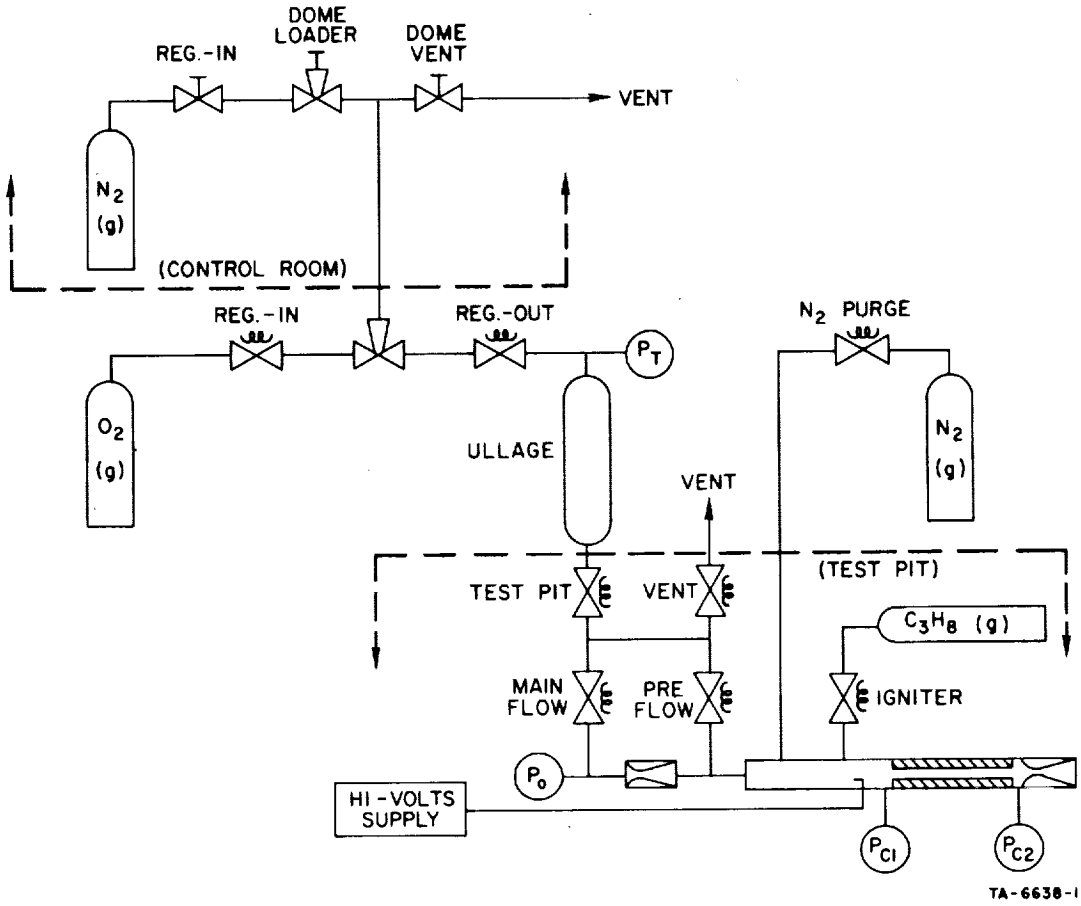

FIG. E-2 OXYGEN FLOW-CONTROL SYSTEM

to the nozzle end was determined to be approximately one second. Therefore, the main flow valve was delayed for that length of time. The weight of fuel typically consumed during this ignition process was determined to be 0.5 g which is about 1 percent of the amount of fuel that would be consumed in a 5-sec test at a regression rate of 0.01 in./sec.

An automatic sequencer actuates the system. The run duration is set and the events proceed as follows:

Zero time	Pressure-recording oscillograph on
+1.9 sec	Oxidizer preflow valve open
+2.0 sec	Propane valve open and spark source on
+2.9 sec	Oxidizer main flow open
+3.0 sec	Oxidizer preflow and propane valves closed
+8, 13, or 18 sec	Oxidizer main flow closed; nitrogen purge valve open

Event markers are recorded on the oscillograph along with pressure-time data obtained from strain-gage transducers at the entrance and exit of the combustion changer. Running times of 5, 10, and 15 sec were chosen to obtain the regression rate/time dependence.

To check the experimental apparatus, weight loss data were obtained for the Plexiglas-oxygen propellant combination and compared with the predicted numerical results. This system was chosen because it has been extensively documented in the literature.[2,26]

Data were obtained at 5-, 10-, and 15-sec intervals for chamber pressures of 45, 115, and 215 psia. The results are shown in Fig. E-3. The regression rate, and therefore the weight loss, lessens as the pressure is lowered, indicating that the burning process is not entirely heat-transfer controlled at low pressures but that chemical kinetics must play a role. Previous results have indicated that the heat-transfer controlled limit, corresponding to the theoretical curve, is reached in the neighborhood of 265 psia[26] for this propellant combination.

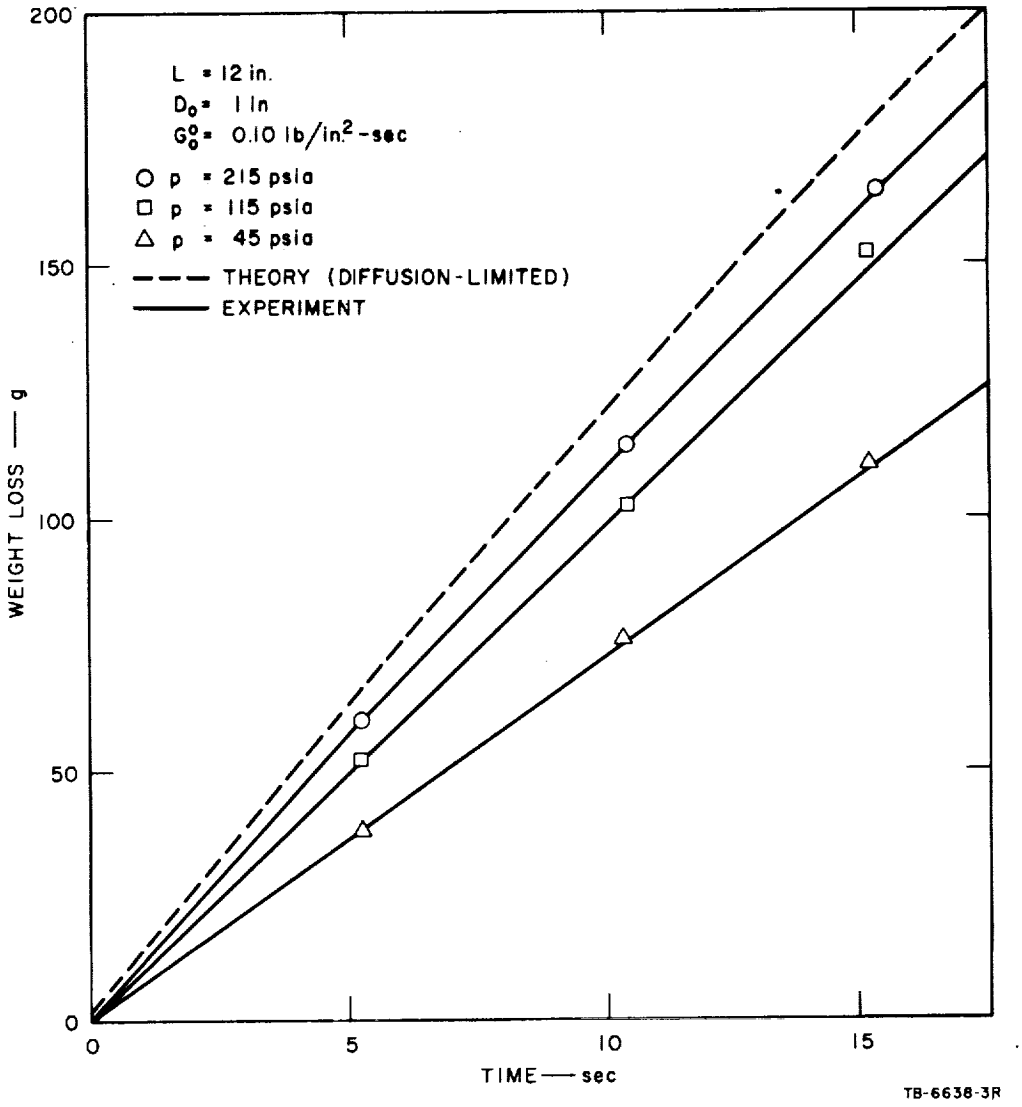

FIG. E-3 WEIGHT LOSS OF A PLEXIGLAS GRAIN AS A FUNCTION OF CHAMBER PRESSURE

Appendix F

CHAMBER PRESSURE RESPONSE TO VARIABLE OXIDIZER MASS FLOW

The equation expressing conservation of mass in the combustion chamber is

$$\frac{d(\rho V)}{dt} = \dot{m}_o + \dot{m}_f - \dot{m}_n \tag{F-1}$$

Using the perfect gas law, $p = \rho RT$, and the equation for the mass flow through the nozzle,

$$\dot{m}_n = \left[\frac{\gamma p^2}{RT} \left(\frac{2}{\gamma+1} \right)^{\frac{\gamma+1}{\gamma-1}} \right]^{\frac{1}{2}} A_t \tag{F-2}$$

Eq. F-1 becomes

$$\frac{V}{RT} \frac{dp}{dt} - \frac{pV}{RT^2} \frac{dT}{dt} = \dot{m}_t - \left[\frac{\gamma p^2}{RT} \left(\frac{2}{\gamma+1} \right)^{\frac{\gamma+1}{\gamma-1}} \right]^{\frac{1}{2}} A_t \tag{F-3}$$

where the oxidizer and fuel mass flows have been lumped together for convenience.

Two cases can be easily calculated--an isothermal process and an isentropic process. In the isothermal case $dT/dt = 0$ and Eq. F-3 may be written in the simple form

$$K_1 \frac{dP}{dt} = \dot{m}_t - K_2 P \tag{F-4}$$

where $P = p/p_i$, and

$$K_1 = \frac{p_i V}{RT_i} \tag{F-5a}$$

$$K_2 = \left[\frac{p_i^2}{RT_i} \left(\frac{2}{\gamma+1} \right)^{\frac{\gamma+1}{\gamma-1}} \right]^{\frac{1}{2}} A_{t_i} \tag{F-5b}$$

Since Eq. F-4 is linear, solutions can be superimposed. A typical forcing function of the form applied experimentally is

$$\dot{m}_t = \dot{m}_1 + (\dot{m}_2 - \dot{m}_1)(1 + \sin \omega t) \tag{F-6}$$

which denotes the superimposition of a step function and a sine wave. The solution for P is

$$P = \frac{(\dot{m}_2 - \dot{m}_1)}{K_2} \left[1 - e^{-t/\tau} + \frac{\sin(\omega t + \varphi)}{(1 + \tau^2 \omega^2)^{\frac{1}{2}}} \right] + 1 \tag{F-7}$$

where $\varphi = - \tan^{-1} \tau\omega$ is the phase angle, and $\tau = K_1/K_2$ is the characteristic time constant of the chamber. At large time, as $t \to \infty$, the magnitude of the pressure oscillation divided by the magnitude of the mass flow oscillation is

$$R = \left| \frac{K_2 P}{\dot{m}_2 - \dot{m}_1} \right| = \frac{1}{(1 + \tau^2 \omega^2)^{\frac{1}{2}}} \tag{F-8}$$

In the isentropic case, when $p = \rho^\gamma$, the counterpart of Eq. F-3 is

$$\frac{K_1}{\gamma} P^{-\frac{\gamma-1}{\gamma}} \frac{dP}{dt} = M - K_2 P^{\frac{\gamma+1}{2\gamma}} \tag{F-9}$$

This equation is nonlinear and must be solved numerically.

Appendix G

THERMOCHEMICAL CALCULATIONS FOR HYBRID PROPELLANTS

Thermochemical calculations were carried out for all of the PBAN-oxygen and PU-oxygen propellant systems studied experimentally at chamber pressures of 5 and 15 atm. Two O/F ratios were considered, stoichiometric and three-quarters of stoichiometric, the latter value most closely representing hybrid operation. The calculated flame temperatures are needed as inputs to the hybrid computer code. The results of the calculations are given on the following pages.

HYBRID SYSTEM NUMBER 1A PRESSURE = 5 ATMOSPHERES

ELEMENTS IN REACTANTS, ATOMS		FUEL	OXIDIZER	BINDERS
H	1.9756	10.34	0.	0.
C	1.3279	6.95	0.	0.
O	4.3061	0.13	2.00	0.
N	0.0401	0.21	0.	0.
AL	0.4670	0.	0.	1.00
ENTHALPY OF REACTANTS, KCAL	-16.3358			

	CHAMBER
PRESSURE, ATM	5.0000
TEMPERATURE, DEG K	3606.9656
HEAT CAPACITY, CAL /DEG K	233.5696
ENTHALPY, KCAL	-16.3358
ENTROPY, CAL / DEG K	240.5331
FROZEN GAMMA	1.1948
SHIFTING GAMMA	1.1187
MOLS OF GAS	3.3373
MOLECULAR WEIGHT	28.0280
DENSITY, GM / CC	0.000506155

HYBRID SYSTEM NUMBER 1A PRESSURE =15 ATMOSPHERES

ELEMENTS IN REACTANTS, ATOMS		FUEL	OXIDIZER	BINDERS
H	1.9756	10.34	0.	0.
C	1.3279	6.95	0.	0.
O	4.3061	0.13	2.00	0.
N	0.0401	0.21	0.	0.
AL	0.4670	0.	0.	1.00
ENTHALPY OF REACTANTS, KCAL	-16.3358			

	CHAMBER
PRESSURE, ATM	15.0000
TEMPERATURE, DEG K	3802.0615
HEAT CAPACITY, CAL /DEG K	201.1827
ENTHALPY, KCAL	-16.3358
ENTROPY, CAL / DEG K	233.3197
FROZEN GAMMA	1.1896
SHIFTING GAMMA	1.1232
MOLS OF GAS	3.2702
MOLECULAR WEIGHT	28.5647
DENSITY, GM / CC	0.001470614

60% PBAN/40% Al (O/F = 2.16)

HYBRID SYSTEM NUMBER 18 PRESSURE = 5 ATMOSPHERES

ELEMENTS IN REACTANTS, ATOMS		FUEL	OXIDIZER	BINDERS
H	2.3832	10.34	0.	0.
C	1.6019	6.95	0.	0.
O	3.9050	0.13	2.00	0.
N	0.0484	0.21	0.	0.
AL	0.5634	0.	0.	1.00
ENTHALPY OF REACTANTS, KCAL	-19.7067			

	CHAMBER
PRESSURE, ATM	5.0000
TEMPERATURE, DEG K	3667.0096
HEAT CAPACITY, CAL /DEG K	244.5151
ENTHALPY, KCAL	-19.7067
ENTROPY, CAL / DEG K	248.9951
FROZEN GAMMA	1.1965
SHIFTING GAMMA	1.1198
MOLS OF GAS	3.5238
MOLECULAR WEIGHT	26.3364
DENSITY, GM / CC	0.000471510

HYBRID SYSTEM NUMBER 18 PRESSURE =15 ATMOSPHERES

ELEMENTS IN REACTANTS, ATOMS		FUEL	OXIDIZER	BINDERS
H	2.3832	10.34	0.	0.
C	1.6019	6.95	0.	0.
O	3.9050	0.13	2.00	0.
N	0.0484	0.21	0.	0.
AL	0.5634	0.	0.	1.00
ENTHALPY OF REACTANTS, KCAL	-19.7067			

	CHAMBER
PRESSURE, ATM	15.0000
TEMPERATURE, DEG K	3867.8880
HEAT CAPACITY, CAL /DEG K	207.9801
ENTHALPY, KCAL	-19.7067
ENTROPY, CAL / DEG K	241.3212
FROZEN GAMMA	1.1912
SHIFTING GAMMA	1.1246
MOLS OF GAS	3.4505
MOLECULAR WEIGHT	26.8536
DENSITY, GM / CC	0.001369447

60% PBAN/40% Al (O/F = 1.62)

HYBRID SYSTEM NUMBER 1C PRESSURE = 5 ATMOSPHERES

ELEMENTS IN REACTANTS, ATOMS		FUEL	OXIDIZER	BINDERS
H	2.4041	10.34	0.	0.
C	1.6159	6.95	0.	0.
O	4.4802	0.13	2.00	0.
N	0.0488	0.21	0.	0.
AL	0.2150	0.	0.	1.00
ENTHALPY OF REACTANTS, KCAL	-19.8795			

	CHAMBER
PRESSURE, ATM	5.0000
TEMPERATURE, DEG K	3430.5849
HEAT CAPACITY, CAL /DEG K	230.4561
ENTHALPY, KCAL	-19.8795
ENTROPY, CAL / DEG K	255.0476
FROZEN GAMMA	1.2081
SHIFTING GAMMA	1.1183
MOLS OF GAS	3.6522
MOLECULAR WEIGHT	26.6035
DENSITY, GM / CC	0.000486299

HYBRID SYSTEM NUMBER 1C PRESSURE =15 ATMOSPHERES

ELEMENTS IN REACTANTS, ATOMS		FUEL	OXIDIZER	BINDERS
H	2.4041	10.34	0.	0.
C	1.6159	6.95	0.	0.
O	4.4802	0.13	2.00	0.
N	0.0488	0.21	0.	0.
AL	0.2150	0.	0.	1.00
ENTHALPY OF REACTANTS, KCAL	-19.8795			

	CHAMBER
PRESSURE, ATM	15.0000
TEMPERATURE, DEG K	3602.9991
HEAT CAPACITY, CAL /DEG K	199.7885
ENTHALPY, KCAL	-19.8795
ENTROPY, CAL / DEG K	247.1396
FROZEN GAMMA	1.2032
SHIFTING GAMMA	1.1232
MOLS OF GAS	3.5916
MOLECULAR WEIGHT	27.0389
DENSITY, GM / CC	0.001412466

80% PBAN/20% Al (O/F = 2.54)

HYBRID SYSTEM NUMBER 1D PRESSURE = 5 ATMOSPHERES

ELEMENTS IN REACTANTS, ATOMS		FUEL	OXIDIZER	BINDERS
H	2.9268	10.34	0.	0.
C	1.9672	6.95	0.	0.
O	4.0993	0.13	2.00	0.
N	0.0594	0.21	0.	0.
AL	0.2595	0.	0.	1.00
ENTHALPY OF REACTANTS, KCAL	-24.2012			

	CHAMBER
PRESSURE, ATM	5.0000
TEMPERATURE, DEG K	3430.6033
HEAT CAPACITY, CAL /DEG K	206.6365
ENTHALPY, KCAL	-24.2012
ENTROPY, CAL / DEG K	267.0809
FROZEN GAMMA	1.2131
SHIFTING GAMMA	1.1236
MOLS OF GAS	3.9283
MOLECULAR WEIGHT	24.6515
DENSITY, GM / CC	0.000452116

HYBRID SYSTEM NUMBER 1D PRESSURE =15 ATMOSPHERES

ELEMENTS IN REACTANTS, ATOMS		FUEL	OXIDIZER	BINDERS
H	2.9268	10.34	0.	0.
C	1.9672	6.95	0.	0.
O	4.0993	0.13	2.00	0.
N	0.0594	0.21	0.	0.
AL	0.2595	0.	0.	1.00
ENTHALPY OF REACTANTS, KCAL	-24.2012			

	CHAMBER
PRESSURE, ATM	15.0000
TEMPERATURE, DEG K	3596.2833
HEAT CAPACITY, CAL /DEG K	175.2233
ENTHALPY, KCAL	-24.2012
ENTROPY, CAL / DEG K	258.5418
FROZEN GAMMA	1.2085
SHIFTING GAMMA	1.1293
MOLS OF GAS	3.8664
MOLECULAR WEIGHT	25.0932
DENSITY, GM / CC	0.001314573

80% PBAN/20% Al (O/F = 1.91)

HYBRID SYSTEM NUMBER 1E PRESSURE = 5 ATMOSPHERES

ELEMENTS IN REACTANTS, ATOMS		FUEL	OXIDIZER
H	2.5923	10.34	0.
C	1.7424	6.95	0.
O	4.7326	0.13	2.00
N	0.0526	0.21	0.
ENTHALPY OF REACTANTS, KCAL	-21.4353		

	CHAMBER
PRESSURE, ATM	5.0000
TEMPERATURE, DEG K	3286.7481
HEAT CAPACITY, CAL /DEG K	224.4207
ENTHALPY, KCAL	-21.4353
ENTROPY, CAL / DEG K	262.3912
FROZEN GAMMA	1.2174
SHIFTING GAMMA	1.1172
MOLS OF GAS	3.8294
MOLECULAR WEIGHT	26.1136
DENSITY, GM / CC	0.000484101

HYBRID SYSTEM NUMBER 1E PRESSURE =15 ATMOSPHERES

ELEMENTS IN REACTANTS, ATOMS		FUEL	OXIDIZER
H	2.5923	10.34	0.
C	1.7424	6.95	0.
O	4.7326	0.13	2.00
N	0.0526	0.21	0.
ENTHALPY OF REACTANTS, KCAL	-21.4353		

	CHAMBER
PRESSURE, ATM	15.0000
TEMPERATURE, DEG K	3441.3549
HEAT CAPACITY, CAL /DEG K	195.8732
ENTHALPY, KCAL	-21.4353
ENTROPY, CAL / DEG K	254.0893
FROZEN GAMMA	1.2128
SHIFTING GAMMA	1.1222
MOLS OF GAS	3.7754
MOLECULAR WEIGHT	26.4874
DENSITY, GM / CC	0.001406923

100% PBAN (O/F = 3.11)

HYBRID SYSTEM NUMBER 1F PRESSURE = 5 ATMOSPHERES

ELEMENTS IN REACTANTS, ATOMS		FUEL	OXIDIZER
H	3.1986	10.34	0.
C	2.1499	6.95	0.
O	4.3777	0.13	2.00
N	0.0650	0.21	0.
ENTHALPY OF REACTANTS, KCAL	-26.4484		

	CHAMBER
PRESSURE, ATM	5.0000
TEMPERATURE, DEG K	3266.0898
HEAT CAPACITY, CAL /DEG K	196.0999
ENTHALPY, KCAL	-26.4484
ENTROPY, CAL / DEG K	277.4010
FROZEN GAMMA	1.2244
SHIFTING GAMMA	1.1297
MOLS OF GAS	4.1625
MOLECULAR WEIGHT	24.0238
DENSITY, GM / CC	0.000448182

HYBRID SYSTEM NUMBER 1F PRESSURE =15 ATMOSPHERES

ELEMENTS IN REACTANTS, ATOMS		FUEL	OXIDIZER
H	3.1986	10.34	0.
C	2.1499	6.95	0.
O	4.3777	0.13	2.00
N	0.0650	0.21	0.
ENTHALPY OF REACTANTS, KCAL	-26.4484		

	CHAMBER
PRESSURE, ATM	15.0000
TEMPERATURE, DEG K	3410.4882
HEAT CAPACITY, CAL /DEG K	166.9462
ENTHALPY, KCAL	-26.4484
ENTROPY, CAL / DEG K	268.3719
FROZEN GAMMA	1.2200
SHIFTING GAMMA	1.1299
MOLS OF GAS	4.1087
MOLECULAR WEIGHT	24.3386
DENSITY, GM / CC	0.001304485

100% PBAN (O/F = 2.34)

HYBRID SYSTEM NUMBER 2A PRESSURE = 5 ATMOSPHERES

ELEMENTS IN REACTANTS, ATOMS		FUEL	OXIDIZER	BINDERS
H	2.1811	9.87	0.	0.
C	1.1845	5.36	0.	0.
O	4.2815	1.50	2.00	0.
N	0.0265	0.12	0.	0.
AL	0.5448	0.	0.	1.00
ENTHALPY OF REACTANTS, KCAL	-19.2253			

	CHAMBER
PRESSURE, ATM	5.0000
TEMPERATURE, DEG K	3632.5293
HEAT CAPACITY, CAL /DEG K	241.7765
ENTHALPY, KCAL	-19.2253
ENTROPY, CAL / DEG K	241.1667
FROZEN GAMMA	1.1088
SHIFTING GAMMA	1.1177
MOLS OF GAS	3.3291
MOLECULAR WEIGHT	27.8401
DENSITY, GM / CC	C.000504732

HYBRID SYSTEM NUMBER 2A PRESSURE =15 ATMOSPHERES

ELEMENTS IN REACTANTS, ATOMS		FUEL	OXIDIZER	BINDERS
H	2.1811	9.87	0.	0.
C	1.1845	5.36	0.	0.
O	4.2815	1.50	2.00	0.
N	0.0265	0.12	0.	0.
AL	0.5448	0.	0.	1.00
ENTHALPY OF REACTANTS, KCAL	-19.2253			

	CHAMBER
PRESSURE, ATM	15.0000
TEMPERATURE, DEG K	3831.5544
HEAT CAPACITY, CAL /DEG K	207.4029
ENTHALPY, KCAL	-19.2253
ENTROPY, CAL / DEG K	233.9875
FROZEN GAMMA	1.1036
SHIFTING GAMMA	1.1221
MOLS OF GAS	3.2529
MOLECULAR WEIGHT	28.3947
DENSITY, GM / CC	C.001466416

60% PU/40% Al (O/F = 1.72)

HYBRID SYSTEM NUMBER 2B PRESSURE = 5 ATMOSPHERES

ELEMENTS IN REACTANTS, ATOMS		FUEL	OXIDIZER	BINDERS
H	2.5857	9.87	0.	0.
C	1.4042	5.36	0.	0.
O	3.9055	1.50	2.00	0.
N	0.0314	0.12	0.	0.
AL	0.6523	0.	0.	1.00
ENTHALPY OF REACTANTS, KCAL	-22.7920			

	CHAMBER
PRESSURE, ATM	5.0000
TEMPERATURE, DEG K	3694.7493
HEAT CAPACITY, CAL /DEG K	261.1249
ENTHALPY, KCAL	-22.7920
ENTROPY, CAL / DEG K	248.7088
FROZEN GAMMA	1.1891
SHIFTING GAMMA	1.1178
MOLS OF GAS	3.4864
MOLECULAR WEIGHT	26.2990
DENSITY, GM / CC	0.000472993

HYBRID SYSTEM NUMBER 2B PRESSURE =15 ATMOSPHERES

ELEMENTS IN REACTANTS, ATOMS		FUEL	OXIDIZER	BINDERS
H	2.5857	9.87	0.	0.
C	1.4042	5.36	0.	0.
O	3.9055	1.50	2.00	0.
N	0.0314	0.12	0.	0.
AL	0.6523	0.	0.	1.00
ENTHALPY OF REACTANTS, KCAL	-22.7920			

	CHAMBER
PRESSURE, ATM	15.0000
TEMPERATURE, DEG K	3900.9078
HEAT CAPACITY, CAL /DEG K	221.9965
ENTHALPY, KCAL	-22.7920
ENTROPY, CAL / DEG K	241.1806
FROZEN GAMMA	1.1838
SHIFTING GAMMA	1.1223
MOLS OF GAS	3.4093
MOLECULAR WEIGHT	26.8422
DENSITY, GM / CC	0.001374237

60% PU/40% Al (O/F = 1.28)

HYBRID SYSTEM NUMBER 2C PRESSURE = 5 ATMOSPHERES

ELEMENTS IN REACTANTS, ATOMS		FUEL	OXIDIZER	BINDERS
H	2.6351	9.87	0.	0.
C	1.4310	5.36	0.	0.
O	4.5630	1.50	2.00	0.
N	0.0320	0.12	0.	0.
AL	0.2483	0.	0.	1.00
ENTHALPY OF REACTANTS, KCAL	-23.2269			

	CHAMBER
PRESSURE, ATM	5.0000
TEMPERATURE, DEG K	3417.7966
HEAT CAPACITY, CAL /DEG K	232.9202
ENTHALPY, KCAL	-23.2269
ENTROPY, CAL / DEG K	256.2981
FROZEN GAMMA	1.2028
SHIFTING GAMMA	1.1171
MOLS OF GAS	3.6483
MOLECULAR WEIGHT	26.5124
DENSITY, GM / CC	0.000488639

HYBRID SYSTEM NUMBER 2C PRESSURE =15 ATMOSPHERES

ELEMENTS IN REACTANTS, ATOMS		FUEL	OXIDIZER	BINDERS
H	2.6351	9.87	0.	0.
C	1.4310	5.36	0.	0.
O	4.5630	1.50	2.00	0.
N	0.0320	0.12	0.	0.
AL	0.2483	0.	0.	1.00
ENTHALPY OF REACTANTS, KCAL	-23.2269			

	CHAMBER
PRESSURE, ATM	15.0000
TEMPERATURE, DEG K	3588.4941
HEAT CAPACITY, CAL /DEG K	201.6443
ENTHALPY, KCAL	-23.2270
ENTROPY, CAL / DEG K	248.3392
FROZEN GAMMA	1.1980
SHIFTING GAMMA	1.1218
MOLS OF GAS	3.5872
MOLECULAR WEIGHT	26.9490
DENSITY, GM / CC	0.001419932

80% PU/20% Al (O/F = 2.00)

HYBRID SYSTEM NUMBER 2D PRESSURE = 5 ATMOSPHERES

ELEMENTS IN REACTANTS, ATOMS		FUEL	OXIDIZER	BINDERS
H	3.2779	9.87	0.	0.
C	1.7258	5.36	0.	0.
O	4.2205	1.50	2.00	0.
N	0.0386	0.12	0.	0.
AL	0.2965	0.	0.	1.00
ENTHALPY OF REACTANTS, KCAL	-28.0115			

	CHAMBER
PRESSURE, ATM	5.0000
TEMPERATURE, DEG K	3438.2041
HEAT CAPACITY, CAL /DEG K	227.3620
ENTHALPY, KCAL	-28.0115
ENTROPY, CAL / DEG K	268.2076
FROZEN GAMMA	1.2057
SHIFTING GAMMA	1.1204
MOLS OF GAS	3.9007
MOLECULAR WEIGHT	24.7054
DENSITY, GM / CC	0.000454307

HYBRID SYSTEM NUMBER 2D PRESSURE =15 ATMOSPHERES

ELEMENTS IN REACTANTS, ATOMS		FUEL	OXIDIZER	BINDERS
H	3.1779	9.87	0.	0.
C	1.7258	5.36	0.	0.
O	4.2205	1.50	2.00	0.
N	0.0386	0.12	0.	0.
AL	0.2965	0.	0.	1.00
ENTHALPY OF REACTANTS, KCAL	-28.0115			

	CHAMBER
PRESSURE, ATM	15.0000
TEMPERATURE, DEG K	3608.5302
HEAT CAPACITY, CAL /DEG K	193.9320
ENTHALPY, KCAL	-28.0115
ENTROPY, CAL / DEG K	259.7620
FROZEN GAMMA	1.2010
SHIFTING GAMMA	1.1255
MOLS OF GAS	3.8357
MOLECULAR WEIGHT	25.1087
DENSITY, GM / CC	0.001320556

80% PU/20% Al (O/F = 1.50)

HYBRID SYSTEM NUMBER 2E PRESSURE = 5 ATMOSPHERES

ELEMENTS IN REACTANTS, ATOMS		FUEL	OXIDIZER
H	3.0101	9.87	0.
C	1.6347	5.36	0.
O	4.8012	1.50	2.00
N	0.0366	0.12	0.
ENTHALPY OF REACTANTS, KCAL	-26.5326		

	CHAMBER
PRESSURE, ATM	5.0000
TEMPERATURE, DEG K	3256.5509
HEAT CAPACITY, CAL /DEG K	226.1879
ENTHALPY, KCAL	-26.5326
ENTROPY, CAL / DEG K	268.1019
FROZEN GAMMA	1.2140
SHIFTING GAMMA	1.1164
MOLS OF GAS	3.9190
MOLECULAR WEIGHT	25.5169
DENSITY, GM / CC	0.000477426

HYBRID SYSTEM NUMBER 2E PRESSURE =15 ATMOSPHERES

ELEMENTS IN REACTANTS, ATOMS		FUEL	OXIDIZER
H	3.0101	9.87	0.
C	1.6347	5.36	0.
O	4.8012	1.50	2.00
N	0.0366	0.12	0.
ENTHALPY OF REACTANTS, KCAL	-26.5326		

	CHAMBER
PRESSURE, ATM	15.0000
TEMPERATURE, DEG K	3406.9760
HEAT CAPACITY, CAL /DEG K	197.2991
ENTHALPY, KCAL	-26.5327
ENTROPY, CAL / DEG K	259.6049
FROZEN GAMMA	1.2094
SHIFTING GAMMA	1.1213
MOLS OF GAS	3.8645
MOLECULAR WEIGHT	25.8763
DENSITY, GM / CC	0.001388326

100% PU (O/F = 2.27)

HYBRID SYSTEM NUMBER 2F PRESSURE = 5 ATMOSPHERES

ELEMENTS IN REACTANTS, ATOMS		FUEL	OXIDIZER
H	3.6220	9.87	0.
C	1.9669	5.36	0.
O	4.5067	1.50	2.00
N	0.0440	0.12	0.
ENTHALPY OF REACTANTS, KCAL	-31.9262		

	CHAMBER
PRESSURE, ATM	5.0000
TEMPERATURE, DEG K	3245.2159
HEAT CAPACITY, CAL /DEG K	209.7912
ENTHALPY, KCAL	-31.9262
ENTROPY, CAL / DEG K	282.4401
FROZEN GAMMA	1.2188
SHIFTING GAMMA	1.1209
MOLS OF GAS	4.2231
MOLECULAR WEIGHT	23.6792
DENSITY, GM / CC	0.000444591

HYBRID SYSTEM NUMBER 2F PRESSURE =15 ATMOSPHERES

ELEMENTS IN REACTANTS, ATOMS		FUEL	OXIDIZER
H	3.6220	9.87	0.
C	1.9669	5.36	0.
O	4.5067	1.50	2.00
N	0.0440	0.12	0.
ENTHALPY OF REACTANTS, KCAL	-31.9262		

	CHAMBER
PRESSURE, ATM	15.0000
TEMPERATURE, DEG K	3389.2556
HEAT CAPACITY, CAL /DEG K	179.2704
ENTHALPY, KCAL	-31.9262
ENTROPY, CAL / DEG K	273.2804
FROZEN GAMMA	1.2145
SHIFTING GAMMA	1.1266
MOLS OF GAS	4.1677
MOLECULAR WEIGHT	23.9942
DENSITY, GM / CC	0.001294076

100% PU (O/F = 1.73)

REFERENCES

1. Marxman, G. A., Wooldridge, C. E., and Muzzy, R. J., "Fundamentals of Hybrid Boundary Layer Combustion," Heterogeneous Combustion, Progress in Astronautics and Aeronautics, Vol. 15, Academic Press, New York, 1964, p. 485.

2. Marxman, G. A., and Gilbert, M., "Turbulent Boundary Layer Combustion in the Hybrid Rocket," Ninth Symposium (International) on Combustion, Academic Press, New York, 1963, p. 371.

3. Barrere, M., and Moutet, A., "La Propulsion par Fusees Hybrides," presented at the International Astronautical Congress, Paris, September 1963.

4. Green, L., Jr., "Introductory Considerations of Hybrid Rocket Combustion," Heterogeneous Combustion, Progress in Astronautics and Aeronautics, Vol. 15, Academic Press, New York, 1964, p. 451.

5. Marxman, G. A., and Wooldridge, C. E., "Research on the Combustion Mechanism of Hybrid Rockets," presented at the Combustion and Propulsion Panel, AGARD, NATO, San Diego, California, April 22-24, 1965.

6. Marxman, G. A., "Combustion in the Turbulent Boundary Layer on a Vaporizing Surface," Tenth Symposium (International) on Combustion, The Combustion Institute, Pittsburgh, 1965, p. 1337.

7. Muzzy, R. J., and Feemster, J. R., "The Design of a Hybrid Rocket Propulsion System," Proceedings of the Ninth Liquid Propulsion Symposium, Vol. I, CPIA, St. Louis, October 1967.

8. Marxman, G. A., "Boundary Layer Combustion in Propulsion," Eleventh Symposium (International) on Combustion, The Combustion Institute, Pittsburgh, 1967, p. 269.

9. Smoot, L. D., and Price, C. F., "Regression Rate Mechanism of Nonmetalized Hybrid Fuel Systems," AIAA J. 3, 1408-1413 (1965).

10. _____, "Regression Rates of Metalized Hybrid Fuel Systems," AIAA J. 4, 910-915 (1966).

11. Smoot, L. D., and Price, C. F., "Pressure Dependence of Hybrid Fuel Regression Rates," AIAA J. 5, 102-106 (1967).

12. Miller, E., "Hybrid Rocket Combustion Regression Rate Mode," AIAA J. 4, 752-753 (1966).

13. Kosdon, F. J., and Williams, F. A., "Pressure Dependence of Nonmetalized Hybrid Fuel Regression Rates,"AIAA J. 5, 774-778 (1967).

14. Lees, L., "Convective Heat Transfer with Mass Addition and Chemical Reactions," Combustion and Propulsion, Third AGARD Colloquium, Pergamon Press, New York, 1958.

15. Spalding, D. B., "A Standard Formulation of the Steady Convective Mass Transfer Problem," Int. J. Heat Mass Transfer 1, 192(1960).

16. Wooldridge, C. E., Marxman, G. A., and Capener, E. L., "Propellant Combustion Phenomena During Rapid Depressurization," Final Report, Stanford Research Institute, Contract No. NAS 7-389, October 1967.

17. Marxman, G. A., Wooldridge, C. E., and Capener, E. L., "Response of a Burning Propellant Surface to Erosive Transients," Final Report, Stanford Research Institute, Contract No. AF 49(638)-1665, April 1968.

18. Marxman, G. A., and Wooldridge, C. E., "The Effect of Surface Reactions on the Solid Propellant Response Function," AIAA J. 6, 471-478 (1968).

19. _____, "Finite-Amplitude Axial Instability in Solid Rocket Combustion," presented at the 12th Symposium (International) on Combustion, Poitiers, France, August 1968.

20. Wooldridge, C. E., and Muzzy, R. J., "Boundary Layer Turbulence Measurements with Mass Addition and Combustion," AIAA J. 4, 2009-2016 (1966).

21. Schlichting, H., Boundary Layer Theory, Chap. XXI, McGraw-Hill Book Co., New York, 1955.

22. Marxman, G. A., and Wooldridge, C. E., "The Incompressible Turbulent Boundary Layer on a Flat Plate with Homogeneous Injection," Technical Memorandum TM-33-64-U1, United Technology Center, Sunnyvale, 1964.

23. Mager, A., "Transformation of the Compressible Turbulent Boundary Layer," J. Aero. Sci. 25, 305(1958).

24. Burggraf, O. R., "The Compressibility Transformation and the Turbulent-Boundary-Layer Equations," J. Aero. Sci. 29, 434 (1962).

25. Crocco, L., "Transformations of the Compressible Turbulent Boundary Layer with Heat Exchange," AIAA J. 1, 2723 (1963).

26. Marxman, G. A., et al., "Investigation of Fundamental Phenomena in Hybrid Propulsion," Vol. I, Final Tech. Report, Stanford Research Institute, Contract No. NOw 64-0659-c, 1967, pp. 255-262.

27. Wooldridge, C. E., and Muzzy, R. J., "Internal Ballistic Considerations in Hybrid Rocket Design," J. Spacecraft and Rockets 4(2), 255-262 (1967).

28. Karlovitz, B., "Combustion Waves in Turbulent Gases," Section 4, Combustion Processes, Vol. II, High Speed Aerodynamics and Jet Propulsion Series, Princeton University Press, Princeton, 1956.

29. Denison, M. R., and Baum, E., "A Simplified Model of Unstable Burning in Solid Propellants," ARS J. 31, 1112-1122 (1961).